

1-1-2011

Modelling high frequency ultrasound scattering from cells and ultrasound contrast agents

Omar Falou
Ryerson University

Follow this and additional works at: <http://digitalcommons.ryerson.ca/dissertations>

 Part of the [Electrical and Computer Engineering Commons](#)

Recommended Citation

Falou, Omar, "Modelling high frequency ultrasound scattering from cells and ultrasound contrast agents" (2011). *Theses and dissertations*. Paper 562.

This Dissertation is brought to you for free and open access by Digital Commons @ Ryerson. It has been accepted for inclusion in Theses and dissertations by an authorized administrator of Digital Commons @ Ryerson. For more information, please contact bcameron@ryerson.ca.

MODELLING HIGH FREQUENCY
ULTRASOUND SCATTERING FROM
CELLS AND ULTRASOUND CONTRAST
AGENTS

By

OMAR FALOU

M.A.Sc., Ryerson University, Toronto, Ontario, Canada, 2006

B.A.Sc., Ryerson University, Toronto, Ontario, Canada, 2003

A dissertation
presented to Ryerson University
in partial fulfillment of the
requirements for the degree of
Doctor of Philosophy
in the Program of
Electrical and Computer Engineering

Toronto, Ontario, Canada, 2011

© Omar Falou, 2011

Author's Declaration

I hereby declare that I am the sole author of this dissertation.

I authorize Ryerson University to lend this dissertation to other institutions or individuals for the purpose of scholarly research.

Omar Falou

I further authorize Ryerson University to reproduce this dissertation by photocopying or by other means, in total or in part, at the request of other institutions or individuals for the purpose of scholarly research.

Omar Falou

MODELLING HIGH FREQUENCY ULTRASOUND SCATTERING FROM CELLS AND ULTRASOUND CONTRAST AGENTS

Doctor of Philosophy, 2011

Omar Falou

Electrical and Computer Engineering, Ryerson University

Abstract

High frequency ultrasound has been shown to detect structural and physical changes in cell ensembles during apoptosis and hence has the potential of monitoring cancer treatment. Ultrasound contrast agents have also been shown to enhance contrast between blood and the surrounding tissue and hence may be used to distinguish between treated and untreated tumours. Theoretical models of high frequency ultrasound scattering from individual cells and ultrasound contrast agents (UCAs) are needed in order to develop methods for using high frequency ultrasound to classify tumours, quantify their responses to treatment, and eventually provide a better cancer detection and treatment monitoring techniques. This work introduces a new technique for measuring the ultrasound backscatter from individual micron-sized objects by combining a microinjection system with a co-registered optical microscope and an ultrasound imaging device. The system was calibrated by measuring the backscatter response from polystyrene microspheres and comparing it to theoretical predictions of an elastic sphere. The backscatter responses from single sea urchin oocytes and acute myloid leukemia cells were also investigated. It was found that such responses are best modelled using the fluid sphere model. A finite element model was also introduced to study scattering from microspheres and UCAs. The Helmholtz equation was used to describe the propagation of sound waves in the fluid domains

whereas the constitutive equation was used to describe the stress-strain relationship in the solid domains. Studies on polystyrene microspheres and UCAs revealed the existence of a systematic relationship between the resonance frequencies and the microsphere surface modes. No such a relationship was found for the UCAs of interest. Instead, these agents exhibited a collection of complex oscillations which appear to be a combination of various surface modes. Increasing the UCA's shell thickness and its shear modulus produced a shift in the resonance frequencies to higher values. A decrease in UCA diameter produced similar effects. The importance of these findings towards the understanding of the UCA behaviour at high frequencies and the generation of harmonics are discussed. Future work includes the measurement of the backscatter response from individual UCAs and cells at various apoptotic stages.

Acknowledgements

First and foremost, I wish to express my gratitude to my dissertation supervisors Dr. Michael C. Kolios and Dr. J. Carl Kumaradas for guiding me on this most exciting venture and for training me to become an independent scientist.

I would like to acknowledge my supervisory committee members, Dr. Sridhar Krishnan, Dr. Marcello Papini, and Dr. Alireza Sadeghian. I am also grateful to Dr. Min Rui, Candice Schreiber, and Arthur Worthington for helping me with the design and execution of the experiments, to Dr. Gregory J. Czarnota for his constructive feedback, and to Amin Jafari Sojahrood for his fruitful discussions. I also wish to thank all my colleagues who contributed to the work of this dissertation: Ralph E. Baddour, Hamed Basseri, Michael Dobson, Ahmed El-Kaffas, George Nathanael, and Avery Raess. Many thanks to my fellow students/staff at the Medical Physics and Electrical and Computer Engineering labs at Ryerson University for making the environment comfortable and friendly.

Last but not least, I wish to thank my wife Sana for her unceasing support and my bundle of joy Yara for always putting a smile on my face especially during difficult times. I would also like to thank my mother, my sister, and my brothers for their continuous encouragement.

This dissertation is dedicated to my father Ahmad, a cancer victim, who taught me courage, patience, and dedication. He was the main force behind my academic success. I truly miss him!

To my dear father Ahmad

إلى والدي العزيز أحمد

Table of Contents

Author’s Declaration	ii
Abstract.....	iii
Acknowledgements	v
Table of Contents	vii
List of Tables	x
List of Figures.....	xi
Nomenclature	xiv
Chapter 1 Introduction.....	1
1.1 Measurement of Apoptosis.....	2
1.2 Motivation	3
1.3 A Historical Perspective of Ultrasound.....	6
1.4 Fundamentals of Sound.....	7
1.4.1 Types of Sound Waves	7
1.4.2 Interaction of Sound Waves with Matter.....	9
1.4.3 Surface Modes	11
1.5 Dynamics of Ultrasound Contrast Agents.....	12
1.6 Fundamentals of Finite Element Analysis	15
1.7 Objectives and Hypothesis	16
1.8 Dissertation Organization and Contributions	17
Chapter 2 A study of high frequency ultrasound scattering from non-nucleated biological specimens.....	19
2.1 Introduction	19
2.2 Methods.....	20
2.2.1 Calculation of Backscatter Transfer Function:.....	20

2.2.2 Time domain Signal Reconstruction:	24
2.3 Results	25
2.4 Discussion and Conclusions.....	30
Chapter 3 The measurement of ultrasound scattering from individual micron- sized objects and its application in single cell scattering	33
3.1 Introduction	33
3.2 Technique description and validation	36
3.2.1 Methods	36
3.2.2 Results	42
3.2.3 Discussion.....	44
3.3 Scattering from cells.....	46
3.4 Concluding remarks	54
Chapter 4 Finite element modelling of high frequency ultrasound scattering from microspheres and ultrasound contrast agents.....	55
4.1 Introduction	55
4.2 Methods.....	58
4.2.1 Polystyrene Microsphere	58
4.2.2 Ultrasound Contrast Agent.....	62
4.3 Results	67
4.3.1 Polystyrene microsphere	67
4.3.2 BR14 Ultrasound Contrast Agent.....	67
4.4 Discussion and Conclusions.....	76
4.4.1 Polystyrene Microspheres.....	76
4.4.2 BR14 Ultrasound Contrast Agent.....	77
Chapter 5 Concluding remarks and future work	82
5.1 Summary and Concluding Remarks.....	82
5.2 Future work	84
Appendix A	88
Analytical Solution of Sound Scattering from a Sphere Immersed in a Fluid.....	88
Anderson’s Solution for Fluid Sphere Immersed in a Fluid.....	88

Faran's Solution for an Elastic Sphere Immersed in a Fluid.....	90
Church's solution of Sound Scattering from a Sphere Immersed in a Fluid.....	92
Appendix B	94
List of Publications.....	94
Papers in Refereed Journals.....	94
Papers in Refereed Conference Proceedings	94
Abstracts and/or other Conference Proceedings.....	95
Bibliography	96

List of Tables

Table 1.1: Properties of selected ultrasound contrast agents	6
Table 2.1: Properties of the transducers used in the experiments.....	24
Table 3.1: Properties of the transducers used in the experiments.....	37
Table 3.2: Polystyrene physical properties	42
Table 4.1: Physical properties of the BR14 ultrasound contrast agent.....	66

List of Figures

Figure 1.1: Trophoblast cell undergoing apoptosis.....	2
Figure 1.2: Ultrasonic backscatter of acute myeloid leukemia cells exposed to the chemotherapeutic cisplatin after 0, 6, 12, 24 and 48 hrs.	4
Figure 1.3: Optical image of lipid-coated ultrasound contrast agents	5
Figure 1.4: Types of sound waves	8
Figure 1.5: Rayleigh Surface Wave	8
Figure 1.6: Illustration of reflection and refraction of an acoustic wave.....	10
Figure 1.7: Surface modes	12
Figure 1.8: Ultrasound contrast agent behaviour as a function of the Mechanical Index	13
Figure 1.9: UCA non-linear scattering.....	14
Figure 2.1: Ultrasonic B-scan of a sparse suspension of sea urchin oocytes in seawater at 40 MHz. Inset is an optical microscopy of sea urchin oocytes	22
Figure 2.2: Average backscatter echoes from individual sea urchin oocytes and their corresponding incident pulses from three transducers: 20 MHz, 40 MHz, and 80 MHz excited at 19 MHz, 40 MHz, and 55 MHz, respectively.	25
Figure 2.3: Echoes from individual sea urchin oocytes at 40 MHz.....	26
Figure 2.4: Theoretical and measured backscatter frequency responses of single sea urchin oocytes in seawater subject to three incident pulses from three transducers: 20 MHz, 40 MHz, and 80 MHz excited at 19 MHz, 40 MHz, and 55 MHz, respectively.....	27
Figure 2.5: Contour plot of the least square fit coefficient of the experimental and theoretical backscatter transfer functions as a function of the sphere density and speed of sound...	27
Figure 2.6: Average experimental and reconstructed echoes from individual sea urchin oocytes at 19 MHz, 40 MHz, and 55 MHz.....	28

Figure 2.7: Comparison of the difference in averaging RF lines in time and in power spectral domains for the 20 MHz transducer.	29
Figure 3.1: Experimental setup composed of a XenoWorks microinjection system consisting of a digital microinjector, a micromanipulator, and a micropipette puller.....	37
Figure 3.2: Schematic diagram of the scatterer suspension setup	38
Figure 3.3: Representative optical images, B-scans, and ultrasonic echoes at 55 MHz of a micropipette before and after the release of a scatterer	41
Figure 3.4: Representative backscatter echoes from a 20 μm polystyrene microsphere and their corresponding incident pulses at 25 MHz and 55 MHz.....	43
Figure 3.5: Theoretical and experimental backscatter frequency responses of a single 20 μm polystyrene microsphere in degassed and distilled water subject to incident pulses from two transducers: 25 MHz and 55 MHz.....	44
Figure 3.6: Representative backscatter echoes from an OCI-AML-5 cell imaged at 25 MHz and 55 MHz	47
Figure 3.7: Theoretical and experimental backscatter frequency responses of a single OCI-AML-5 cell in PBS subject to incident pulses from a 25 MHz transducer.	48
Figure 3.8: Theoretical and experimental backscatter frequency responses of a single OCI-AML-5 cell in PBS subject to incident pulses from a 55 MHz transducer	49
Figure 3.9: Theoretical and average experimental backscatter frequency responses from individual OCI-AML-5 cells in PBS subject to incident pulses from two transducers: 25 and 55 MHz	50
Figure 4.1: Setup of the finite-element model for UCA immersed in a fluid.....	63
Figure 4.2: Backscatter pressure amplitude vs. number of mesh elements.	64
Figure 4.3: Meshed model: 14,736 triangular elements.	65
Figure 4.4: Analytical (Faran) and finite-element solutions for scattering from a 30 μm polystyrene microsphere immersed in water at high frequencies.....	68
Figure 4.5: Finite-element solutions for deformations of a 30 μm polystyrene microsphere at 23.1, 33.7, 43.8, 53.5, and 63.2 MHz	68
Figure 4.6: Analytical solutions for angular scattering from a 30 μm polystyrene microsphere at 23.1, 33.7, 43.8, 53.5, and 63.2 MHz.....	69

Figure 4.7: Resonance frequency vs. contrast agent diameter: comparison between the Church and finite element solutions.	70
Figure 4.8: Effects of varying the shell thickness on the backscatter response for 4 μm diameter BR14.	70
Figure 4.9: Backscatter vs. frequency for a 100 nm shelled, 4 μm diameter UCA immersed in water.	71
Figure 4.10: Finite-element solutions for deformations of a 100 nm shelled, 4 μm diameter UCA at 15.1, 37.7, 49.6, 51.6, and 64.8 MHz.	71
Figure 4.11: Finite element solutions for angular scattering from a 100 nm shelled, 4 μm diameter UCA at 15.1, 37.7, 49.6, 51.6, and 64.8 MHz.	72
Figure 4.12: Effects of varying the shell shear modulus on the backscatter response for a 100 nm shelled, 4 μm diameter UCA.	73
Figure 4.13: Effects of varying the contrast agent's diameter on the backscatter response for a 100 nm shelled UCA.	74
Figure 4.14: Relationship between shell thickness and monopole resonance frequency for a 4 μm UCA.	74
Figure 4.15: Relationship between shell shear modulus and the resonance frequencies for a 100 nm , 4 μm UCA.	75
Figure 4.16: Relationship between diameter and resonance frequencies for a 100 nm shelled UCA.	75
Figure 5.1: Fluorescence microscopy images of AML cells undergoing apoptosis.	85
Figure A.1: Illustration of scattering by a sphere.	89
Figure A.2: Depiction of an ultrasound contrast agent.	92

Nomenclature

a	radius of scatterer
c	speed of sound
c_1	longitudinal speed of sound in object
c_2	shear speed of sound in object
c_3	longitudinal speed of sound in medium
c_g	speed of sound in gas
d	diameter of scatterer
E	Young's modulus
E_s	shell's Young's modulus
f	frequency
F	face load
I	intensity of scattered wave
I_0	intensity of incident wave
I_z	attenuated intensity of wave
k	wavenumber of incident wave
k_1	longitudinal wavenumber in object
k_2	shear wavenumber in object
k_3	wavenumber in medium
m	order of the scattered wave
n	surface mode number
\mathbf{n}	outward pointing normal vector to a surface
p	acoustic pressure

p_s	scattered acoustic pressure
P_0	incident plane wave pressure
P_h	hydrostatic pressure
r, θ, ϕ	spherical coordinates
T_z	ratio of transmitted to incident pressure
\mathbf{u}	time-harmonic displacement vector in the scatterer
V_s	Volume of the shell
z	distance travelled by a wave
Z	acoustic impedance
Z_1	acoustic impedance of medium
Z_2	acoustic impedance of object
α	attenuation coefficient
σ	stress
$\sigma_x, \sigma_y, \sigma_z$	normal stresses
$\tau_{xy}, \tau_{xz}, \tau_{yx}, \tau_{yz}, \tau_{zx}, \tau_{zy}$	shear stresses
ϵ	strain
$\epsilon_x, \epsilon_y, \epsilon_z$	normal strains
$\gamma_{xy}, \gamma_{yx}, \gamma_{zx}$	shear strains
λ	wavelength
μ_a	absorption coefficient
μ_s	scattering coefficient
ν	Poisson's ratio
ν_s	shell's Poisson's ratio
ω	angular frequency
ω_0	angular linear resonance frequency
θ_i	angle of incidence

θ_r	angle of reflection
θ_t	angle of refraction
ρ	mass density
ρ_1	mass density of the object
ρ_3	mass density of the surrounding medium
ρ_g	mass density of gas
ρ_L	mass density of surrounding liquid
$[D]$	constitutive matrix
η_m	phase shift of mode m
n_m	spherical Neumann function
j_m	spherical Bessel function
P_m	Legendre polynomial of order m
S	term accounting for strain
s_1	surface tension of inner boundary
s_2	surface tension of outer boundary
ρ_s	shell mass density
G_s	shell shear modulus
κ	polytropic exponent
β	difference in mass densities between shell and surrounding fluid
γ	sum of the squares of the difference between theoretical and experimental values
$\mathcal{H}\{ \}$	Hilbert transform
$H_{\text{expr}_f}(t)$	matrix containing B-scans data after Hilbert transform
$\mathcal{F}^{-1}\{ \}$	Fourier transform

$\text{BSTF}_{\text{theor}}(\omega)$	theoretical backscatter transfer function
$\text{BSTF}_{\text{expr}}(\omega)$	experimental backscatter transfer function
$r_{\text{theor}}(t)$	constructed time domain echo
$r_{\text{ref}}(t)$	average incident pulse
$r_{\text{expr}}(t)$	average backscatter echoes from individual objects
$r_{\text{expr}_f}(t)$	matrix containing measured RF lines
δR_s	shell thickness of the ultrasound contrast agent
R_z	ratio of reflected to incident pressure
R_{01}	inner radius
R_{02}	outer radius
$R_{\text{expr}}(\omega)$	Fourier transform of the average backscatter signal
$R_{\text{ref}}(\omega)$	Fourier transform of the average reference signal
R_{coef}	reflection coefficient of a given material

Chapter 1

Introduction

Cancer is a malignant tumour of potentially unlimited growth and is the leading cause of early death in Canada, being responsible for almost 29.5% of all deaths according to a report published by StatsCan in 2004 (StatsCan, 2004). The same report suggests that cancer may soon surpass cardiovascular diseases, and become *Canada's main cause of death*. It's estimated that 38% of women in Canada will develop cancer during their lifetimes. Among Canadian men, 41% will develop cancer during their lifetimes, with half of them occurring in the lung, prostate, colon, and rectum (Canadian Cancer Society, 2002). Currently, there are four major types of cancer treatment: surgery, radiation therapy, chemotherapy, and immunotherapy. Surgery, radiation therapy, and chemotherapy are the most commonly practiced therapies. Ultrasound has been proposed as a tool for monitoring cancer treatment. Understanding the interaction between sound waves and scattering objects is a prerequisite for the development of monitoring techniques. Various sound scattering models have been developed for this purpose. These include: Rayleigh model for scattering from tiny particles, Anderson model for scattering from fluid spheres, Farn model for scattering from elastic spheres, and Church model for scattering from ultrasound contrast agents (details are given in section 1.4.2 and in Appendix A).

1.1 Measurement of Apoptosis

Cancer cells may respond to chemotherapy or radiation therapy by undergoing apoptosis. Apoptosis, or programmed cell death, was originally defined by Kerr *et al.* in 1972 (Kerr *et al.*, 1972). Apoptosis is characterized by the following histological features: nuclear condensation and DNA degradation, cytoplasm shrinkage, and fragmentation of the cell into membrane-bound bodies by a budding process (Hacker, 2000; Saraste *et al.*, 2000) as shown in Figure 1.1.

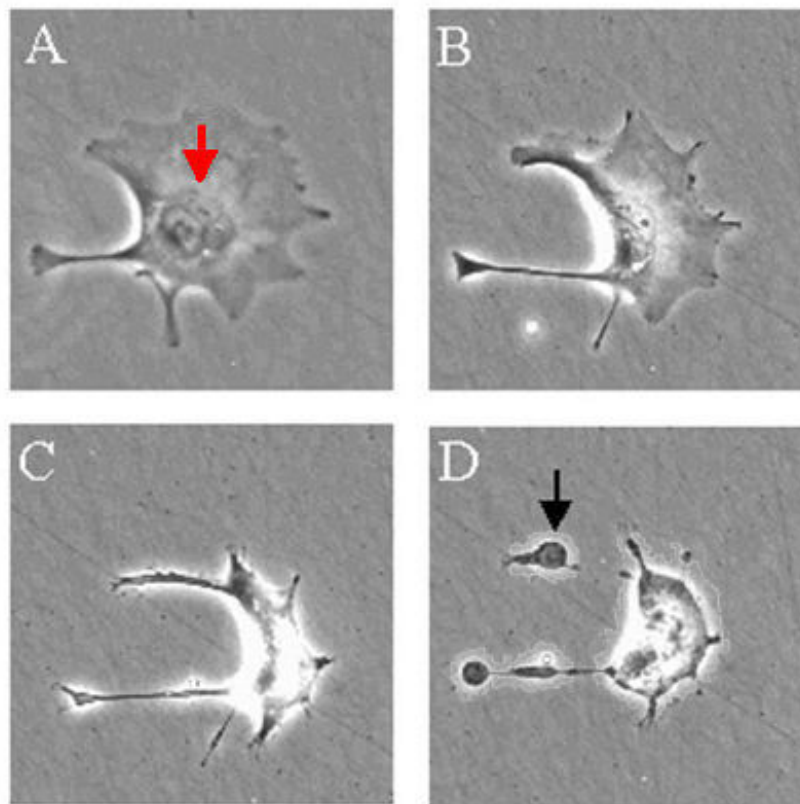


Figure 1.1: Trophoblast cell undergoing apoptosis: (A) Nuclear condensation (red arrow); (B) and (C) Nuclear condensation and cytoplasm shrinkage; (D) Fragmentation of cell and formation of small vesicles (black arrow). Adapted from Reproductive & Cardiovascular Disease Research Group (2007).

It usually takes weeks or even months of repeated dosing with drugs or radiation fractions until the efficiency of the treatment is assessed. This long evaluation time period can be troublesome since drugs have severe side effects and are expensive. A number of techniques have been developed for the detection of cell death and apoptosis by measuring the apoptotic index, the percentage of cells in a volume undergoing apoptosis. Both light and electron microscopy can be used to detect the morphological changes that occur during apoptosis shown in Figure 1.1. Dyes which stain DNA may be used to enhance the contrast of the nuclear material. A common and highly efficient technique for the detection of apoptosis is the measurement of the characteristic, non-random DNA fragmentation. The fragmented DNA can be detected using a variety of techniques such as: enzyme-linked immunosorbent assay or ELISA (Salgame *et al.*, 1997).

1.2 Motivation

A major disadvantage of the current apoptosis measurement techniques is that they are invasive. A sample from a culture or a biopsy from a patient must be obtained. Such a sample can only provide a measurement at only one spatial location and time-point. Hence, providing a rapid non-invasive way to measure the apoptotic index, and cell death, in general, would be very beneficial since it may help in quantifying patient response to cancer treatment. Ultrasound has been proposed as one such method.

It has been shown that high frequency ultrasound (20–60 MHz) can be used to detect structural and physical changes in cell ensembles during cell death (Sherar *et al.*, 1987), including apoptosis (Czarnota *et al.*, 1997; Czarnota *et al.*, 1999; Kolios *et al.*, 2004).

Ultrasonic backscatter from cell ensembles treated with the chemotherapeutic cisplatin, which induces apoptosis, increased the ultrasound backscatter by 9–13dB resulting in much brighter images as illustrated in Figure 1.2. Hence, high frequency ultrasound has the potential of monitoring cancer treatment.

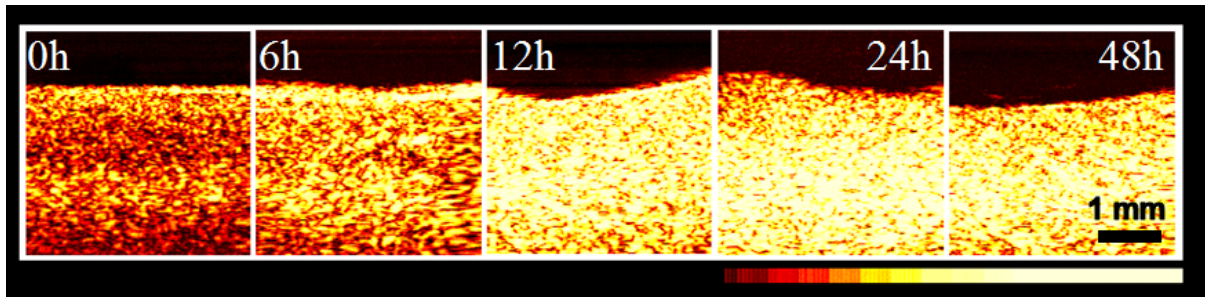


Figure 1.2: Ultrasonic backscatter of acute myeloid leukemia (AML) cells exposed to the chemotherapeutic cisplatin after 0, 6, 12, 24 and 48 hrs. The speckle pattern is characteristic of ultrasound images. Adapted from Czarnota *et al.* (1999).

When compared to other diagnostic imaging modalities such as MRI, ultrasound represents the safest, fastest, and the least expensive method (Stride *et al.*, 2003). High frequency ultrasound (HFUS) imaging has less penetration depth (< 25 mm) than clinical ultrasound but greater image resolution which makes it more sensitive to cell structure and spatial distribution, and therefore to the changes that occur during cell death (Hunt *et al.*, 2002; Tunis *et al.*, 2005). This makes HFUS ideal for imaging small animals, such as mice, which have much smaller organs than humans. Using mice in laboratory research has many benefits. Mice are small, inexpensive, and easy to maintain. They can reproduce quickly so research can be conducted on many mouse generations. Experimental drugs are currently being tested on mice and their efficacy in treating the tumour is determined before using them on patients. Mouse models were developed for this purpose and have been used in preclinical cancer research for almost a century (Naf *et al.*, 2002). These include human tumour xenografts and genetically engineered models (GEMs).

Human tumour xenografts are human cells lines grown in an immunodeficient mouse whereas in GEMs, tumours are expressed as a result of the alteration of the genetic material. Xenografts are easy to use, relatively inexpensive but lack the cellular and architectural complexity of GEM tumours. On the other hand, GEMs are genetically and histologically accurate models of human tumour and were developed to overcome the limitations of xenografts (Becher *et al.*, 2006).

Another potential way to monitor tumour treatment in small animals is by the use of ultrasound contrast agents or UCAs (Pollard *et al.*, 2007; Bagi *et al.*, 2009; O'Connor *et al.*, 2009; Guibal *et al.*, 2010). UCAs are gas-filled, encapsulated bubbles that are administered intravenously to the venous system. They are very small (< 8 microns) which enables them to pass through capillaries but big enough so that they remain in the vasculature as shown in Figure 1.3. UCAs have a high degree of echogenicity compared to tissues, and therefore they

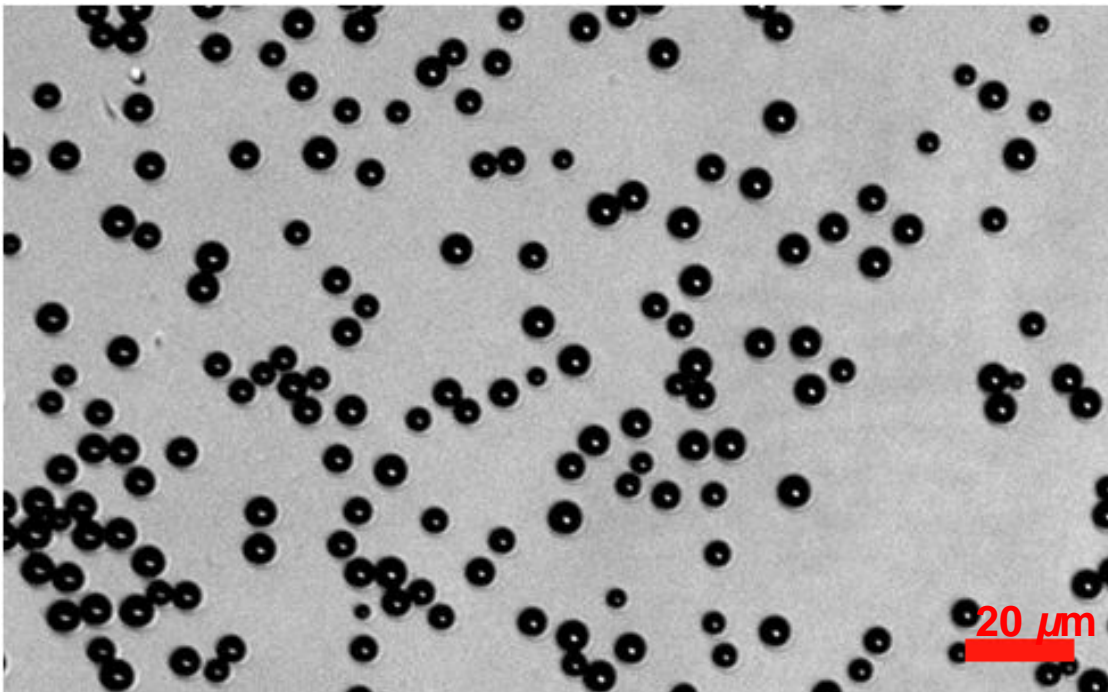


Figure 1.3: Optical image of lipid-coated ultrasound contrast agents (produced in-house by Tyrone M. Porter's Lab, Boston University, MA).

enable contrast between blood and the surrounding tissue and hence may be used to distinguish between treated (no or little blood circulation) and untreated tissues (normal blood circulation). A summary of the various applications of UCAs is given in Klibanov *et al.* (2006). Table 1.1 gives the properties of selected UCAs.

Table 1.1: Properties of selected ultrasound contrast agents (Adapted from Szabo, 2004)

Manufacturer	Name	Gas	Shell
Acusphere	AI-700	Decafluorobutane	Polymer
Bracco	Sonovue	Sufurhexafluoride	Surfactant
Bracco	BR14	Perfluorocarbon	Phospholipid
BMS	Definity	Octafluoropropane	Liposome
Mallinckrodt	Albunex	Air	Albumin
Amersham	Optison	Octafluoropropane	Albumin
Amersham	Sonazoid	Perfluorocarbon	Lipid
Point Biomedical	CardioSphere	Air	Polymer bilayer
Schering	Levovist	Air	Fatty acid

1.3 A Historical Perspective of Ultrasound

Sound waves can be divided into three categories based on their frequencies:

- Infrasound: frequencies below the audible sound (< 20 Hz)
- Audible sound: frequencies detectable by the human ear (20 Hz – 20 KHz)
- Ultrasound: frequencies above 20 KHz. Medical imaging applications of ultrasound typically use frequencies that are higher than 1 MHz.

Ultrasound was first applied in warfare through the technique of SOund NAvigation and Ranging (SONAR) where a “pulse-echo” technique is used to locate submerged objects. Another application of ultrasound emerged in the 1940’s when “pulse-echo” ultrasound technique was used in non-destructive testing of metals (Firestone, 1945). Medical

ultrasound application emerged in the late 1940's and early 1950's through the use of ultrasound for non-invasive imaging (Reid *et al.*, 1952; National Council on Radiation Protection and Measurements, 1983; Szabo, 2004) and for the treatment of polyarthritis, by driving hydrocortisone ointment molecules across the skin to treat the inflamed tissue (Fellinger *et al.*, 1954). This led to the development of phonophoresis, a powerful technique which uses ultrasound to enhance transdermal drug delivery (Tyle *et al.*, 1989). Heating tissue using ultrasound has been shown to enhance radiotherapy (Overgaard *et al.*, 1995; Vernon *et al.*, 1996), chemotherapy (Saad *et al.*, 1989; Harrison *et al.*, 1991; Saad *et al.*, 1992), and gene therapy (Azuma *et al.*, 2003). The development of medical ultrasound techniques continue to evolve and expand.

1.4 Fundamentals of Sound

1.4.1 Types of Sound Waves

Sound waves are produced when mechanical energy propagates through the medium by the compression and rarefaction of the medium. In fluids, the sound wave travels parallel to the direction of particle motion and is called longitudinal or compressional wave as shown in Figure 1.4(a). In solids, particles can also vibrate perpendicular to the direction of particle motion; hence additional types of waves may exist. These include transverse or shear waves, where the particles oscillate perpendicular to the direction of the wave propagation as illustrated in Figure 1.4(b). Longitudinal waves are also called P waves (primary) since they travel faster than shear waves, also known as S or secondary waves (Serway *et al.*, 2000).

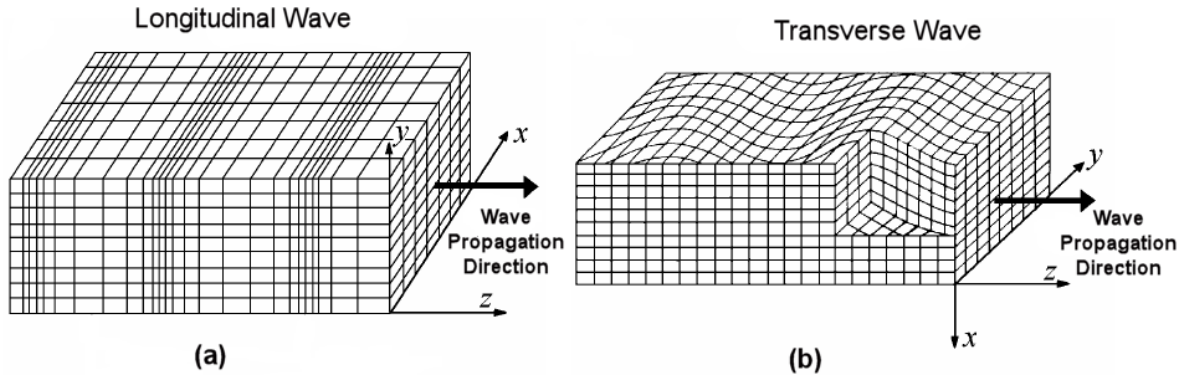


Figure 1.4: Types of sound waves: (a) Longitudinal wave, (b) Transverse wave (Adapted from Cobbold, 2007)

A third type of waves which propagate across the surface of solids known as Rayleigh Surface Waves may also exist. These are a combination of longitudinal and transverse displacements of particles. Rayleigh waves have horizontal displacement where each particle of the medium moves in an elliptical orbit parallel to the direction of wave propagation as shown in Figure 1.5. Many other types of waves also exist but they are beyond the scope of this work.

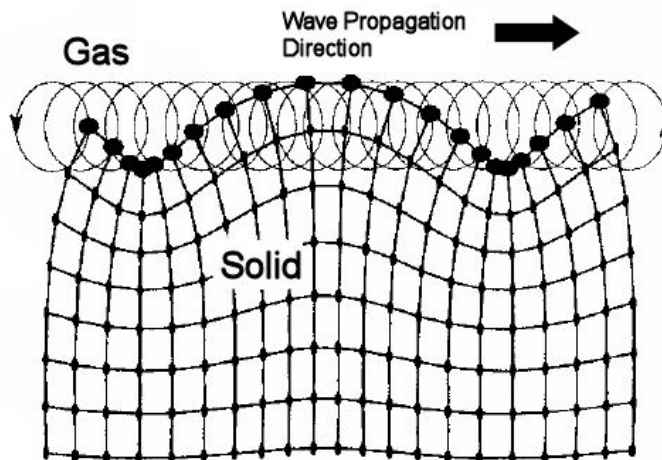


Figure 1.5: Rayleigh Surface Wave (Adapted from Cobbold, 2007)

1.4.2 Interaction of Sound Waves with Matter

When a sound wave travelling in a medium of acoustic impedance Z_1 (the acoustic impedance of a medium is the product of its mass density by its speed of sound) encounters an object of different acoustic impedance Z_2 , reflection, refraction, attenuation, or scattering can occur.

Reflection and Refraction

When the object is much larger than the wavelength, part of the incident wave is reflected and the rest of the energy is transmitted (refracted) through the object as illustrated in Figure 1.6. The fraction of the incident wave pressure that is reflected, R_z , depends on the acoustic impedances of the medium (Z_1) and the object (Z_2), the incident angle θ_i , and the angle of refraction θ_t :

$$R_z = \frac{Z_2 \cos \theta_i - Z_1 \cos \theta_t}{Z_2 \cos \theta_i + Z_1 \cos \theta_t}. \quad (1.1)$$

The fraction of the incident wave pressure that is transmitted, T_z , is given by:

$$T_z = 1 - R_z. \quad (1.2)$$

The angle of reflection θ_r is always equal to the angle of incidence θ_i . The angle of refraction can be calculated using Snell's Law:

$$\frac{\sin \theta_i}{c_1} = \frac{\sin \theta_t}{c_2}, \quad (1.3)$$

where c_1 and c_2 are the sound velocities in the medium and the object respectively (Szabo, 2004; Cobbold, 2007).

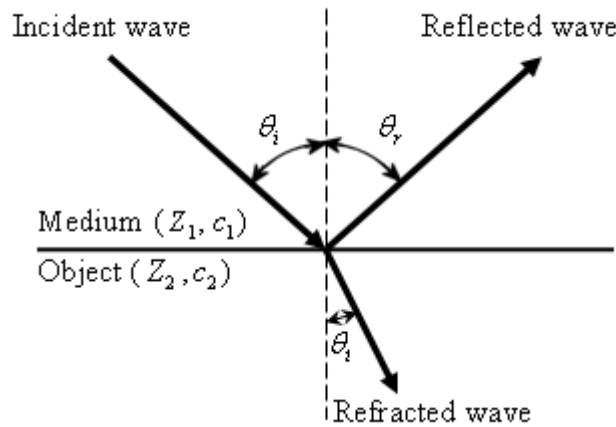


Figure 1.6: Illustration of reflection and refraction of an acoustic wave

Scattering

Scattering is a physical process where waves are forced to deviate from their trajectory by non-uniformities (objects) in the medium. Lord Rayleigh (Strutt, 1872) was first to study acoustic wave scattering by spherical objects where the size (radius, a) of the object is much smaller than the wavelength ($a \ll \lambda$). If the density of the object is the same but its compressibility is different than that of the surrounding medium, the object will radially expand and contract which gives rise to a scattered pressure known as monopole radiation. On the contrary, if the compressibility of the object is the same but its density is different than that of the surrounding medium, the object will oscillate back and forth and the scattered pressure is known as dipole radiation. It is thought that the monopole radiation dominates the dipole radiation for most soft biological tissues (Nassiri *et al.*, 1986).

Scattering from objects of a size comparable to the wavelength is more complex and is referred to as Mie Scattering. Mie Scattering was first introduced by Gustav Mie who studied scattering of electromagnetic waves by spherical objects (Mie, 1908). Morse (1936)

formulated the scattering solution for pressure waves for a fixed rigid sphere with no sound wave penetration. The solution of scattering by a fluid sphere immersed in a fluid, in which no shear waves exist, was derived by Anderson (1950). Shortly after, Faran (1951) derived a mathematical formulation for scattering by an elastic sphere immersed in a fluid. Experimental studies of Faran's elastic scattering theory were undertaken by many investigators few years later (Hampton *et al.*, 1961; Hickling, 1962). Subsequent studies of elastic scattering from objects suspended in fluids has led to the formulation of the Resonance Scattering Theory (Flax *et al.*, 1978).

Attenuation

Sound attenuation is the loss of energy with distance travelled caused by scattering and absorption. For plane waves travelling through a homogenous medium, sound attenuation is given by:

$$I_z = I_0 e^{-2\alpha z}, \quad (1.4)$$

where I_0 is the initial intensity of a signal at some location, I_z is the reduced intensity after the wave has travelled a distance z from that initial location, and α is the attenuation coefficient. The attenuation coefficient α is the sum of the scattering and absorption coefficients, $\alpha = \mu_s + \mu_a$, where μ_s and μ_a are the scattering and absorption coefficients, respectively (Cobbold, 2007).

1.4.3 Surface Modes

The interaction between sound waves and a given object (such as a sphere) can lead to the deformation of the shape of the latter. These shape deformations, or surface modes, are

thought to occur as a result of the existence of surface waves which travel along the free surface of the scatter. These modes are denoted by n , which is the number of wavelengths of the surface distortion that span the sphere's circumference. Some of the basic surface modes are shown in Figure 1.7. In the breathing mode ($n = 0$), the sphere contracts and expands periodically (also known as radial or monopole oscillation). In the dipole mode ($n = 1$), the sphere oscillates rigidly back and forth, whereas in the quadrupole mode ($n = 2$), the shape alternates between a prolate and an oblate spheroid, etc. (Uberall *et al.*, 1996). The study of surface modes is of great importance for the understanding of the behaviour of spherical objects such as ultrasound contrast agents as will be shown later in this dissertation.

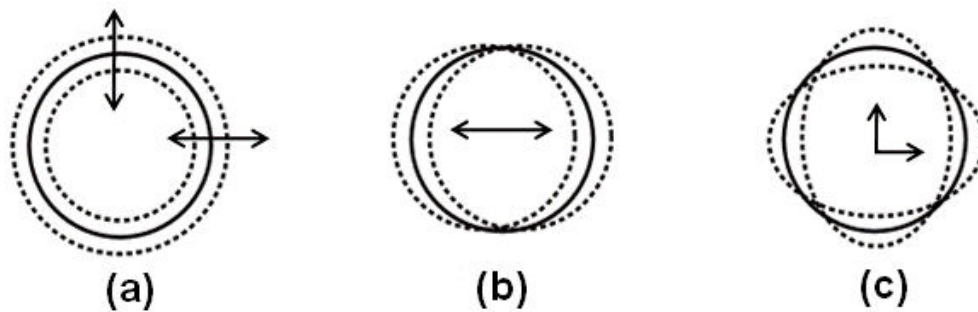


Figure 1.7: Surface modes: (a) Breathing mode; (b) Dipole mode; (c) Quadruple mode (Adapted from Uberall *et al.*, 1996)

1.5 Dynamics of Ultrasound Contrast Agents

The first mathematical formulation which predicts the dynamic response (linear and non-linear) of an air bubble (no shell) subject to a time-varying input pressure field has been derived by Lord Rayleigh in 1917 and is known as the Rayleigh-Plesset (RP) equation. The RP equation has several limitations. It is only applicable to a gas bubble oscillating in an incompressible fluid and can only predict the radial oscillations of the bubble; hence it cannot

be used to model that behaviour of UCAs that have an encapsulating shell (Leighton, 2004). The RP equation has been modified by many authors to take into account the presence of shell which increases both the overall mechanical stiffness of the bubble and its acoustic damping. De Jong *et al.* (1993) modelled the behaviour of UCAs by incorporating experimentally measured mechanical properties of the shell into the RP equation. C. Church (1995) derived a RP-like equation describing the dynamics of ultrasound contrast agents in which the shell is assumed to be a continuous layer of solid viscoelastic material. Despite these theoretical and experimental efforts, *the behaviour of UCAs is not fully understood* (Stride *et al.*, 2003). For instance, current analytical models do not incorporate non-radial oscillations which can be generated through instabilities at the boundary of the gas inside the UCA and the surrounding liquid medium (Versluis *et al.*, 2004). These modes alter the backscatter characteristics of these UCAs.

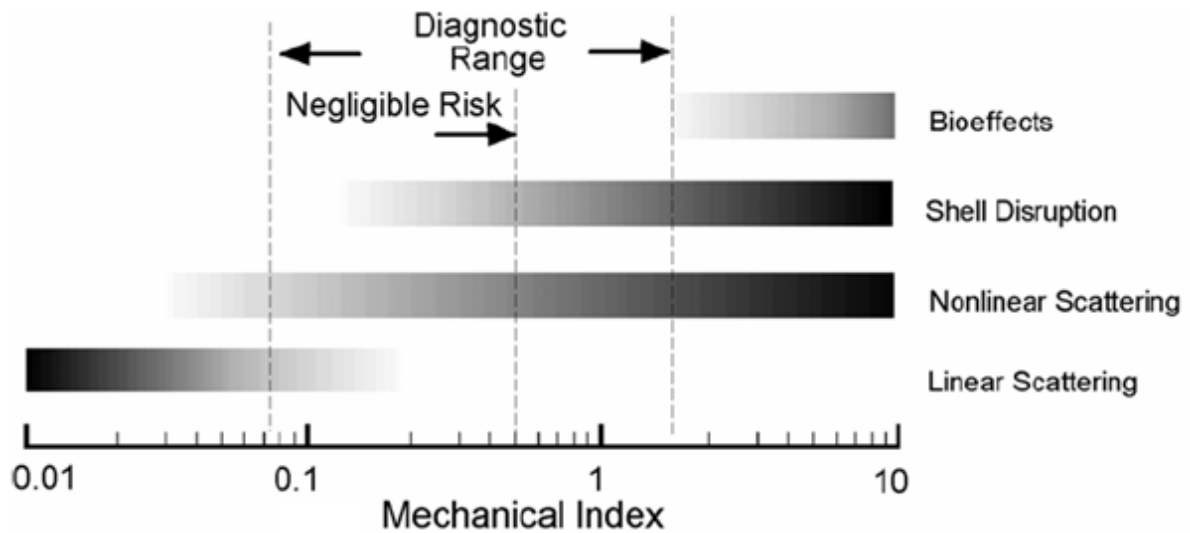


Figure 1.8: Ultrasound contrast agent behaviour as a function of the Mechanical Index (Adapted from Cobbold, 2007).

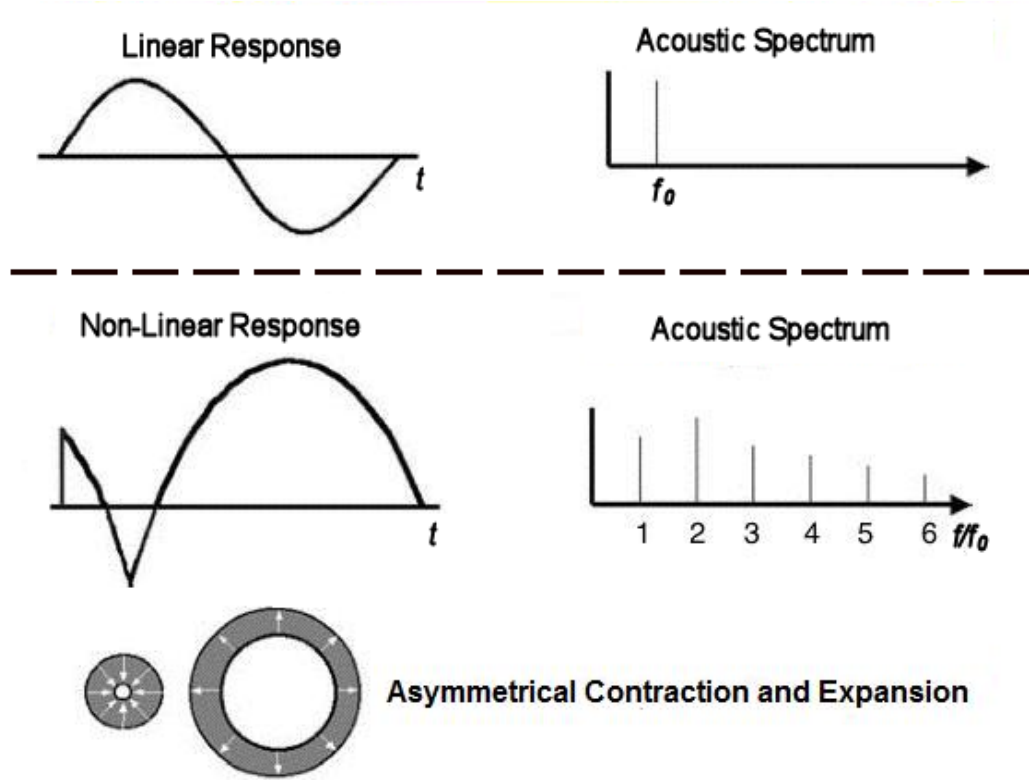


Figure 1.9: UCA non-linear scattering (Adapted from Szabo, 2004).

The behaviour of ultrasound contrast agents depends on the Mechanical Index (MI), a measure of the acoustic output of an ultrasound system defined as the peak negative pressure of the system divided by the square root of the centre frequency of the incident ultrasound pulse. Figure 1.8 illustrates the ultrasound contrast agent behaviour as a function the Mechanical Index. Linear scattering occurs at low pressures when the UCA oscillation amplitude is small relative to the equilibrium radius (Hoff, 2001). In this case, the UCA can be modelled as a linear-mass spring system, in which the mass of the surrounding medium corresponds to mass of the system, the gas pressure inside the UCA corresponds to the spring, and the damping sources (such as the viscosity of the shell) corresponds to the dash-pot of the system. Non-linear scattering occurs at large-amplitude pressure fields when the

UCA expands with the pressure field, but cannot contract by the same amount because the gas inside the bubble cannot be compressed indefinitely. When the oscillations are non-linear, the scattered signal may contain frequencies other than the driving frequency, known as harmonics (Figure 1.9). Subharmonics, scattered energies with frequencies that are a fraction of the fundamental (driving) frequency, may also be generated. Subharmonic imaging was shown to improve the contrast between blood and the surrounding tissue in compared to harmonic imaging (Goertz *et al.*, 2005).

1.6 Fundamentals of Finite Element Analysis

Analytical solutions to the problem of wave scattering from simple, homogeneous, and three dimensional structures such as fluid and elastic spheres have been extensively studied in the past (some solutions are given in Appendix A). However, these formulations are not flexible enough to be extended to wave scattering from complex scatterers such as ultrasound contrast agents, UCAs interactions with blood vessels and cells. Finite-element analysis (FEA), a numerical technique that involves dividing a domain into a large number of small elements called “finite elements”, is flexible and can be applied to irregular-shaped objects composed of several materials with complex boundary conditions (Logan, 2002). The system of interest can be linear or non-linear, static or dynamic. FEA is capable of solving a wide variety of problems in, for example, structural mechanics, acoustics, and heat transfer. It is also capable of accurately predicting the values of several physical variables, such as pressure, stresses, strains, etc.

Solving a problem using FEA involves four general steps:

- Discretization of the computational domain into finite-elements. Domain discretization involves the creation of a system of points called nodes which makes a grid called a mesh.
- Specification of the element type. This is done by selecting linear, quadratic, or cubic elements with higher order basis functions.
- Assembly of the elements together while satisfying the requirements of equilibrium and continuity between the elements. The result of the assembly process is a set of algebraic equations represented in matrix form.
- Solving the resulting algebraic equations using numerical methods such as the Gauss-Seidel method (Gerald *et al.*, 1999).

1.7 Objectives and Hypothesis

The objectives of my dissertation are to model high frequency ultrasound scattering from biological specimens, cells, and ultrasound contrast agents. Such models are prerequisites for predicting the ultrasound backscatter from tissues with and without the presence of ultrasound contrast agents which will help in measuring cell death and hence assessing the efficacy of tumour treatment. The long term goal of this research is to use high frequency ultrasound imaging to monitor cancer treatment.

I hypothesize that numerical methods, particularly the finite-element analysis, may be used to predict high frequency ultrasound scattering from biological specimens, cells, and contrast agents for the purpose of monitoring cancer treatment.

1.8 Dissertation Organization and Contributions

Chapter 2 presents the investigation of high frequency ultrasound scattering from non-nucleated biological specimen such as sea urchin oocytes. Results from this investigation show that sea urchin oocytes are best modeled as fluid spheres. This chapter also establishes an objective methodology to determine the appropriate theoretical model of the properties of individual cells as ultrasound scatterers. Chapter 3 presents a novel technique for measuring the high frequency ultrasound backscatter from individual micron-sized objects and its application to deduce scattering from nucleated biological cells such as Acute Myloid Leukemia (AML) cells. The developed technique can also be used to measure the backscatter from ultrasound contrast agents when they are in suspension or when they are attached to cells. Chapter 4 introduces a finite-element model to study the dynamic behaviour of microspheres and ultrasound contrast agents. This model, which accounts for the non-radial oscillations of scatterer, has the advantage of being able to predict high resonance modes. Using this model, I was able to show the existence of a relationship between the resonance frequencies and the surface modes of polystyrene microspheres. The model also has the potential of being used to optimize the parameters of the ultrasound contrast agents for high frequency ultrasound. Finally, a summary of what has been accomplished along with

suggestions for future work are presented in Chapter 5. A list of publications related to this dissertation is given in Appendix B.

Chapter 2

A study of high frequency ultrasound scattering from non-nucleated biological specimens¹

2.1 Introduction

When compared to clinical ultrasound imaging (1–10 MHz), high frequency ultrasound imaging is more sensitive to cell structure and cell spatial distribution changes (Hunt *et al.*, 2002; Tunis *et al.*, 2005). Recent publications have demonstrated that high frequency ultrasound has the potential of being used for tumour classification (Oelze *et al.*, 2004). Others have shown that high frequency ultrasound can be used to detect structural and physical changes in cell ensembles during apoptosis (Czarnota *et al.*, 1997). Ultrasonic backscatter from cell ensembles treated with the chemotherapeutic drug cisplatin, which induces apoptosis increased the ultrasound backscatter signal amplitude by 9 – 13 dB and induced changes in the frequency dependence of backscatter (Czarnota *et al.*, 1997; Kolios *et*

¹ The work presented in this chapter has been published as: Falou, O., Baddour, R. E., Nathanael, G., Czarnota, G. J., Kumaradas, J. C., and Kolios, M. C. (2008), “A Study of High Frequency Ultrasound Scattering from Non-nucleated Biological Specimens,” *Journal of the Acoustical Society of America* 124(5), EL278-283. It was also selected for publication in the 2008 *Virtual Journal of Biological Physics Research*, 16(8).

al., 2002). Theoretical models of ultrasound scattering at the cellular level are needed in order to develop methods for using ultrasound backscatter measurements to classify tumours or determine their response to treatment. The development of these models requires an understanding of the mechanical properties of components of a cell such as the nucleus and the cytoplasm.

Baddour *et al.*(2005) have performed successful measurements of high frequency (10–65 MHz) backscatter from single cells. A recent study by the same group showed that for prostate carcinoma (PC-3) cells whose nucleus to cell volume ratio is 0.33, the backscatter response could be modeled as a fluid sphere (Baddour *et al.*, 2007). However, the same study found that for human acute myeloid leukemia (OCI-AML-5) cells whose nucleus to cell volume ratio equals to 0.50, the backscatter response was not modeled as well by a fluid sphere. Baddour *et al.* hypothesized that the cytoplasm is of fluid nature whereas the nucleus possesses elastic properties, giving rise to this discrepancy (Baddour *et al.*, 2007). This work attempts to model the ultrasound backscatter (10–62 MHz) from some non-nucleated biological specimens through the measurement and comparison of the backscatter response from sea urchin oocytes to theoretical predictions from a fluid sphere.

2.2 Methods

2.2.1 Calculation of Backscatter Transfer Function:

A sparse suspension of oocytes from *Strongylocentrotus purpuratus* (purple sea urchin) were prepared in artificial seawater: $\rho = 1025 \text{ Kg/m}^3$, $c = 1527 \text{ m/s}$ (MacKenzie, 1981). This was necessary in order to eliminate the detection of two scattering events per radiofrequency (RF)

line (that would complicate the analysis) and potential multiple scattering. The oocytes were obtained by shedding live female urchins into artificial seawater with 0.5 M KCL. They are mainly composed of chromatin and yolk proteins. These oocytes were selected because their spherical shape and narrow size distribution as shown in Figure 2.1 inset (mean oocyte diameter of approximately $75 \mu\text{m}$, standard deviation = $2.2 \mu\text{m}$). The size distribution of the oocytes was determined experimentally as follows: an Olympus IX71 inverted microscope (Olympus America, Inc., Center Valley, PA) with a Retiga EXi CCD camera (QImaging, Inc., Surrey, BC) connected to a PC loaded with a digital video recording software, StreamPix 3 (NorPix, Inc., Montreal, QC), was used to capture images of a micrometer ruler and 20 oocytes placed on a slide. The image analysis tool, ImageJ (<http://rsbweb.nih.gov/ij/>), was used to find the pixel-to-micron conversion factor based on the image of the ruler. The diameters of the oocytes were estimated by measuring their diameters in pixels, which were then converted to microns based on the pixel-to-micron conversion factor found earlier.

Data acquisition was performed using a VisualSonics VS40B ultrasound imaging device (VisualSonics, Inc., Toronto, ON). Three transducers, with different resonant frequencies, f-numbers, and focal lengths, were employed. Table 2.1 summarizes the properties of the three transducers. Data from the -6 dB bandwidth of each spectrum of the incident pulse (as measured by the reflection off a quartz plate) were used in the analysis, giving an overall analysis range of 10 – 62 MHz. The performance of the 80 MHz transducer pulsed at 55 MHz was satisfactory but this was not a transducer designed to operate with the commercial device. The reason for using this transducer was to expand the frequency band in this study from 51 to 62 MHz. It was the only transducer available to achieve such an expansion of the bandwidth at the time. Ten independent acquisitions of 75, 100, and 125 linearly separated ($150 \mu\text{m}$ spacing) raw RF echo signals were

performed using the 20, 40, 80 MHz transducers, respectively. Since oocytes centered in the focal region of a given transducer lead to a higher amplitude echo opposed to oocytes that are located off the transducer axis, any RF scan-lines whose maximum was less than 90% of the overall maximum value from all RF lines were discarded, assuming they did not contain an oocyte completely in the focal region of that scan. This was done to obtain “pure” RF lines in order to perform time domain averaging of the backscattered echoes.

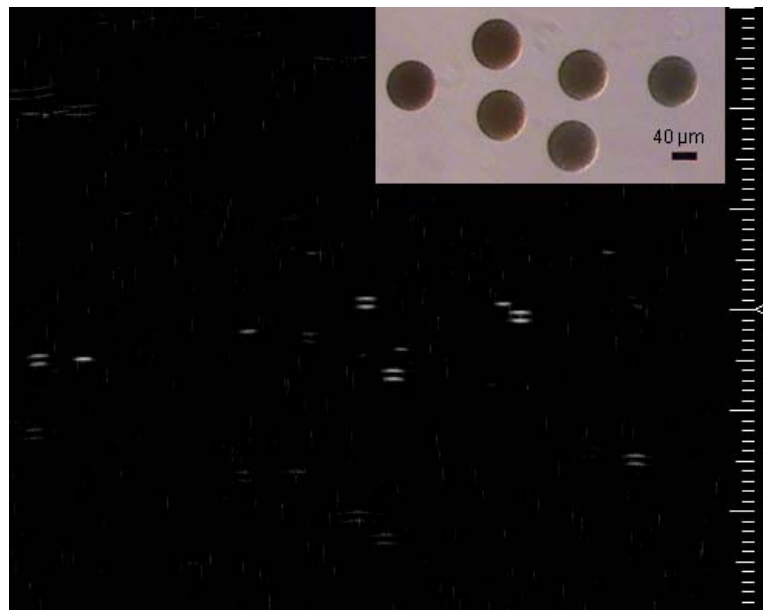


Figure 2.1: Ultrasonic B-scan of a sparse suspension of sea urchin oocytes in seawater at 40 MHz (smallest scale = $100 \mu\text{m}$). The triangle on the right hand side of the image indicates the location of the transducer focus. Inset is an optical microscopy of sea urchin oocytes.

A Hamming window of $2 \mu\text{s}$ width, centered at the maximum value of each RF line, was applied to all remaining lines in order to partially remove abnormal scattering patterns in some lines due to the presence of more than one oocyte in the focal region (resolution volume) of the scan. Furthermore, visual inspection was performed to eliminate any lines which exhibited these patterns and were not removed by the previous step. For each transducer, the remaining RF lines

(of which there were between 5 and 23) were translated to align the midpoint of the two largest positive peaks and then averaged to obtain a single RF line corresponding to the backscatter from an individual “average” oocyte. From this a backscatter transfer function, $\text{BSTF}_{\text{expr}}(\omega)$, was calculated:

$$\text{BSTF}_{\text{expr}}(\omega) = \frac{R_{\text{expr}}(\omega)}{R_{\text{coef}} R_{\text{ref}}(\omega)}, \quad (2.1)$$

where $R_{\text{expr}}(\omega)$ is the Fourier transform of the average backscatter signal (within the transducer’s depth of field). R_{coef} is the reflection coefficient between the scatterer suspension fluid (seawater) and a flat polished SiO_2 crystal (Edmund Industrial Optics, Inc., Barrington, NJ, part 43424; $\rho = 2200 \text{ Kg/m}^3$, $c = 5720 \text{ m/s}$), and $R_{\text{ref}}(\omega)$ is the Fourier transform of the average reference signal. Reference signals were obtained using the specular reflection from the SiO_2 crystal placed at the transducer focus in seawater at room temperature. R_{coef} can be calculated using the acoustic impedances of the seawater and the SiO_2 crystal, and therefore it does not depend on the frequency ω . The number of points in the Fourier transforms was at least twice the number of samples in the corresponding signals. Only data from the -6 dB spectrum of the reference pulse were used in the analysis (10–62 MHz), which led to a high signal-to-noise ratio and avoided problems in division as a result of having small values in the denominator of equation (2.1). The average reference signal was obtained by superimposing and averaging 32 independent acquisitions of RF echo signals for each transducer. The values of the $|\text{BSTF}|^2$ are presented in the form of spectral plots expressed in decibels relative to the backscatter intensity from the reference (dBr).

These were compared with the theoretical backscatter frequency responses calculated for a fluid sphere using the Anderson model (1950), with a range of densities and sound speeds for the scattering sphere. A least squares analysis was used to determine the density and speed of sound for the fluid sphere that best agreed with the experimental response in the spectral domain. This was performed by minimizing, γ , the sum of the squares of the difference between theoretical and experimental values. Densities from 1140 Kg/m³ to 1260 Kg/m³ and speeds of sound from 1540 m/s to 1600 m/s were tried.

Table 2.1: Properties of the transducers used in the experiments.

Transducer	f-number	Focal length (mm)	Excitation Frequency (MHz)	-6 dB bandwidth (MHz)
20 MHz polyvinylidene fluoride	2.35	20	19	10 – 28
40 MHz polyvinylidene fluoride	3.00	9	40	21 – 51
80 MHz lithium niobate	3.00	6	55 ^a	40 – 62

2.2.2 Time domain Signal Reconstruction:

Previous studies of scattering from individual cells (Baddour *et al.*, 2005; Baddour *et al.*, 2007) focused on the analysis of experimental results in the frequency domain through the BSTF. The analysis of data in time domain provides additional insight into scattering behaviour of objects, such as ringing patterns and ring-down time. In this work, experimental and theoretical backscatter signals from sea urchin oocytes are presented and compared in both time and frequency domains. Given the experimental transmitted pulse and the theoretical backscatter frequency responses, the constructed time domain echo is given by:

$$r_{\text{theor}}(t) = \mathcal{F}^{-1}\{R_{\text{ref}}(\omega)\text{BSTF}_{\text{theor}}(\omega)\}, \quad (2.2)$$

where, $\mathcal{F}^{-1}\{\}$ is the inverse Fourier transform and $\text{BSTF}_{\text{theor}}(\omega)$ is the scattered echo of a homogeneous sphere insonified by a plane wave of unit amplitude (Anderson, 1950; Baddour *et al.*, 2005).

2.3 Results

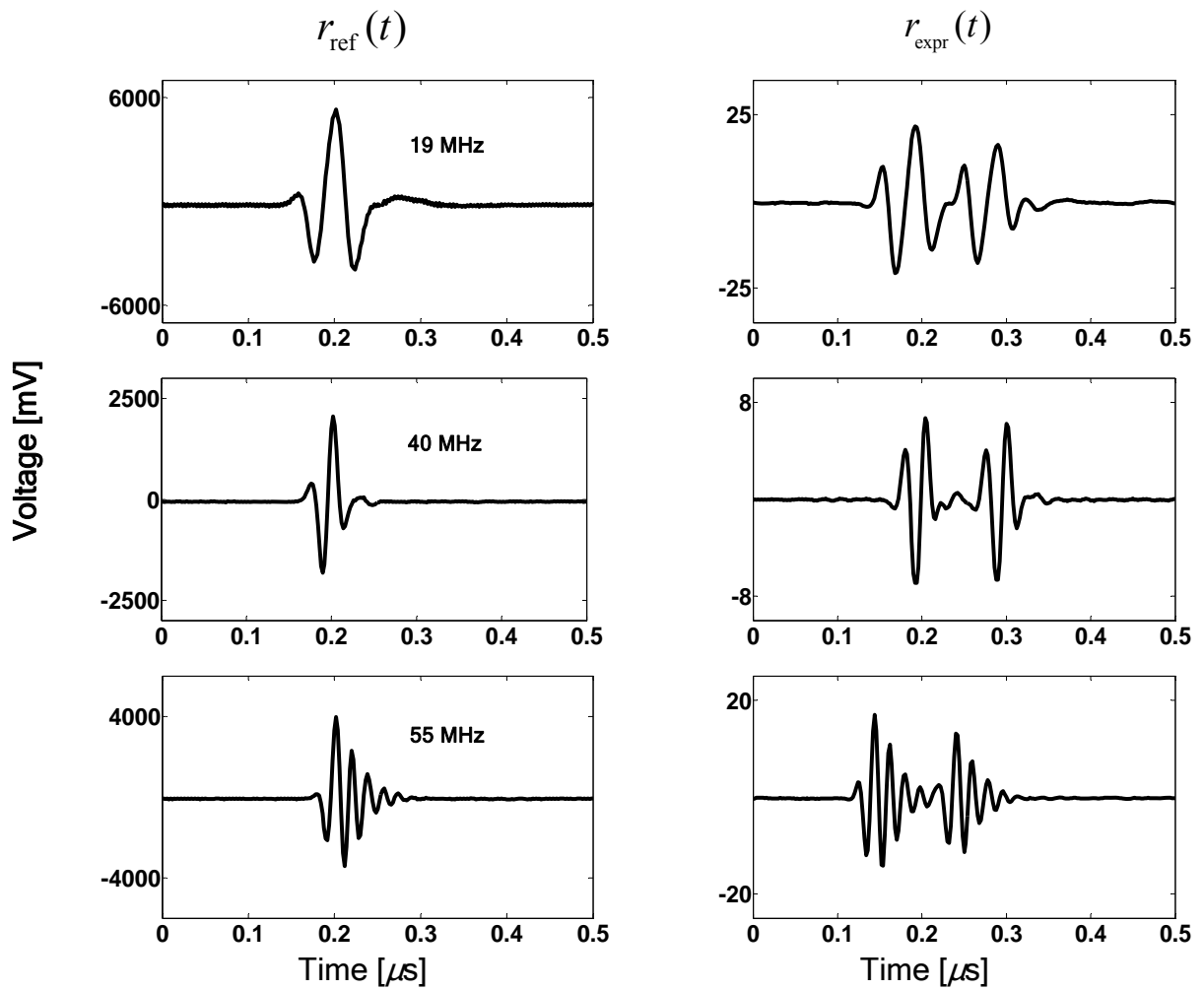


Figure 2.2: Average backscatter echoes from individual sea urchin oocytes and their corresponding incident pulses from three transducers: 20 MHz, 40 MHz, and 80 MHz excited at 19 MHz, 40 MHz, and 55 MHz, respectively.

Figure 2.1 shows the B-scan of sparse suspension of sea urchin oocytes in seawater at 40 MHz. Each pair of bright bands corresponds to the backscatter from a single oocyte. For each transducer, the average backscatter echoes from individual sea urchin oocytes and their corresponding average incident pulses are presented in Figure 2.2. Figure 2.3 shows the echoes from individual sea urchin oocytes at 40 MHz. The measured backscatter frequency responses within a range that corresponds to the -6 dB bandwidths of each transducer are plotted in Figure 2.4. The theoretical frequency backscatter response of a fluid sphere ($d=75$ μm , $c=1573$ m/s , $\rho = 1198$ Kg/m^3) is also shown in Figure 2.4.

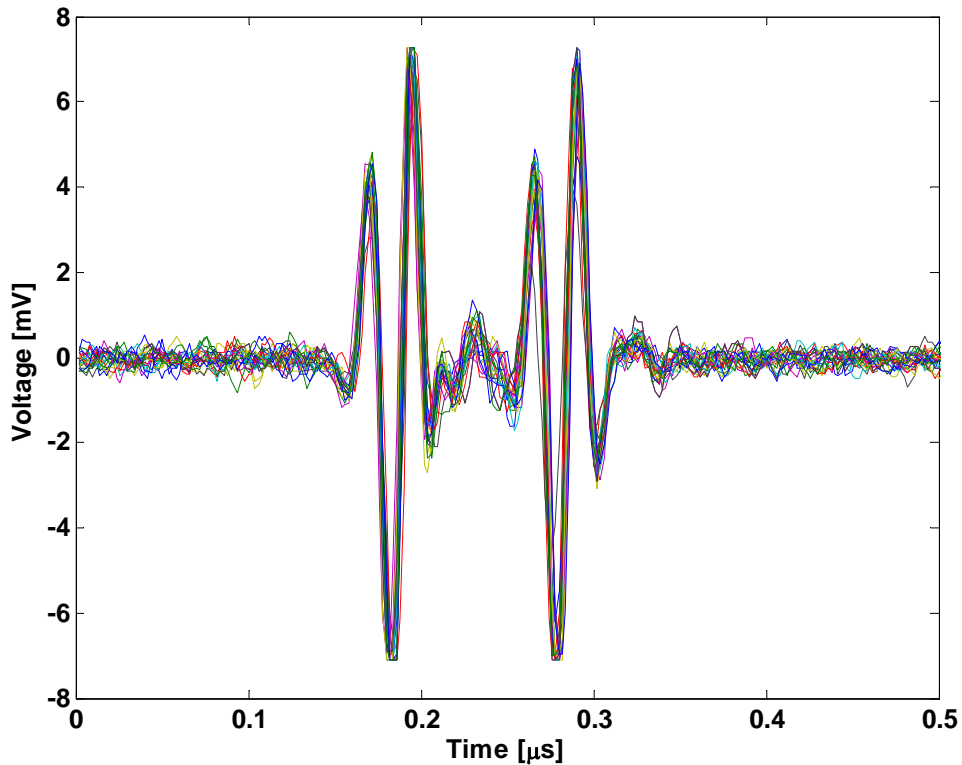


Figure 2.3: Echoes from individual sea urchin oocytes at 40 MHz. Each echo corresponds to scattering from a different oocyte. A little variation in the echoes is observed.

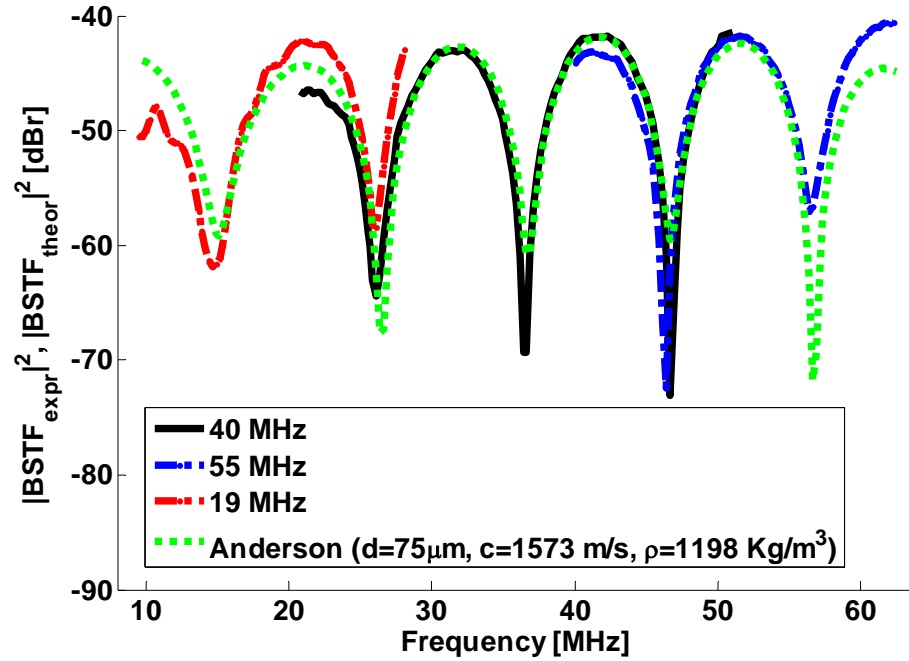


Figure 2.4: Theoretical and measured backscatter frequency responses of single sea urchin oocytes in seawater subject to three incident pulses from three transducers: 20 MHz, 40 MHz, and 80 MHz excited at 19 MHz, 40 MHz, and 55 MHz, respectively.

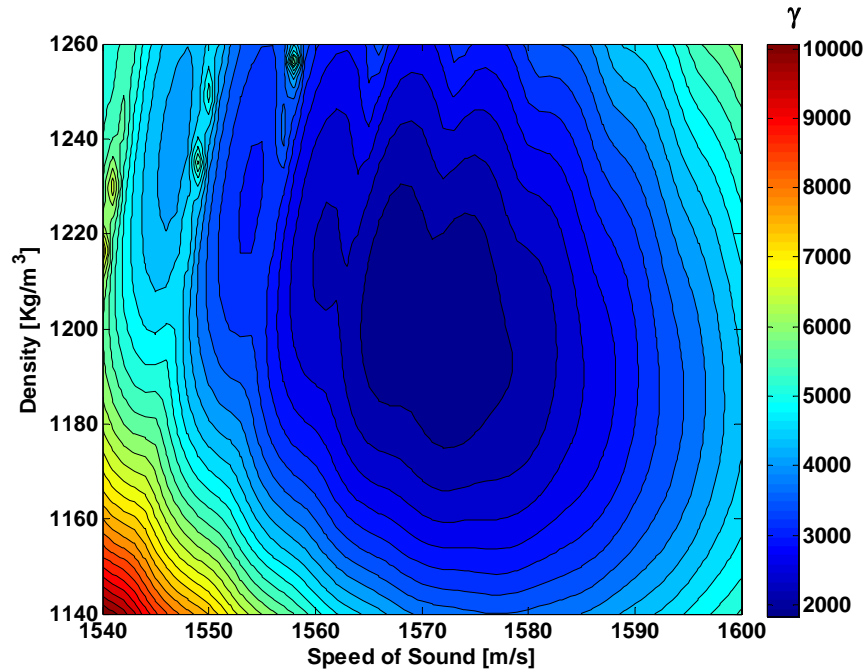
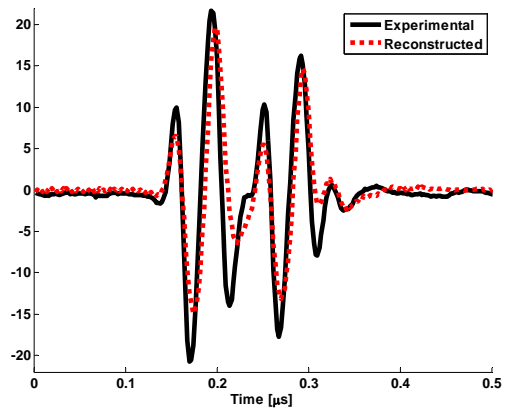
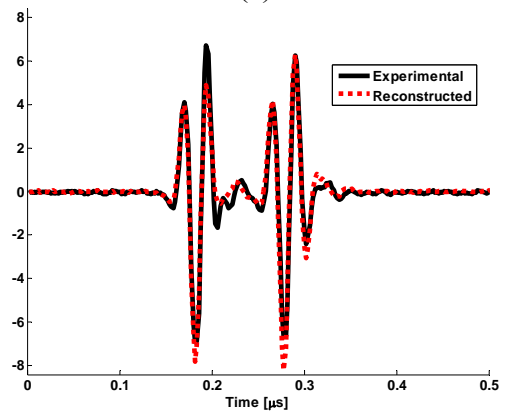


Figure 2.5: Contour plot of the least square fit coefficient of the experimental and theoretical backscatter transfer functions as a function of the sphere density and speed of sound. \mathcal{J} is the sum of the squares of the difference between theoretical and experimental values.

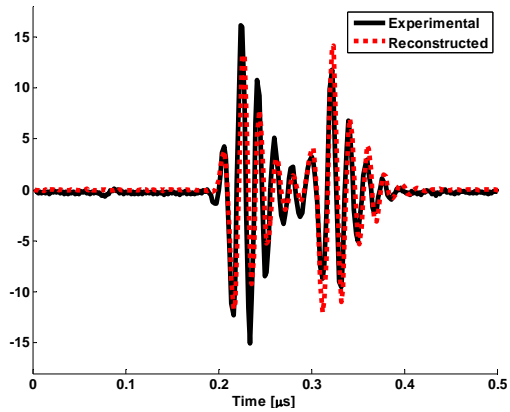
Voltage [mV]



(a)



(b)



(c)

Figure 2.6: Average experimental and reconstructed (given the experimental transmitted pulse and the theoretical backscatter frequency responses) echoes from individual sea urchin oocytes at a) 19 MHz, b) 40 MHz, and c) 55 MHz. Note that the reflection off the front and back surface is similar to the incident pulse and there is no phase reversal at the back surface.

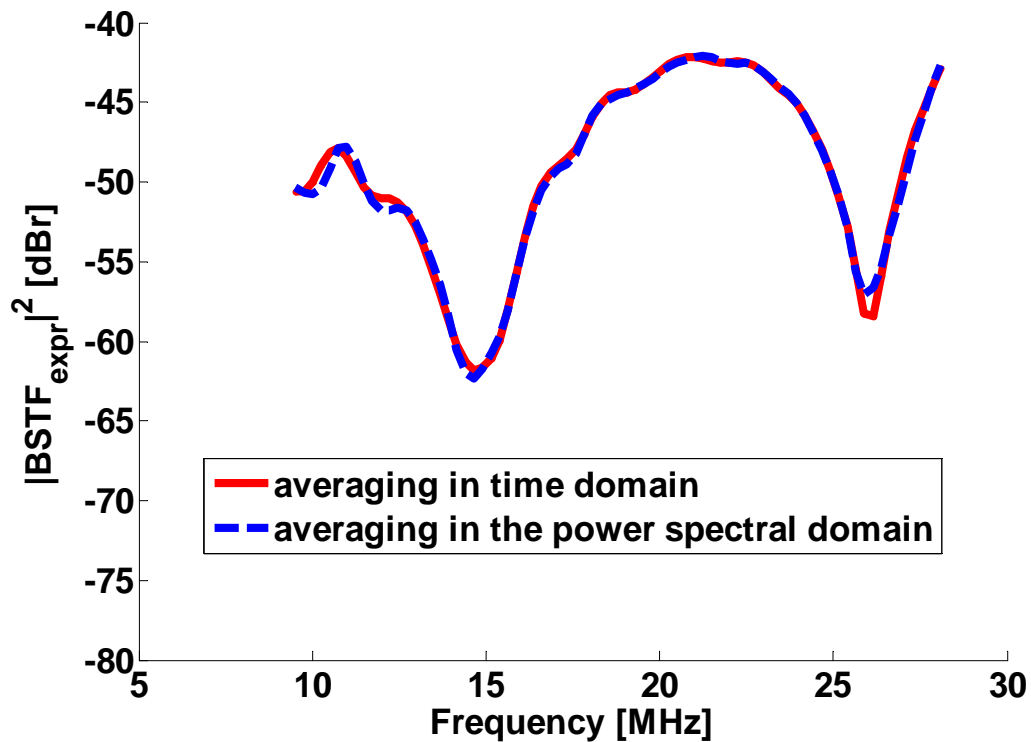


Figure 2.7: Comparison of the difference in averaging RF lines in time and in power spectral domains for the 20 MHz transducer.

A theoretical density of 1198 Kg/m^3 and speed of sound of 1573 m/s for the oocyte were found to have the best fit to experimental data as shown in Figure 2.5. These values are comparable to the density of blood cells (1125 Kg/m^3) and speed of sound in blood (1570 m/s), respectively (Macovski, 1983; Kenner, 1989). The average experimental and reconstructed signals from individual sea urchins oocytes from the 19 MHz, 40 MHz, and 55 MHz transducers are presented in Figure 2.6. A comparison of the difference in averaging RF lines in time and in power spectral domains for the 19 MHz transducer is shown in Figure 2.7.

2.4 Discussion and Conclusions

There is a very good agreement in the locations of maxima and minima as shown in Figure 2.4. The difference has been measured to be less than 1% on average in the locations of maxima and minima between the theoretical frequency response of a fluid sphere and the measured backscatter frequency response of individual sea urchin oocytes. The presence of many ripples in the experimental data collected using the 20 MHz transducer may be due to relatively low number of RF lines left (5 of them) after discarding inappropriate scans (as described in section 2.2.1). This suggests that most of the oocytes in the solution were not located within the -6 dB focal volume of the transducer in the particular experiment. The overall agreement shown in Figure 2.4 suggests that sea urchin oocytes can be best modeled as fluid sphere. These findings are not surprising since sea urchin oocytes have no membrane delimited nucleus and have a spherical shape (inset in Figure 2.1).

The incident pulses and backscatter echoes for each transducer (Figure 2.2) reveal that sea urchins are very weak scatterers (peak of echoes from quartz plate were ~ 300 times $[-49.5$ dB] larger than that of the backscatter echoes). No ringing pattern was observed which indicates the absence of detectable shear waves inside the oocytes, a further indication of their fluid-like nature. Scattering seems to occur off the front and back surfaces of the sea urchin oocytes as shown in the B-scan image (Figure 2.1). The backscatter echo is composed of two pulses which can be easily distinguished for the 40 MHz transducer. The peak-to-peak separation of the latter is $0.096 \mu\text{s}$ which corresponds to a round-trip distance of $150 \mu\text{m}$ (the distance was found by multiplying the peak-to-peak separation by the speed of sound in the oocyte), or approximately twice the mean

diameter of the oocytes. These findings further strengthen the argument that the oocytes can be modeled as fluid spheres.

A good agreement was found in the time domain between the experimental and reconstructed echoes from individual oocytes, as shown in Figure 2.6. The maxima/minima that are larger than ± 1 [V] align temporally with insignificant error. Their values agree to an average error of 56%, 24%, and 59% for the 19 MHz, 40 MHz, and 55 MHz data, respectively. These average errors are not surprising given the discrepancies between the theoretical and experimental spectral plots (Figure 2.4). It should be pointed out that a more rigorous method of demonstrating pulse coherence (Krishnan *et al.*, 1997) could have been used instead of the simple method described above. However, since the signal-to-noise ratio of the oocyte backscatter was high, a simple method was sufficient to demonstrate the similarities between the experimental and reconstructed echoes from individual oocytes. In macroscopic models of wave propagation, a phase inversion occurs in the reflection at the boundary between two media when a wave travels from a region with higher acoustic impedance to lower impedance. The experimental RF data (Figure 2.6) does not exhibit this phase reversal at the back surface of the oocyte (where the wave travels from higher to lower impedance). These results suggest that, although scattering mainly occurs at the surrounding medium–oocyte interfaces, a complete scattering model, such as that of Anderson, is needed to predict the scattered field from spherical objects.

It is worth mentioning that obtaining an average representation of the backscatter echo from an individual sea urchin oocyte was the main reason for doing the averaging in the time domain instead of the power spectral domain so that experimental and reconstructed echoes can be

compared (Figure 2.6). Had the averaging not been done in the time domain, the reconstruction algorithm would have had to be validated by comparing the reconstructed echo with an arbitrary RF echo instead of the average experimental echo. Since oocytes have a very narrow size distribution and a 90% thresholding was applied, the resulting RF lines are very likely to represent the backscattering events of sea urchins within the resolution volume of the transducer at the time of imaging. To confirm this further, averaging in the time and in the power spectral domains were compared for the 19 MHz transducer. It is expected that averaging in the time and frequency domain would produce equivalent results since RF lines were aligned before averaging and a narrow bandwidth (10–62 MHz) was examined as shown in Figure 2.7.

In conclusion, the backscatter response from sea urchin oocytes were measured and compared to theoretical predictions for a fluid sphere (Anderson model). Very good agreement was found between the experimental and theoretical results in the frequency domain (difference less than 1% on average) suggesting that the backscatter response from a sea urchin oocyte is best modeled as a fluid sphere. This work confirms the fluid behaviour of the non-nucleated biological specimens used in this study at high ultrasound frequencies. It also establishes an objective methodology to determine the appropriate theoretical model of the properties of individual cells as ultrasound scatterers.

Chapter 3

The measurement of ultrasound scattering from individual micron-sized objects and its application in single cell scattering²

3.1 Introduction

The measurement of the ultrasound backscatter from individual micron-sized objects such as cells is needed for applications ranging from tissue characterization to molecular imaging. This has been previously done by scanning a sample with objects in suspension and analyzing the brightest signals received, assuming these to be caused by scattering events from the single objects of interest (Baddour *et al.*, 2005; Baddour *et al.*, 2007; Falou *et al.*, 2008). This technique is error-prone since the bright signals may be from unwanted particles in the suspension, aggregates of the objects of interest (e.g. a cluster of cells), or from air bubbles, which are hard to eliminate from fluid suspensions. This work introduces a new

² The work presented in this chapter has been published as: Falou, O., Rui, M., El Kaffas, A., Kumaradas, J. C., and Kolios, M. C. (2010), “The Measurement of Ultrasound Scattering from Individual Micron-sized Objects and its Application in Single Cell Scattering,” *Journal of the Acoustical Society of America* 128(2), 894–902. It was also selected for publication in the 2010 *Virtual Journal of Biological Physics Research*, 20(4).

technique, consisting of a microinjection system and co-registered optical and ultrasonic imaging devices to measure the ultrasound backscatter from single micron-sized objects.

It has been shown that high frequency ultrasound (20–60 MHz) can be used to detect structural and physical changes in cell ensembles during cell death through apoptosis (Czarnota *et al.*, 1997; Czarnota *et al.*, 1999; Kolios *et al.*, 2004). Ultrasonic backscatter from cell ensembles treated with the chemotherapeutic drug cisplatin (which induces apoptosis) increase the ultrasound backscatter signal amplitude by 9–13 dB and lead to changes in the frequency dependence of backscatter. Recent studies showed similar effects after cancer radiotherapy *in vitro and in vivo* (Vlad *et al.*, 2008; Vlad *et al.*, 2009).

When compared to clinical ultrasound imaging (1–10 MHz), high frequency ultrasound imaging, whose wavelength approaches the size of the cell, is more sensitive to cell structural and spatial distribution changes (Hunt *et al.*, 2002; Tunis *et al.*, 2005). The long term goal of this work is to use high frequency ultrasound imaging to determine the apoptotic index, the percentage of cells in a volume undergoing apoptosis, which will help in quantifying patient response to cancer treatment. However, a theoretical model of ultrasound scattering from cell ensembles is required in order to determine the proportion of cells undergoing apoptosis in a tumour and hence assess the effectiveness of therapy.

Most scattering models used for lower frequency ultrasonic tissue characterization assume a random distribution of scatterers and a Gaussian-like variation in tissue acoustic properties (Lizzi *et al.*, 1983; Insana *et al.*, 1990; Oelze *et al.*, 2002). These models have been used to diagnose various tissue pathologic states (Lizzi *et al.*, 1988; Lizzi *et al.*, 1997; Ursea *et al.*, 1998; Feleppa *et al.*, 2000; Mamou *et al.*, 2006). However, most tumour tissues exhibit non-random spatial cell distributions, and hence the need for more accurate scattering

models. A prerequisite to these models is the understanding of the backscatter responses at the cellular level.

Recently, Baddour *et al.* (2005; 2007) performed measurements of high frequency ultrasound backscatter responses from single eukaryotic cells in suspension. They found that for prostate carcinoma (PC-3) cells whose nucleus to cell volume ratio is 0.33, the ultrasound backscatter could be modeled as a fluid sphere (Baddour *et al.*, 2007). Falou *et al.* (2008) presented similar findings for non-nucleated biological specimens, such as sea urchin oocytes. However, for human acute myeloid leukemia (OCI-AML-5) cells whose nucleus to cell volume ratio is 0.5, Baddour *et al.* (2007) found that the ultrasound backscatter response could not accurately be modeled as a fluid sphere. They hypothesized that for cells with low nucleus to cell volume ratios (e.g. PC-3), the backscatter response can be modeled as a fluid sphere. However, for cells with a nucleus to cell volume ratio of 0.5 (e.g. OCI-AML-5), the backscatter response is better modeled as an elastic sphere. During their experiments, no visual confirmation of the underlying scattering structures could be made, as the ultrasound measurements were done with cells in suspension. In addition, the possible presence of air bubbles in the suspension of cells may have led to the incorrect interpretation of the measured ultrasonic signals.

In this work, a new technique is developed to measure the ultrasonic backscatter response from individual micron-sized objects, particularly OCI-AML-5 cells. This method allows the optical detection of the scattering objects responsible for the backscatter responses measured by the ultrasound imaging devices as optical videos of the scattering objects are made during the ultrasound acquisition. Using this new set-up, the ultrasonic behaviour of

acute myeloid leukemia cells was investigated by comparing the measured backscatter response to theoretical predictions from a fluid sphere model (Anderson, 1950).

3.2 Technique description and validation

3.2.1 Methods

A XenoWorks microinjection system (Sutter Instrument Company, Novato, CA) consisting of a digital microinjector, a micromanipulator, and a P-97 micropipette puller was used. The system uses custom tailored micropipettes with pressure values ranging from -35 kPa to $+35$ kPa, controllable in 0.7 kPa increments, applied along the surface of the object of interest. Fire-polished thin wall borosilicate micropipettes of length, outer diameter, and inner diameter of 10 , 1 , and 0.78 mm, respectively (Sutter Instrument Company, catalog number: BF100-78-10) were pulled to form tips of outer and inner diameters of 5 μm and 3 μm , respectively. The micropipette movement was controlled by a joystick with a translational precision of $50/100$ μm at the pipette tip for every full rotation/swing of the joystick, along each of the x , y , and z axes. A Retiga EXi CCD camera (QImaging, Inc., Surrey, BC) mounted on an Olympus IX71 inverted microscope (Olympus America, Inc., Center Valley, PA) and a VEVO770 Ultrasound imaging device (VisualSonics, Inc., Toronto, ON) were used to capture optical and ultrasonic data, respectively. Both devices were connected to a PC loaded with StreamPix 3 (NorPix, Inc., Montreal, QC), a digital video recording software and the image analysis tool, ImageJ (<http://rsbweb.nih.gov/ij/>), which allowed for the capturing of optical movies (frame rate of 9 frames per second) and size measurements of the

object of interest. The MATLAB 7 software package (The MathWorks, Inc., Natick, MA) was used to process the ultrasonic data as shown in Figure 3.1.

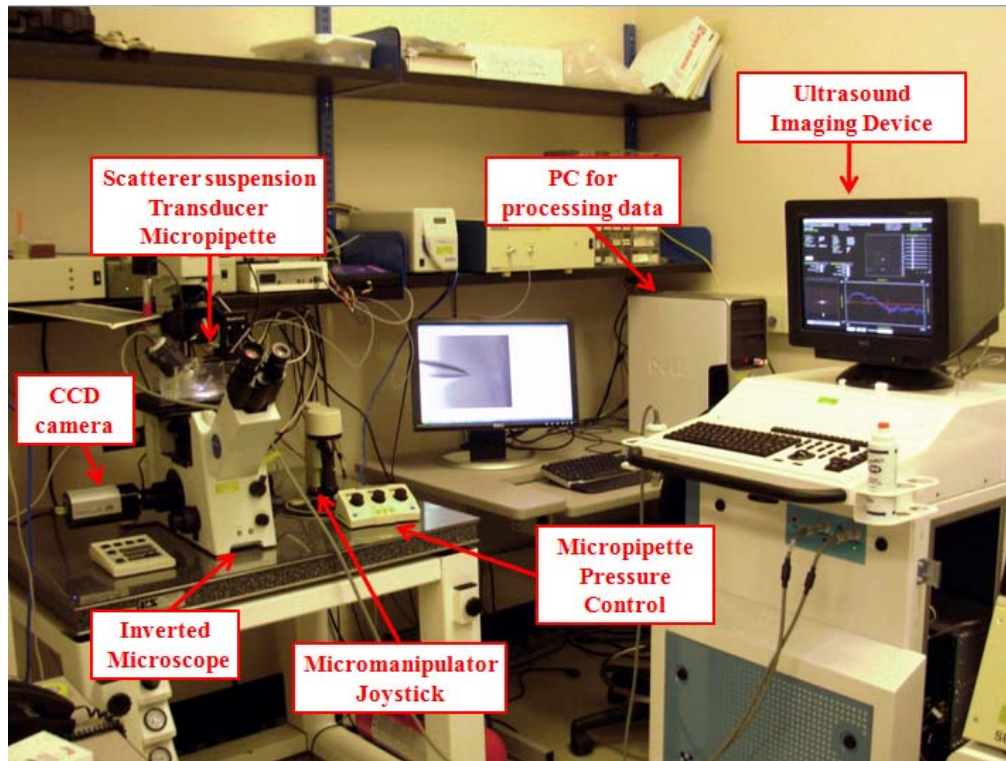


Figure 3.1: Experimental setup composed of a XenoWorks microinjection system consisting of a digital microinjector, a micromanipulator, and a micropipette puller. A CCD camera mounted on an Olympus IX71 inverted microscope and a VEVO770 ultrasound imaging device were used to capture optical and ultrasonic data. Both devices were connected to a PC which allowed for the capturing of optical movies and the processing of ultrasonic data.

Table 3.1: Properties of the transducers used in the experiments.

Transducer	f-number	Focal length	-6 dB bandwidth
		(mm)	(MHz)
25 MHz polyvinylidene fluoride	2.1	15	12–28
55 MHz polyvinylidene fluoride	2.25	4.5	25–57

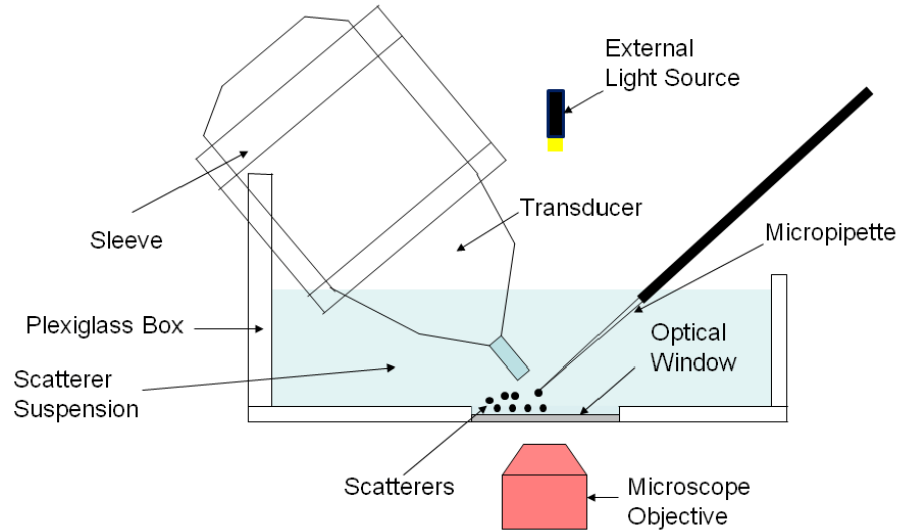


Figure 3.2: Schematic diagram of the scatterer suspension setup. A suspension of the scatterer was placed in a custom made container. The micropipette and the transducer are held perpendicular to one another.

Ultrasonic data acquisition was performed using a VEVO770 ultrasound imaging device. Radiofrequency data were collected at a sampling rate of 420 MHz. Two broadband focused Polyvinylidene Fluoride transducers, with different resonant frequencies, f-numbers, and focal lengths, were employed. Table 3.1 summarizes the properties of the two transducers. Only data from the -6 dB bandwidth of each transducer were used in the analysis which gave an overall bandwidth spanning 12–57 MHz.

A sparse suspension of the scatterer was prepared at room temperature by mixing a very low concentration of scatterers (between 1000 to 10,000 scatterers/mL) into 250 mL of the suspending fluid. The suspension was placed in a custom made container made of plexiglass. The container has a two inch optical window in the bottom and a sleeve which holds the ultrasound transducer at 45 degrees from the vertical as shown in Figure 3.2. The transducer axis pointed just above the centre of the window and the transducer could be

translated along its axis to adjust for a variable focal length. The centre of the window was positioned at the focal point of the optical microscope and an individual scattering object was held with the micropipette at the same position. In this manner, optical and ultrasound images were obtained at the same time. The long axis of the micropipette and the transducer axis were oriented perpendicular to one another. This orientation was important in order to minimize the ultrasonic signal from the micropipette. Initially, the micropipette was brought to the focus of the transducer and its location was saved. It was then translated to the bottom of the container and brought in close proximity of the scatterer. The scatterer was then attached to the micropipette under optical guidance using a pressure ranging from -18.9 kPa to -9 kPa. The micropipette was transferred back to its saved location and the scatterer was released (by using positive pressure of $+35$ kPa and/or tapping gently on the micropipette) while simultaneously imaging it optically and ultrasonically. Ultrasonic data acquisition was initiated prior to the release of the scatterer from the pipette.

30 ultrasonic raw RF lines spaced $55-70 \mu\text{m}$ apart were acquired from different lateral positions for each ultrasound frame and their corresponding B-scans, represented by the matrix $H_{\text{expr}_f}(t)$, were constructed using the following equation:

$$H_{\text{expr}_f}(t) = \ln \left(\left| \mathcal{H} \left\{ r_{\text{expr}_f}(t) \right\} \right| \right), \quad (3.1)$$

where $\mathcal{H} \{ \}$ is the Hilbert transform and $r_{\text{expr}_f}(t)$ is the matrix containing measured RF lines for a series of frames. Visual inspection was performed to determine the frames that contained a scatterer. Once a frame containing a scatterer was found, the RF line containing the maximum amplitude was chosen and a hamming window centered at that amplitude was applied in order to minimize the scattering from the micropipette. Figure 3.3 illustrates the

steps taken to deduce the RF line containing the pulse from a single scatterer (in this example, OCI-AML-5 cell) suspended in degassed PBS. It shows representative optical images, B-scans, and ultrasonic echoes at 55 MHz of a micropipette before and after the release of scatterer. Optical images and B-scans of the region of interest, containing the pipette and the scatterer before and after the release of the scatterer are given in Figure 3.3(a), 3.3(b), 3.3(c), and 3.3(d), respectively. Figures 3.3(e) and 3.3(f) illustrate the backscattered pulses at the dashed lines in Figures 3.3(c) and 3.3(d), respectively. The backscatter transfer function, $BSTF_{\text{expr}}(\omega)$, was calculated using equation (2.1). In this work, Dow Corning 710 fluid (Applied Industrial Technologies, Cleveland, OH, Part number: 710 4KG PL; $\rho = 1.11 \text{ g/cm}^3$, $c = 1370 \text{ m/s}$) was used instead of the SiO_2 crystal during the measurement of the reference signals. Two different suspension fluids were used in the experiments depending on the scatterer. The $|BSTF|^2$ are presented in the form of spectral plots expressed in decibels relative to the backscatter intensity from the reference(dBr). The above procedure was repeated until successful measurements of the BSTF were achieved. This method for measuring the backscatter transfer function of micron-sized object was tested with a $20 \mu\text{m}$ diameter polystyrene microspheres (Beckman Coulter, Inc., Brea, CA, ref. number: 6602798). These were used because they are homogeneous, spherical, and have well-known physical properties. Table 3.2 gives the physical properties of polystyrene.

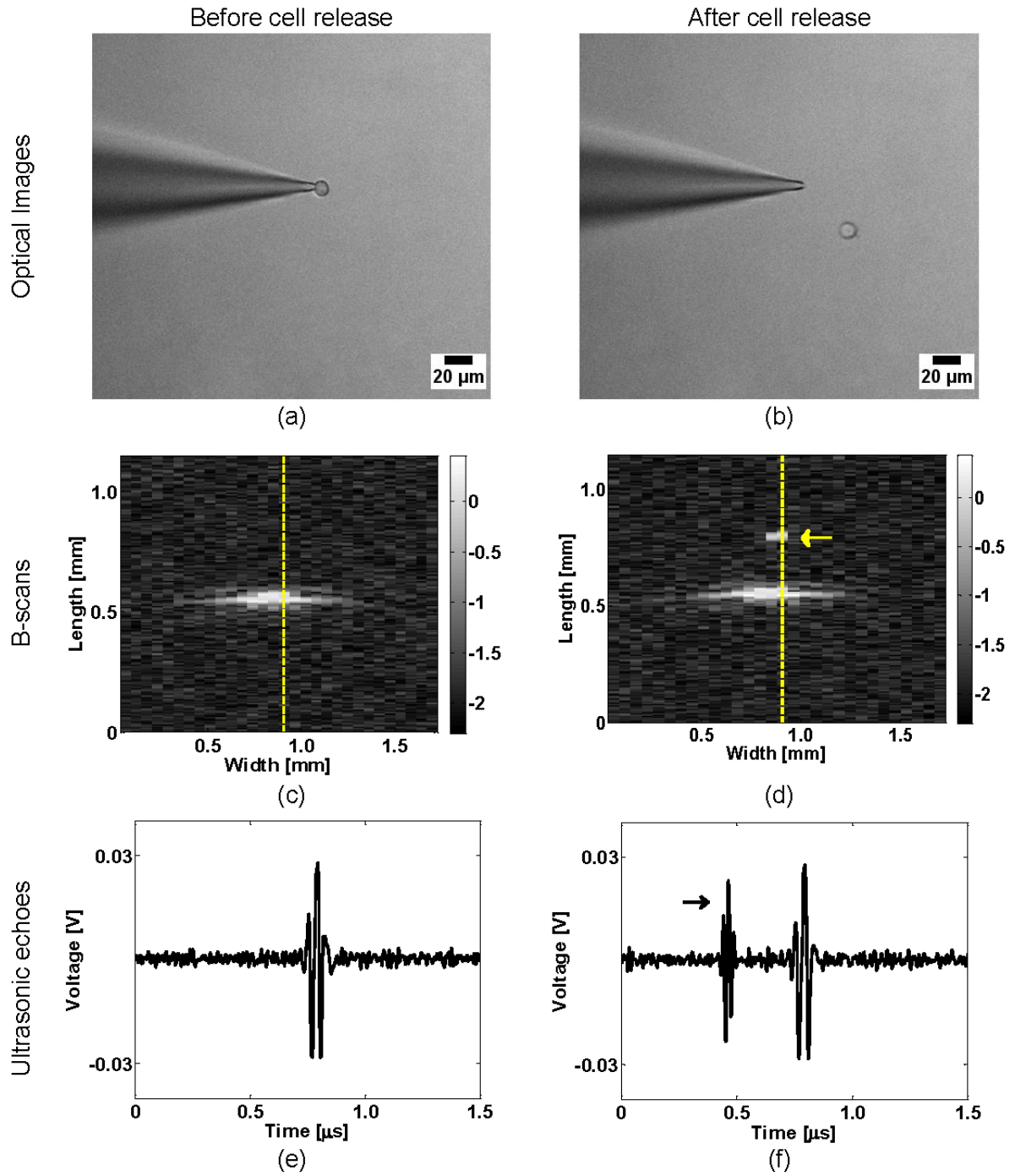


Figure 3.3: Representative optical images, B-scans, and ultrasonic echoes at 55 MHz of a micropipette before [(a),(c),(e)] and after the release of a scatterer (OCI-AML-5 cell) [(b),(d),(f)]. (c) and (d) are the B-scans of the region of interest, containing the pipette and the released scatterer. (e) and (f) represent the backscattered pulses at the dashed lines in figures (c) and (d), respectively. The arrow points to the scatterer in (d) and the RF echo from the scatterer in (f).

Table 3.2: Polystyrene physical properties

Property	Value
Density (ρ)	1050 kg/m ³
Compressional speed of sound (c)	2350 m/s
Young's Modulus (E)	3.61 GPa
Poisson's Ratio (ν)	0.35

The microspheres were suspended in distilled and degassed water ($\rho = 1.0$ g/mL, $c = 1483$ m/s) at room temperature. Hamming windows of $0.83 \mu\text{s}$ and $0.95 \mu\text{s}$ widths were applied to the 25 and 55 MHz backscatter measurements, respectively, to localize and isolate the signal from the microsphere. The backscatter transfer function, $|\text{BSTF}|^2$, was determined from the measured data and compared to the theoretical backscatter frequency responses calculated for an elastic sphere using the Faran scattering model (Faran, 1951) to validate the new method.

3.2.2 Results

Figure 3.4 shows representative backscatter echoes from a single $20 \mu\text{m}$ polystyrene microsphere in degassed and distilled water and their corresponding incident pulses at 25 and 55 MHz. The theoretical and averaged experimental backscatter responses within a range that corresponds to the -6 dB bandwidths of each transducer are plotted in Figure 3.5. For the theoretical calculations, the elastic sphere was assumed to have the parameters: $\rho = 1.05$ g/mL, $c = 2350$ m/s, $\nu = 0.35$, where ν is the Poisson's ratio.

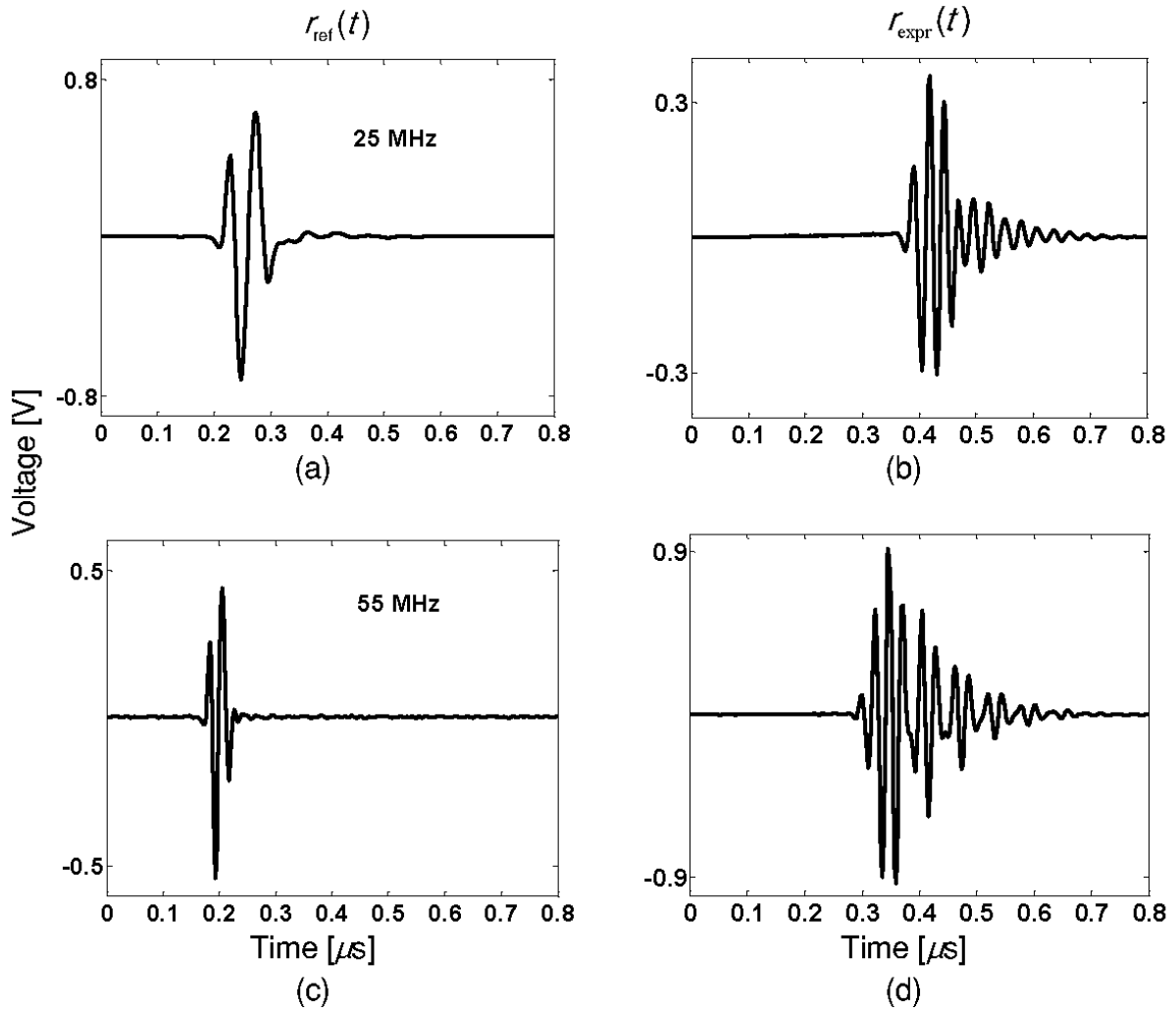


Figure 3.4: Representative backscatter echoes from a 20 μm polystyrene microsphere and their corresponding incident pulses (as measured by the reflection from the surface of Dow Corning fluid at the transducer focus): incident pulses at (a) 25 MHz and (c) 55 MHz; echoes from a 20 μm polystyrene microsphere at (b) 25 MHz and (d) 55 MHz.

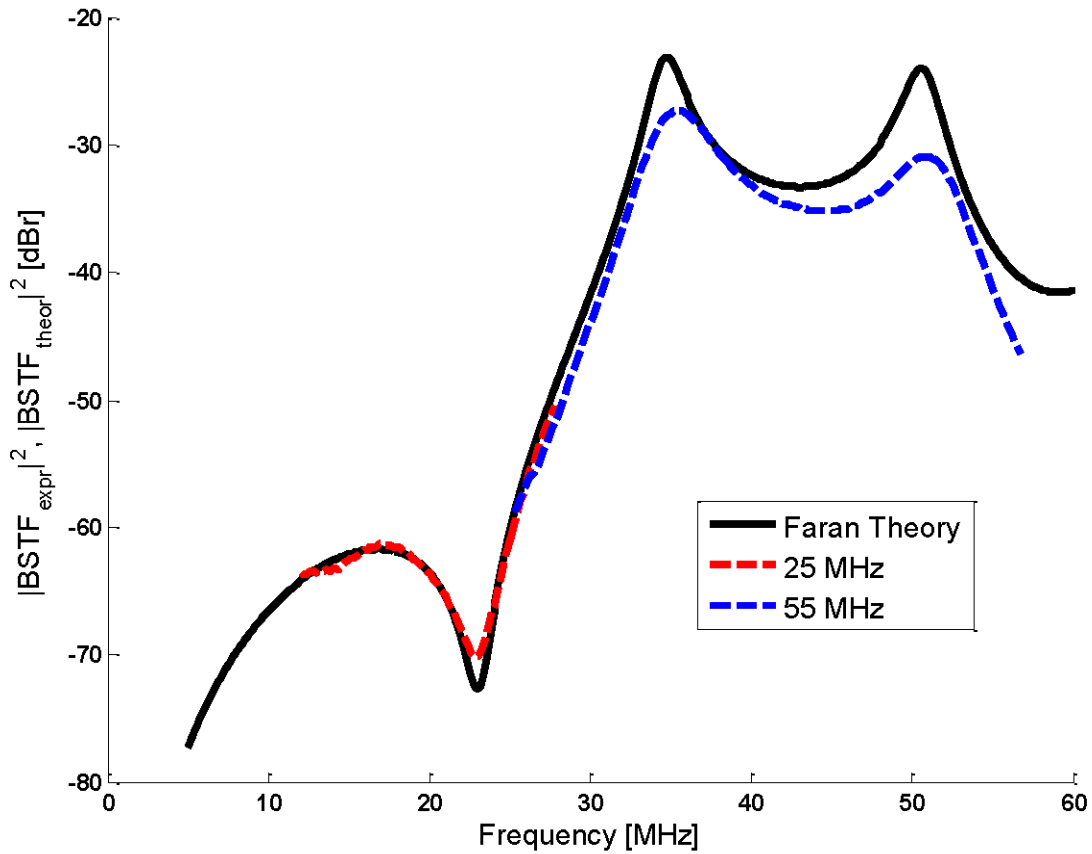


Figure 3.5: Theoretical and experimental backscatter frequency responses of a single $20 \mu\text{m}$ polystyrene microsphere in degassed and distilled water subject to incident pulses from two transducers: 25 MHz and 55 MHz (Elastic sphere model parameters: $\rho = 1.05 \text{ g/mL}$, $c = 2350 \text{ m/s}$, $\nu = 0.35$).

3.2.3 Discussion

The measurement of the ultrasonic response from individual micron-size objects, such as biological cells (weak scatterers) and ultrasound contrast agents (strong scatterers), is required for various applications ranging from ultrasound tissue characterization to molecular imaging. Yet, performing such a measurement remains a challenge. For instance, the possible presence of air bubbles or other foreign objects in a suspension of scatterers during the measurements may lead to the incorrect interpretation of the backscattered signals. Spurious air bubbles were repeatedly seen in the experiments in this work despite my best effort to

degas the solutions in which the experiments were done. In addition, the size and shape of the individual object that produces an ultrasound signal are required as input parameters to theoretical models, yet these are hard to be measure experimentally. This novel technique combining a microinjection system and co-registered optical and ultrasonic imaging devices (Figure 3.1) made it possible to deduce the experimental ultrasound backscatter response from micron-sized objects under optical guidance.

A very good agreement was found between the measured backscatter responses of individual microspheres and theoretical predictions of an elastic sphere recording theoretically predicted gradients of 43dB/13MHz as shown in Figure 3.5. The difference was measured to be less than 1% on average in the locations of maxima and minima between the experimentally measured backscatter frequency response of individual microspheres and the theoretical frequency response of an elastic sphere. For the 55 MHz data, the experimental curve has lower values for the $|\text{BSTF}|^2$ than that of the theoretical one, particularly at the resonance frequencies. This may be due to the increase of the attenuation at high frequencies. The lower value of the $|\text{BSTF}|^2$ for the second resonant peak (55 MHz) in the experimental backscatter response when compared to the first peak (35 MHz) is a further indication of the increased effect of attenuation in the backscatter response at high frequencies. This was further confirmed by calculating the difference in the $|\text{BSTF}|^2$ at these resonant peaks. The difference was found to be ~ 3 dB which is equivalent to the difference in the attenuation in water at these frequencies (Mordfin, 2002).

An examination of the backscatter echoes from the polystyrene microsphere (Figure 3.4) reveals the presence of resonances exhibited in the form of ringing patterns. The

ring-down durations for such patterns are of 0.3 and 0.4 μs for the 25 and 55 MHz data, respectively. Such findings are further indications of the resonant behaviour of microspheres, which agree well with the Faran's scattering model for elastic spheres (Faran, 1951) and have been measured in the past (Baddour *et al.*, 2005).

3.3 Scattering from cells

The OCI-AML-5 cells were prepared in a degassed and dilute phosphate buffered saline (PBS) solution (in distilled water: 8 g/L sodium chloride, 0.20 g/L potassium chloride, 0.20 g/L potassium phosphate, 1.15 g/L sodium phosphate, 0.132 g/L calcium chloride, 0.10 g/L magnesium chloride). PBS (assumed to have the same density and speed of sound as those of distilled water) was used since it is non-toxic to cells and it has an osmolarity and ion concentrations critical to cell survival. Hamming windows of 0.33 μs and 0.24 μs widths were applied to the 25 and 55 MHz backscatter measurements from the cells, respectively, to localize and isolate the signal from the cell. The experimental procedure was repeated until eight successful trials were collected. Since the mass density of an OCI-AML-5 cell is unknown, the individual measured $|\text{BSTF}|^2$ of a cell in each trial was compared to the theoretical backscatter frequency response calculated for a fluid sphere using the Anderson model (Anderson, 1950), with a diameter as measured optically (Vlad *et al.*, 2008), a sound speed of 1535 m/s (Taggart *et al.*, 2007), and a range of densities from 1.0 g/mL to 1.2 g/mL for the cell. The least squares method was used to determine the mass density that produced the best agreement with their corresponding experimental responses, as detailed in Falou *et*

al. (2008). The measured optical diameters and theoretical densities were averaged and used to plot the averaged theoretical fit to experimental data.

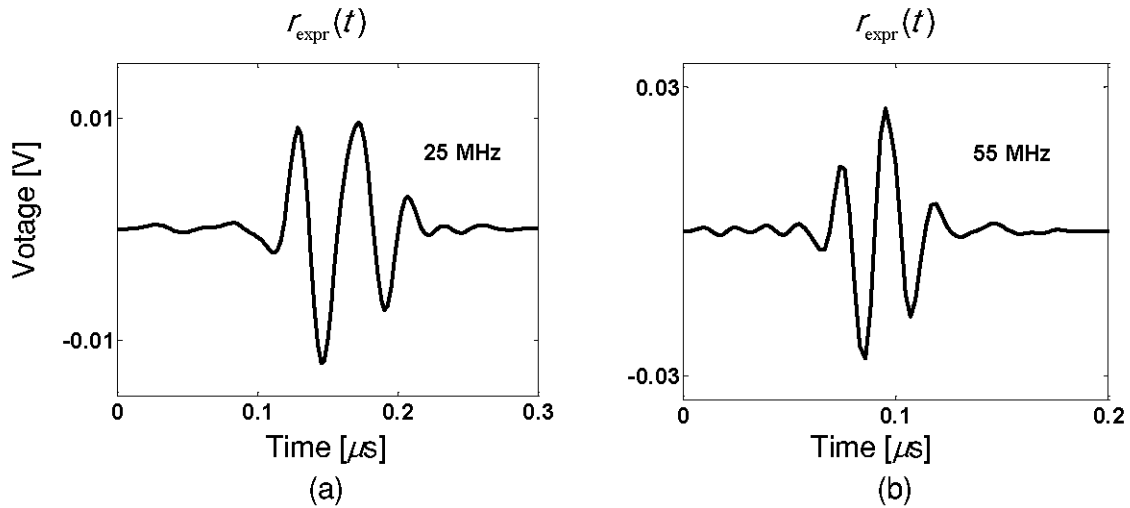


Figure 3.6: Representative backscatter echoes from an OCI-AML-5 cell imaged at (a) 25 MHz and (b) 55 MHz.

Representative backscatter echoes from individual OCI-AML-5 cells imaged at 25 MHz and 55 MHz are shown in Figure 3.6 . Figure 3.7 and Figure 3.8 show the best fitted theoretical (assuming a fluid sphere model) and experimental backscatter frequency responses (within the -6 dB bandwidths of the transducer) of an individual OCI-AML-5 cell in PBS subject to incident pulses from 25 and 55 MHz transducers, respectively. Figure 3.9 shows the theoretical (Fluid sphere model parameters: $d = 11.2\mu\text{m}$, $\rho = 1.09\text{ g/mL}$, $c = 1535\text{ m/s}$) and the average experimental backscatter frequency responses of a single OCI-AML-5 cell in PBS subject to incident pulses from two transducers: 25 and 55 MHz. Error bars represent the 95% confidence intervals.

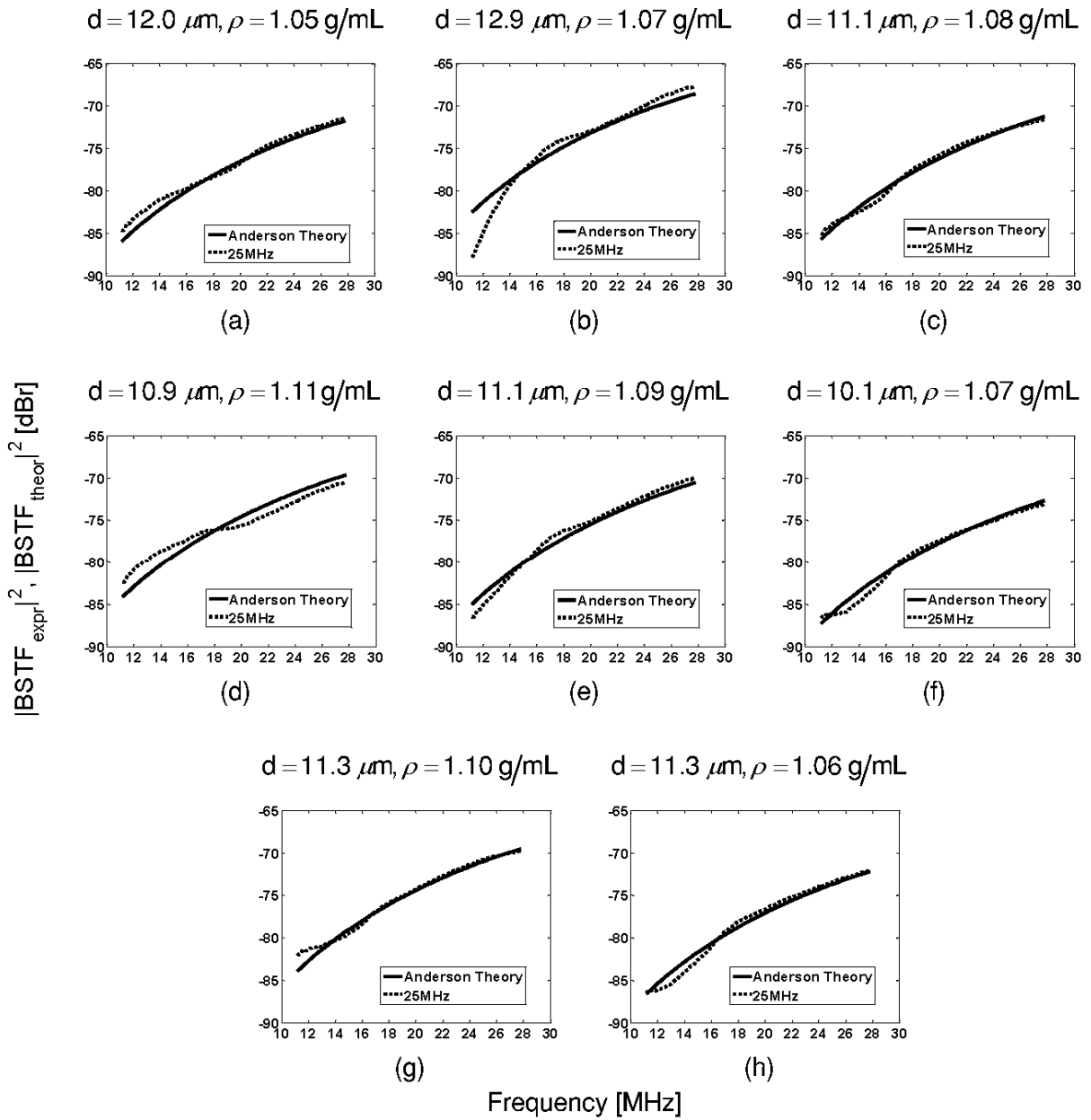


Figure 3.7: Theoretical (Fluid sphere model: $c = 1535 \text{ m/s}$, diameter and density are given in the figure title) and experimental backscatter frequency responses of a single OCI-AML-5 cell in PBS subject to incident pulses from a 25 MHz transducer. Each part in the figure represents a backscatter measurement from an individual different cell.

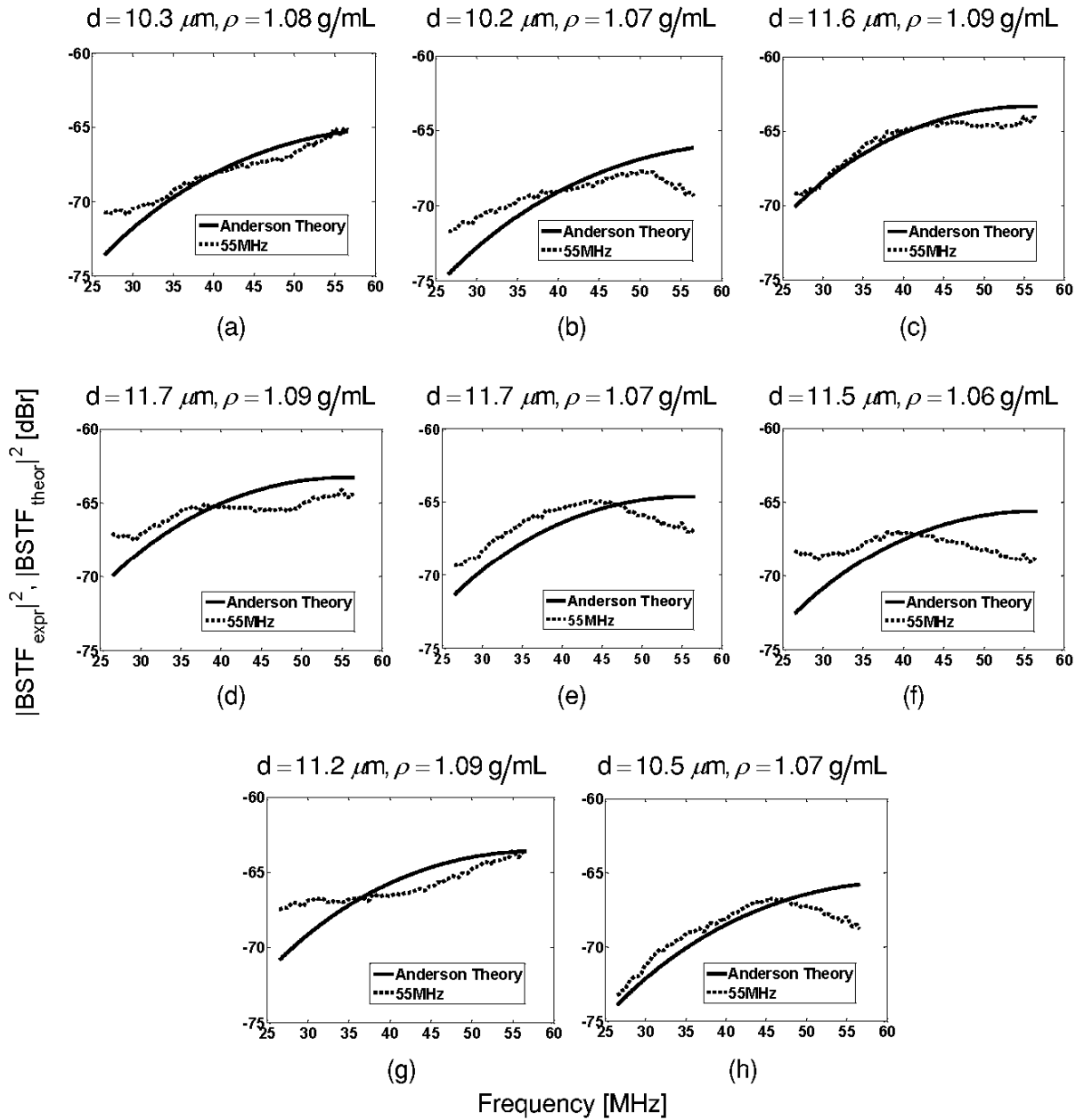


Figure 3.8: Theoretical (Fluid sphere model: $c = 1535 \text{ m/s}$, diameter and density are given in the figure title) and experimental backscatter frequency responses of a single OCI-AML-5 cell in PBS subject to incident pulses from a 55 MHz transducer. Each part in the figure represents a backscatter measurement from an individual different cell.

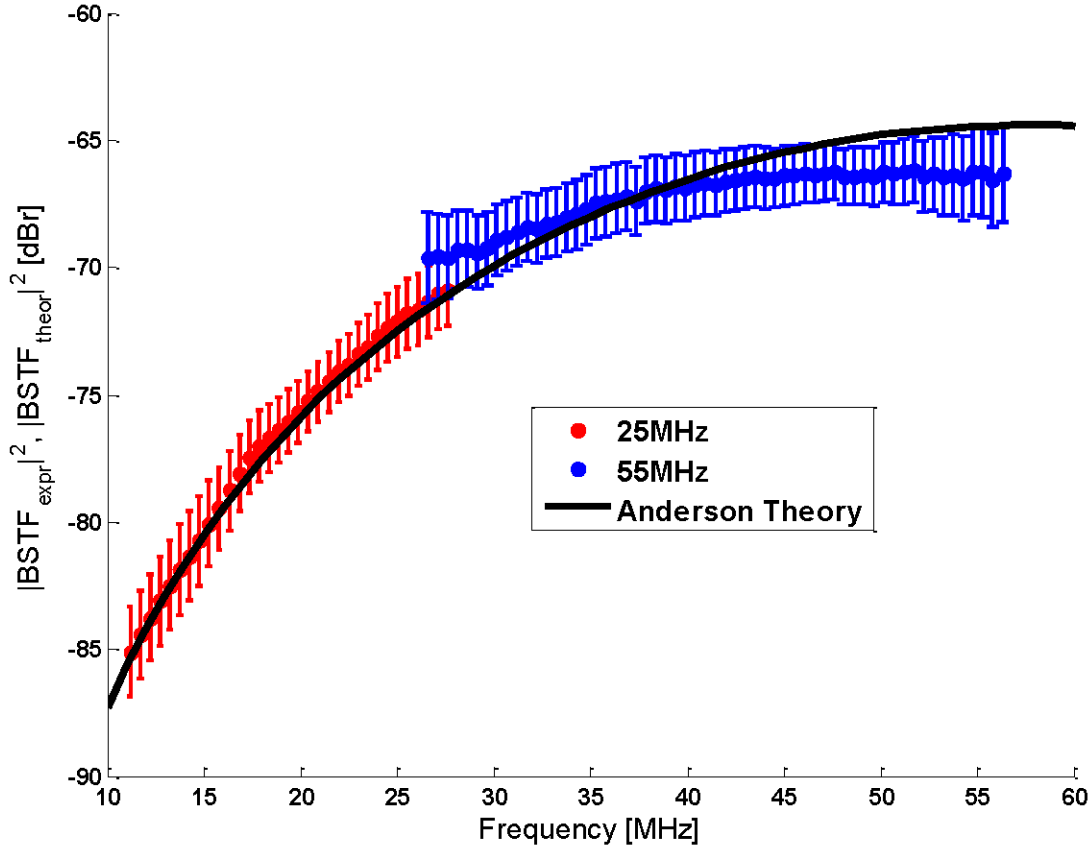


Figure 3.9: Theoretical (Fluid sphere model parameters: $d = 11.2 \mu\text{m}$, $\rho = 1.08 \text{ g/mL}$, $c = 1535 \text{ m/s}$) and average experimental backscatter frequency responses from individual OCI-AML-5 cells in PBS subject to incident pulses from two transducers: 25 and 55 MHz. Error bars represent the 95% confidence intervals. The experimental data shown correspond to the average of all data presented in Figure 3.7 and Figure 3.8.

The absence of the ringing patterns in the backscatter echoes from individual OCI-AML-5 cells imaged at 25 and 55 MHz (Figure 3.6) is an indication of their fluidlike behaviour at high frequencies. The nonexistence of sharp and abrupt peaks in the experimental frequency responses presented in Figure 3.7 and Figure 3.8 further confirms this. This is contrary to the findings reported by Baddour *et al.* (2007) where a sharp dip between 10 and 15 MHz was present in the measured frequency responses from individual OCI-AML-5 cells. This is possibly due to the presence of foreign objects in the suspension,

as no concurrent microscopy of the scattering objects was available, which may have led to the erroneous interpretation of the measured backscattered pulses. These findings presented in this work lead to the conclusion that individual OCI-AML-5 cells may be modeled as fluid sphere, similarly to PC-3 prostate carcinoma cells (Baddour *et al.*, 2007) and sea urchin oocytes (Falou *et al.*, 2008) when these cells are suspended in solution. To further investigate this, each measured backscatter frequency response was compared to the theoretical response for a fluid sphere using the Anderson model. With the exception of figures 3.8(b), 3.8(f), and 3.8(g), the measured and theoretical backscatter responses follow the same trend and are of the same order of magnitude as shown in figures 3.7(a)–3.7(h), and 3.8(a)–3.8(h). Fluid spheres with densities ranging from 1.05 g/mL to 1.11 g/mL provided the best fit to experiment data. This is further confirmed by the fact that OCI-AML-5 cells tend to slowly settle at the bottom of the suspending medium (PBS), which implies that they have a greater density than that of PBS (1.0 g/mL).

The discrepancies in the frequency dependent backscatter, but not overall level of backscatter, found between the measured and theoretical responses in figures 3.8(b), 3.8(f), and 3.8(g) may be due to a slight deformation the shape of the cell (difficult to observe optically) during the application of the pressure gradient along their membranes (holding process), which may have led to changes in their scattering behaviour, particularly at 55 MHz, where the wavelength of the central frequency of the incident pulse approaches the size of the OCI-AML-5 cell. In addition, while every effort was made to avoid any damage to the cell by carefully employing fire-polished micropipettes, the delicate nature of the OCI-AML-5 cell membrane might have damaged the cell.

The theoretical and average experimental backscatter frequency responses presented in Figure 3.9 provide a summary of the data presented in Figure 3.7 and Figure 3.8 and further evidence that scattering from OCI-AML-5 cells is best modeled with a fluid sphere scattering model. The theoretical backscatter predicted by the Anderson theory well agrees with experimental data within experimental error. Moreover, attempt to fit the Faran model using a Poisson's of 0.42 (Knight *et al.*, 2002) to the AML experimental data was not successful, which indicates that the Anderson model is more appropriate. It should be pointed out that cells in tissues, rather than surrounded by PBS solution, would exhibit potentially different scattering characteristics since in this configuration it is likely that the nucleus would contribute the most to the overall scattering: the main difference is acoustical properties will be between the cytoplasm and nucleus, rather than the cell and the solution, as in these experiments (with the cytoplasm becoming the acoustic background that the PBS is in the suspension experiments). In this case, I hypothesize that the fluid sphere model may not be an appropriate model and the scattering from the cell and nucleus may be better modeled with either more complex formulations, or models in which the elasticity of the nucleus is taken into account (Doyle *et al.*, 2009). Computer simulations may be used to calculate the ultrasound backscatter from tissues by using ultrasound scattering from collections of cells, in which each individual particles are assumed to have the same physical properties of that of the cell nucleus or that of the cell. This will allow for the better understanding of scattering from collections of cells such as in tumour tissues.

The novel technique introduced in this work provided a means for measuring the ultrasonic backscatter response from individual micron-sized objects under optical guidance to observe the scattering object. The robustness of this technique also lies in its ability to

measure the backscatter from individual cells at specific stages of apoptosis. This is particularly important for the development of theoretical models of ultrasound scattering from cell ensembles undergoing apoptosis and for the determination of the apoptotic index. Such work will help in the development of non-invasive and rapid assessment of the effectiveness of cancer therapies (Vlad *et al.*, 2008; Vlad *et al.*, 2009). This technique may also be employed in various biomedical ultrasound applications ranging from tissue characterization to molecular imaging. For instance, it can be used to study the difference between the backscatter response from individual ultrasound contrast agents in a suspending medium and individual contrast agents when they are attached to a cell.

Not all captured movies were considered appropriate for the analysis due to the following reasons: first, during the attachment of the scatterer to the micropipette, some of the suspending medium diffused into the micropipette as a result of the negative pressure applied and resulted in the failure of the release of the scatterer due to the clogging of the micropipette. Second, for delicate scatterers such as cells, a portion of the scatterer was aspirated into the micropipette and resulted in damage to the cellular structure. Third, in some trials, the speed at which the scatterer left the micropipette was too high: this resulted in ultrasound frames not containing any scattering events from the object of interest. Last, since the direction which the scatterer follows upon its release from the micropipette is not controlled, ultrasonic echoes such as the one shown in Figure 3.3(f) might be captured when the scatterer and the micropipette are at a very close distance, which makes it very difficult to extract the scatterer pulse from its corresponding RF line due to the overlapping of both scatterer and micropipette signals. 30 trials were performed on average in order to obtain eight successful measurements for each transducer. It should be noted that the estimated

range of cell velocities was found to be: 1.8×10^{-4} – 11.1×10^{-4} m/s which is much smaller than the speed of sound in PBS (1483 m/s). This would lead to a negligible Doppler shift in the frequencies for the short pulses used in the experiments.

The experimental conditions may be improved by optimizing the micropipette design (e.g. taper length, tip diameter) and the applied pressure gradient in order to prevent the aspiration of the soft scatterers into the micropipette, decrease the speed at which the scatterer gets released, and prevent physical damage to the cell.

3.4 Concluding remarks

In conclusion, the developed technique was shown to be successful in measuring the ultrasonic backscatter responses from individual micron-size objects (polystyrene microspheres) at high frequencies. The application of this technique for measuring the backscatter responses from single OCI-AML-5 cells suspended in PBS revealed that their backscatter responses at high frequencies are best modeled using the Anderson fluid sphere model.

Chapter 4

Finite element modelling of high frequency ultrasound scattering from microspheres and ultrasound contrast agents³

4.1 Introduction

Few studies have looked at the dynamic response and backscatter of UCAs at HFUS (Deng *et al.*, 1998; Moran *et al.*, 2002; Goertz *et al.*, 2005; Ketterling *et al.*, 2007). While some authors reported backscatter from UCAs centered at transducer central frequency with no harmonic components (Deng *et al.*, 1998; Moran *et al.*, 2002), others observed the presence of harmonics in the backscatter of a lipid-shelled UCA, DefinityTM (Bristol-Myers Squibb, North Billerica, MA), at low pressure (0.49 MPa) (Goertz *et al.*, 2005). The results reported by Goertz *et al.* (2005) are surprising since high pressure is required to produce a non-linear response from UCA and generate harmonics in the backscatter (refer to section 1.5 for details). Ketterling *et al.* (2007) reported the presence of subharmonics in the response of a

³ A portion of this work presented in this chapter has been presented as: Falou, O., Kumaradas, J. C., and Kolios, M. C. (2007) "Finite-element Modeling of Elastic Surface Modes and Scattering from Elastic Objects," COMSOL Users Conference, Boston, USA and Falou, O., Jafari Sojahrood, A., Kumaradas, J. C., and Kolios, M. C. (2010) "Modeling the effect of shell thickness on high frequency ultrasound scattering from ultrasound contrast agents," Canadian Acoustical Association Conference, Victoria, Canada.

polymer-shelled UCA, Point (POINT Biomedical, San Carlos, CA), at high pressure (5.9 MPa). However, the experimental subharmonic response occurs at lower pressure amplitude than the theoretical response predicted by the Church model (Church, 1995). Refer to Appendix A for a detailed description of the Church model.

Analytical solutions to the problem of wave scattering from spherical objects such as ultrasound contrast agents have been studied extensively in the past (De Jong *et al.*, 1993; Church, 1995; Allen *et al.*, 2001; Chen *et al.*, 2003; Doinikov *et al.*, 2007). A theoretical work on small amplitude UCA oscillations by Allen *et al.* (2001) showed that albumin-shelled contrast agents excited by HFUS (1 – 40 MHz) support dipole resonance in addition to the monopole resonance predicted by other models (De Jong *et al.*, 1993; Church, 1995; Doinikov *et al.*, 2007). Chen *et al.* (2009) studied the harmonic contributions to the backscatter from the Definity UCA and found that such contribution is significant for single UCAs but may be less important for polydispersed Definity population using HFUS. However none of these models can account for inhomogeneity in the UCA shell, shell stresses and strains, non-linear behaviour of UCAs at high pressures, and UCA-cell interactions.

Finite-element analysis combined with other numerical techniques, such as the boundary element method, infinite elements, and T-matrix method have been used in the past to model acoustic scattering from various objects submerged in a fluid (Hunt *et al.*, 1975; Wilton, 1978; Numrich *et al.*, 1981; Everstine *et al.*, 1990; Eaton *et al.*, 1996). The near-field scattering was typically modeled using finite elements while other techniques were used to

find the far-field scattering. Most of these studies concentrated on scattering from rigid objects (Hunt *et al.*, 1975; Demkowicz *et al.*, 2006).

Recently, Puzin *et al.* (2007) developed a 3-D finite element model to study the changes in the monopole resonance frequency of various thick-shelled UCAs (in which the shell thickness is 10% the UCA radius). Their model was based on the near-field calculations of the pressure field which showed a good agreement with analytical solutions (De Jong *et al.*, 1993; Church, 1995; Doinikov *et al.*, 2007). Patil *et al.* (2010) proposed a 3-D finite element model which accounts for the non-linear sound propagation in the UCA surrounding medium. Their model was validated against experiment observations of non-adherent and adherent UCAs reported by other authors (Zhao *et al.*, 2005; Zhao *et al.*, 2006; Garbin *et al.*, 2007; Vos *et al.*, 2007). In this work, I introduce a 2-D axi-symmetric finite element model to study the far-field ultrasonic backscatter response from ultrasound contrast agents at high frequencies. The model describes the basic fundamentals of sound wave propagation using the Helmholtz equation in addition to the stress-strain relationship within elastic material and is capable of predicting the dynamic response of ultrasound contrast agents, particularly surface modes. It requires less computational resources than 3-D models, particularly at high frequencies where more elements are required as a result of the short ultrasonic wavelengths contained in the incident pulse. I hypothesize that the finite-element model may be used to predict high frequency ultrasound scattering from ultrasound contrast agents for the purpose of monitoring cancer treatment.

4.2 Methods

The COMSOL Multiphysics™ 3.5a (COMSOL, Inc., Burlington, MA) finite-element package was used to simulate the acoustic wave propagation through spherical structures. A spherical geometry, such as that of polystyrene microspheres, was chosen for the first stage of the model development since analytical solutions exist which enable the comparison of computational and analytical results and hence allows for the validation of the developed finite element model.

The scatterer is located in the centre of the computational domain with different acoustic properties than those of the surrounding fluid. The scatterer is insonified by a plane wave travelling in the $+z$ direction. Due to the symmetric nature of the problem, the 3-D model can be simplified by a 2-D axi-symmetric model, with the z -axis being the axis of the symmetry. 2-D models require less computational resources and execution times and they are easier to mesh when compared to 3-D models.

4.2.1 Polystyrene Microsphere

An example of a scatterer that supports both longitudinal and shear waves are polystyrene microspheres used for the calibration of cell counters. Baddour *et al.* (2005) and Falou *et al.* (2010) have shown good agreement between analytical solutions and experimental backscatter measurements of polystyrene microspheres suspended in water. The time-harmonic Helmholtz wave equation was used to model propagation of sound waves in the domain outside the scatterer (assumed to be a Newtonian fluid):

$$\nabla \left(\frac{1}{\rho} \nabla p \right) + \frac{\omega^2 p}{\rho c^2} = 0, \quad (4.1)$$

where p is the acoustic pressure, ρ is the mass density of the medium, ω is the angular frequency ($\omega = 2\pi f$) of the wave, and c is the speed of the wave in the medium. The surrounding medium was assumed to be water having a density and speed of sound of 1000 kg/m^3 and 1483 m/s , respectively. The stress-strain relationship or constitutive equation for linear elastic material was used to describe the stress-strain relationship in the microsphere. The stress σ and the strain ε are related by the Hooke's Law for three-dimensional isotropic material (Acoustics Module: User's Guide, 2008):

$$\sigma = [D]\varepsilon, \quad (4.2)$$

where $[D]$ is given by:

$$[D] = \frac{E}{(1+\nu)(1-2\nu)} \begin{bmatrix} 1-\nu & \nu & \nu & 0 & 0 & 0 \\ \nu & 1-\nu & \nu & 0 & 0 & 0 \\ \nu & \nu & 1-\nu & 0 & 0 & 0 \\ 0 & 0 & 0 & \frac{1-2\nu}{2} & 0 & 0 \\ 0 & 0 & 0 & 0 & \frac{1-2\nu}{2} & 0 \\ 0 & 0 & 0 & 0 & 0 & \frac{1-2\nu}{2} \end{bmatrix}, \quad (4.3)$$

$$\sigma = \begin{pmatrix} \sigma_x \\ \sigma_y \\ \sigma_z \\ \tau_{xy} \\ \tau_{yx} \\ \tau_{zx} \end{pmatrix}, \quad (4.4)$$

and

$$\boldsymbol{\varepsilon} = \begin{pmatrix} \varepsilon_x \\ \varepsilon_y \\ \varepsilon_z \\ \gamma_{xy} \\ \gamma_{yx} \\ \gamma_{zx} \end{pmatrix}. \quad (4.5)$$

E is the Young's modulus, ν is the Poisson's ratio, and $\sigma_x, \sigma_y, \sigma_z$ are stresses along the x, y and z directions, respectively (also known as normal stresses). $\tau_{xy}, \tau_{yx}, \tau_{zx}$ are called shear stresses. The notation τ_{ij} is used to represent shear stresses where i denotes the direction of the stress component, while j denotes the surface on which the stress component acts. $\varepsilon_x, \varepsilon_y, \varepsilon_z$ and $\gamma_{xy}, \gamma_{yx}, \gamma_{zx}$ are the normal and shear strains, respectively.

Two boundary conditions were imposed, one for the outer domain boundary and one for the boundary between the scatterer and the surrounding medium (Figure 4.1). A second-order non-reflecting boundary condition (NRBC) proposed by Bayliss-Gunzburger-Turkel (Bayliss *et al.*, 1982) was applied on the outer boundary. This boundary condition approximates an infinite space so that the scattered wave is not reflected back into the domain. The Bayliss-Gunzburger-Turkel condition is given by:

$$\frac{\partial^2 p}{\partial r^2} + \left(\frac{4}{R_0} - 2ik \right) \frac{\partial p}{\partial r} + \left(\frac{2}{R_0} - 4ik \right) \frac{p}{R_0} - k^2 p = P_0 e^{-ikz} \quad (4.6)$$

where k is the wavenumber ($k = \omega/c$) and R_0 is the radius of the boundary (which was three times that of the scatterer radius in this work). The term on the right-hand side represents the

emitted plane wave from the transducer, P_0 (assumed to be 1 Pa) whose direction is along the +z-axis.

In the case of an elastic material immersed in a fluid, shear and surface waves may also exist inside and at the surface of the scatterer. The acoustic wave incident on the surface of the scatterer exerts a load on the surface of the elastic sphere described by:

$$\mathbf{F} = -\mathbf{n}p, \quad (4.7)$$

where \mathbf{F} is the face load, \mathbf{n} is the outward pointing normal vector to the surface, and p the wave pressure on the surface (Acoustics Module: User's Guide, 2008). The normal component of acceleration was coupled at the surface of the scatterer in the solid (right hand side) and fluid (left hand side) domains:

$$\mathbf{n} \cdot \left(\frac{1}{\rho} \nabla p \right) = -(\mathbf{n} \cdot \mathbf{u}) \omega^2, \quad (4.8)$$

where \mathbf{u} is the time-harmonic displacement vector. COMSOL's implementation of the above equations is based on the principle of virtual works, which states that for any displacement, the total work from internal strains is the negative of the work from external loads, so that their sum equals to zero (Acoustics Module: User's Guide, 2008).

The quadratic Lagrange triangular elements (Zienkiewicz *et al.*, 2005) were used in the discretization of the computational domain. The Unsymmetric-pattern MultiFrontal PACKage or UMFPACK solver (Davis, 2004) was used to obtain a solution since it is fast (non-iterative). The finite-element models were executed on a computer having an Intel® Xeon™ 2.80 GHz Processor with 1.00 GB of RAM running Microsoft® Windows XP®

operating system. The computation time was found to be 10 seconds per frequency on average.

The finite element solution was compared to the analytical solution of scattering from an elastic sphere initially derived by Faran (1951) and corrected by Hickling (1962). The scattered pressure from an elastic sphere insonified by a plane wave travelling in the $+z$ direction is given by:

$$p_s(r, \theta) = -P_0 \sum_{m=0}^{\infty} \left[(-i)^{m+1} (2m+1) \sin \eta_m e^{i\eta_m} \right] \left[j_m(kr) - in_m(kr) \right] P_m(\cos \theta), \quad (4.9)$$

where η_m is the phase-shift which takes into account the physical properties of the surrounding medium and the elastic sphere such as the sphere's mechanical properties (see Appendix A for details). A 30 μm diameter microsphere was used for this study since it exhibits distinguishable resonant features at frequencies of interest (10–70 MHz). Oscillations representing surface modes of the microsphere at various resonance frequencies were also visualized by plotting the displacement at the microsphere surface.

4.2.2 Ultrasound Contrast Agent

Ultrasound contrast agents are composed of an elastic shell encapsulating a gas core. The finite element model (Figure 4.1) described above had to be modified in such a way so that:

- The time-harmonic Helmholtz wave equation is used to model propagation of sound waves in the gas core as well as the domain outside the scatterer.

- At the gas core-shell and shell-surrounding medium interfaces, both equations 4.7 and 4.8 are imposed as boundary conditions to account for the presence of shear and surface waves inside and at the surface of the UCA shell.

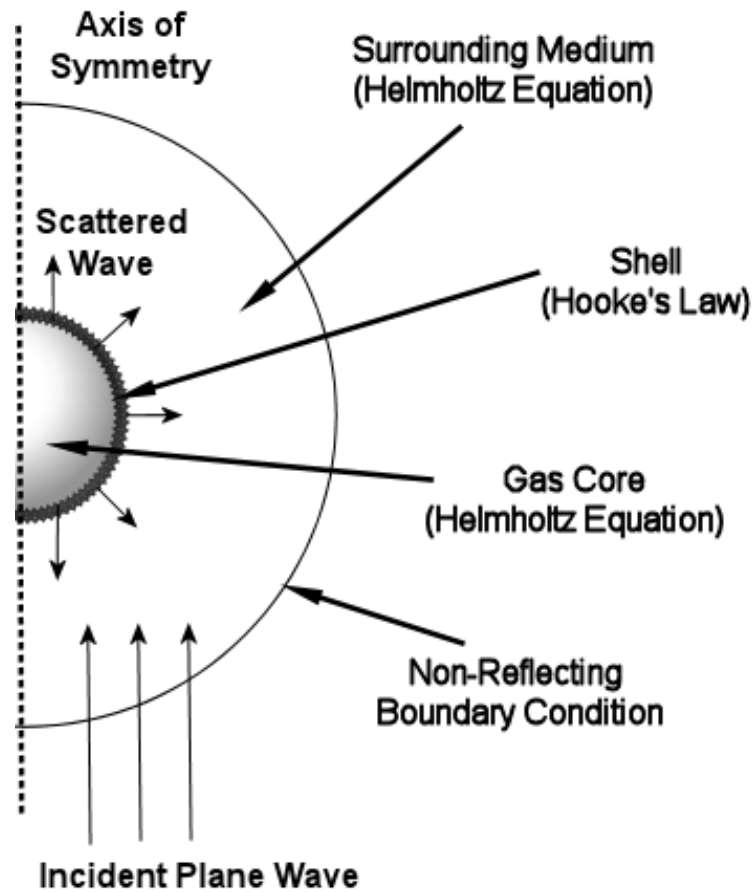


Figure 4.1: Setup of the finite-element model for UCA immersed in a fluid.

The number of mesh elements was chosen by studying the effect of refining the mesh on the backscatter pressure amplitude. It was found that 14,736 elements are needed to obtain accurate solutions as shown in Figure 4.2. Figure 4.3 illustrates the corresponding meshed model.

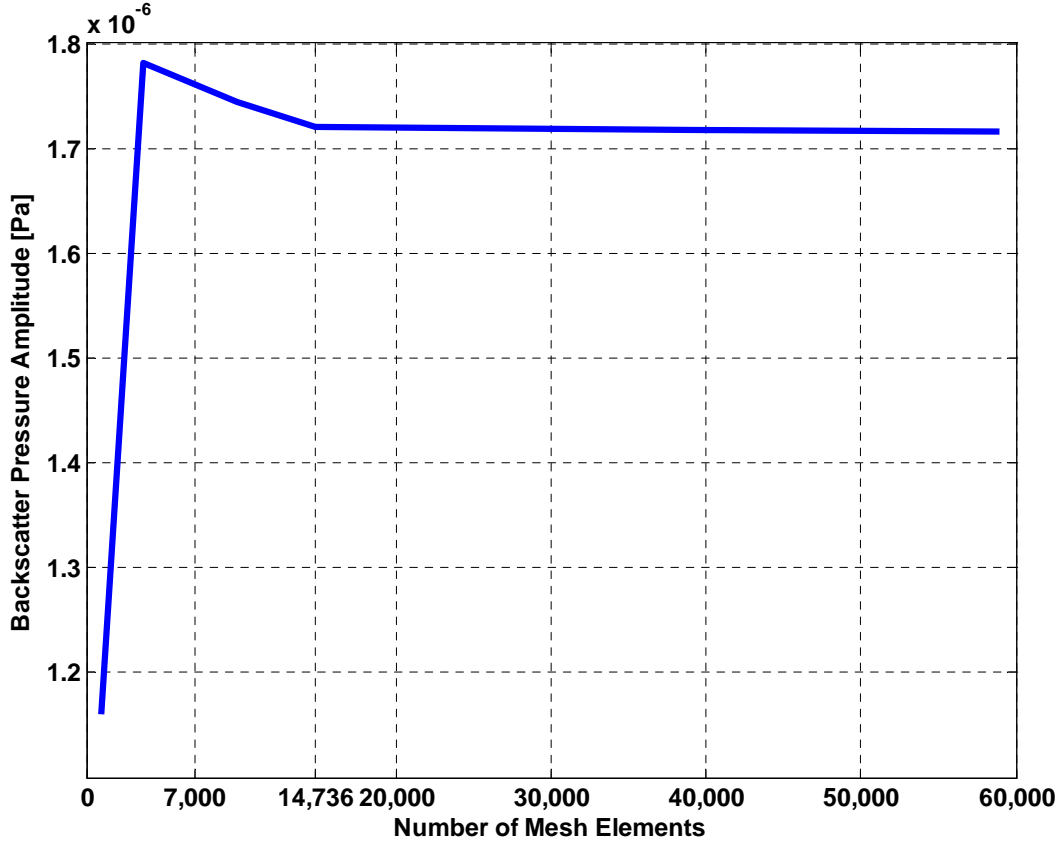


Figure 4.2: Backscatter pressure amplitude [Pa] vs. number of mesh elements.

The finite element solution for the fundamental resonance frequency was compared to the analytical solution formulated by Church (1995). In his work, the UCA is modelled as a continuous layer of viscoelastic solid material (shell) that separates the gas core from the surrounding liquid and whose angular linear resonance frequency is given by:

$$\omega_0 = \sqrt{(\rho_s R_{01}^2 \beta)^{-1} \left\{ 3\kappa P_h - \frac{2s_1}{R_{01}} - \frac{2s_2 R_{01}^3}{R_{02}^4} + 4 \frac{V_s G_s}{R_{02}^3} \left[1 + S \left(1 + \frac{3R_{01}^3}{R_{02}^3} \right) \right] \right\}}, \quad (4.10)$$

where S is a term accounting for the strain, V_s is the volume, G_s is the shear modulus, ρ_s is the mass density, R_{01} is the inner radius, R_{02} is the outer radius, s_1 is the inner surface

tension, and s_2 is the outer surface tension of the shell, respectively. P_h is the hystrostatic pressure (10^5 Pa), κ is the polytropic exponent (1.4 in the adiabatic case), and β is a term accounting for the difference in mass densities between the shell and the surrounding fluid (see Appendix A for details).

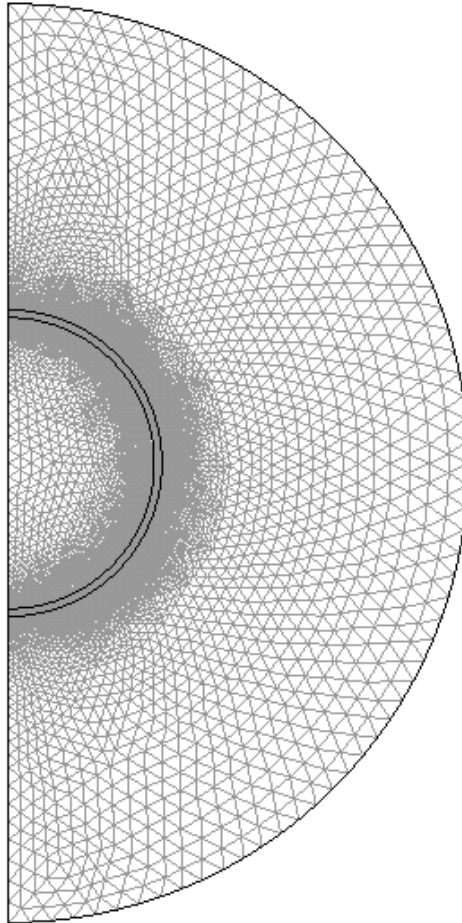


Figure 4.3: Meshed model: 14,736 triangular elements.

A $4 \mu\text{m}$ diameter perfluorocarbon phospholipid-coated contrast agent known as BR14 (Bracco Research SA, Geneva, Switzerland) surrounded by water was used to validate the finite element model by comparing the resonance frequency predicted by both the finite

element model and the Church solution. This contrast agent was chosen it since it is widely used and has been the subject of research by many investigators (Goertz *et al.*, 2003; Versluis *et al.*, 2004; Emmer *et al.*, 2007; Dollet *et al.*, 2008). Table 4.1 gives the physical properties of BR14 used in the Church and finite element models. The surface tensions at both the shell-gas and the shell-liquid interfaces were assumed to be negligible (Emmer *et al.*, 2007).

A parametric study was also performed using the finite element model to study the effects of changing the UCA parameters on its scattering behaviour at high frequencies (10–70 MHz). The far-field scattered pressure from the UCA insonified by a plane wave travelling in the $+z$ direction was investigated by varying its diameter, shell thickness, and shell elasticity while keeping other parameters fixed. It is believed that the finite element model, which describes the basic fundamentals of sound wave propagation and stress-strain relationship within elastic material, may help in the understanding of the behaviour of UCAs at high frequencies. It may also provide an insight into the presence of harmonic components in the UCA response observed experimentally at low pressures (Goertz *et al.*, 2005).

Table 4.1: Physical properties of the BR14 ultrasound contrast agent (Emmer *et al.*, 2007; Dollet *et al.*, 2008)

Property	Value
Shell thickness (δR_s)	3 nm
Shell density (ρ_s)	1100 kg/m ³
Shell's Young's modulus (E_s)	177.6 MPa
Shell's shear modulus (G_s)	60 MPa
Shell's Poisson's ratio (ν_s)	0.48
Perfluorocarbon density (ρ_g)	11.21 kg/m ³
Perfluorocarbon speed of sound (c_g)	100 m/s

4.3 Results

4.3.1 Polystyrene microsphere

Figure 4.4 shows the comparison between the analytical (Faran) and finite-element solutions for scattering from a 30 μm polystyrene microsphere immersed in water at high frequencies. The plot shows the far-field backscatter response versus frequency. Figure 4.5 depicts the deformations of the microsphere immersed in water at five resonance frequencies which corresponded to surface modes. Figure 4.6 shows the angular distribution of scattering for the same microsphere at the first five resonance frequencies.

4.3.2 BR14 Ultrasound Contrast Agent

In order to validate the finite element model results for ultrasound contrast agents, the resonance frequencies of the BR14 contrast agents having diameters ranging from 1 to 10 μm were compared against the Church model predictions. Figure 4.7 illustrates these comparisons. The maximum percentage error between the Church and the finite element solutions was found to be $\sim 5\%$. The finite element model was then used to examine how changes in the physical properties of the contrast agents would alter the scattering behaviour of these agents as a function of frequency. Figure 4.8 shows the effects of varying the shell thickness from 3 to 100 nm on the backscatter response for BR14 while keeping other parameters fixed.

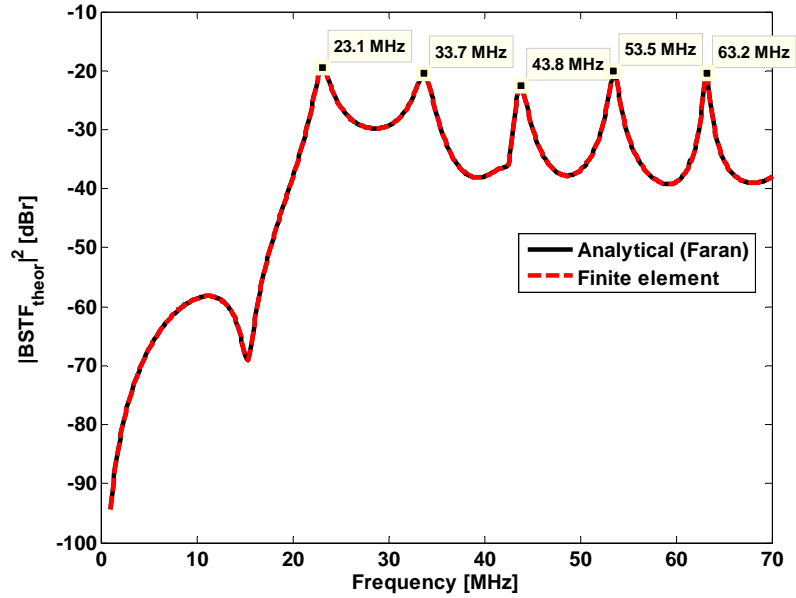


Figure 4.4: Analytical (Faran) and finite-element solutions for scattering from a $30\ \mu\text{m}$ polystyrene microsphere immersed in water at high frequencies.

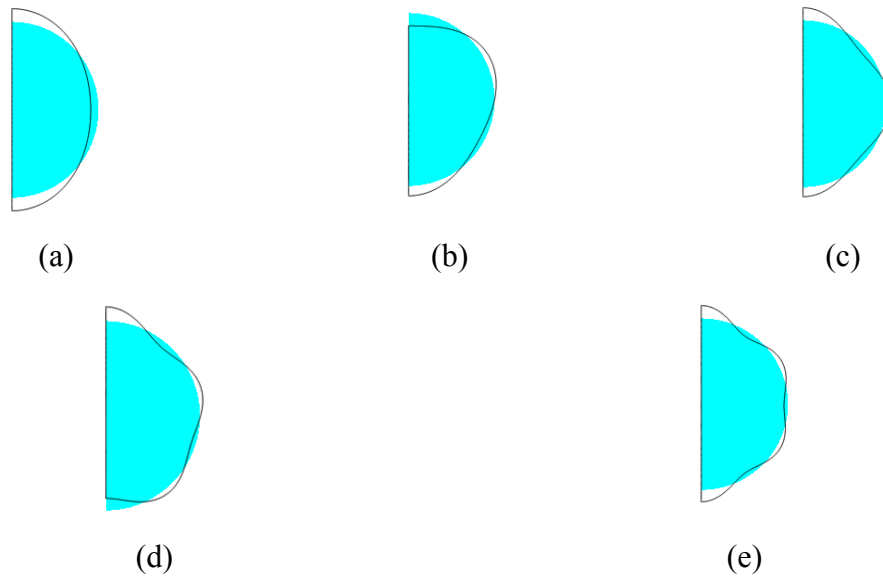
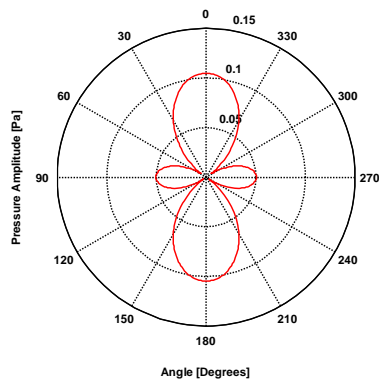
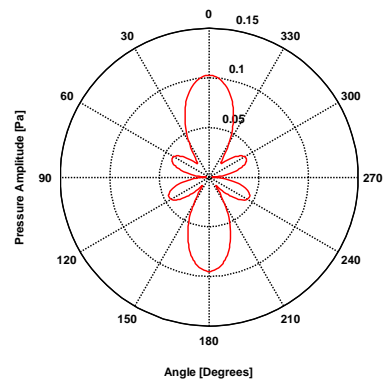


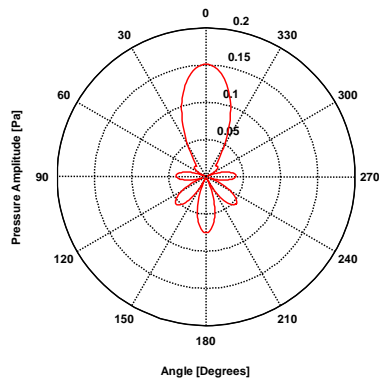
Figure 4.5: Finite-element solutions for deformations of a $30\ \mu\text{m}$ polystyrene microsphere at a) 23.1, b) 33.7, c) 43.8, d) 53.5, and e) 63.2 MHz. The plots show a snapshot of the maximum deformation for a slice parallel to the direction of wave propagation (bottom to top). The cyan half circle and the black curve illustrate the shape of the microsphere before and after applying the pressure, respectively. The displacement was multiplied by a factor of 4.5×10^7 to 1.6×10^8 for visualization purposes.



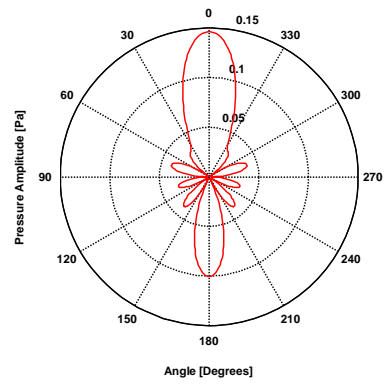
(a)



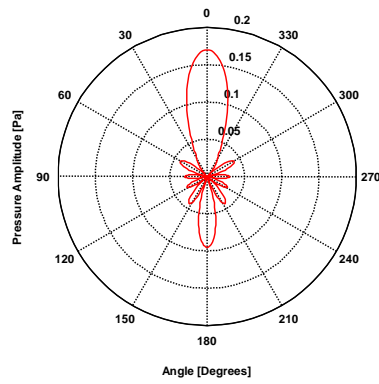
(b)



(c)



(d)



(e)

Figure 4.6: Analytical solutions for angular scattering from a $30\ \mu\text{m}$ polystyrene microsphere at a) 23.1, b) 33.7, c) 43.8, d) 53.5, and e) 63.2 MHz. The plots show the pressure amplitude [Pa] vs. angle [degrees]. Backscattering occurs at 180° .

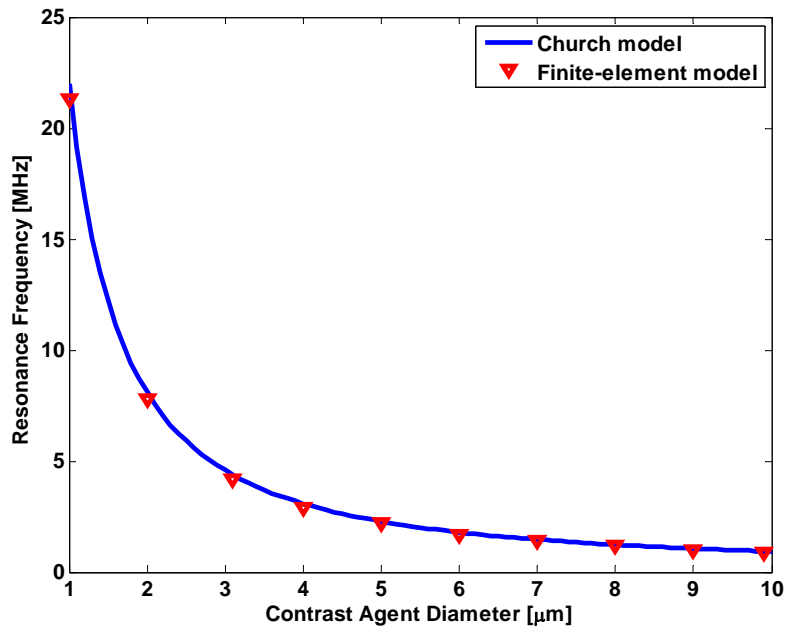


Figure 4.7: Resonance frequency vs. contrast agent diameter: comparison between the Church and finite element solutions.

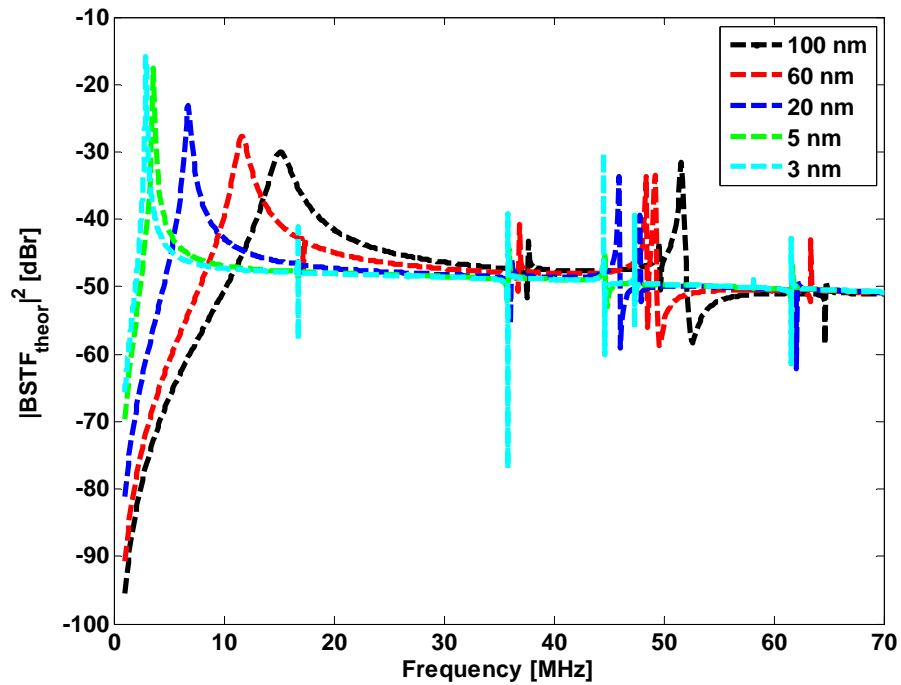


Figure 4.8: Effects of varying the shell thickness on the backscatter response for 4 μm diameter BR14.

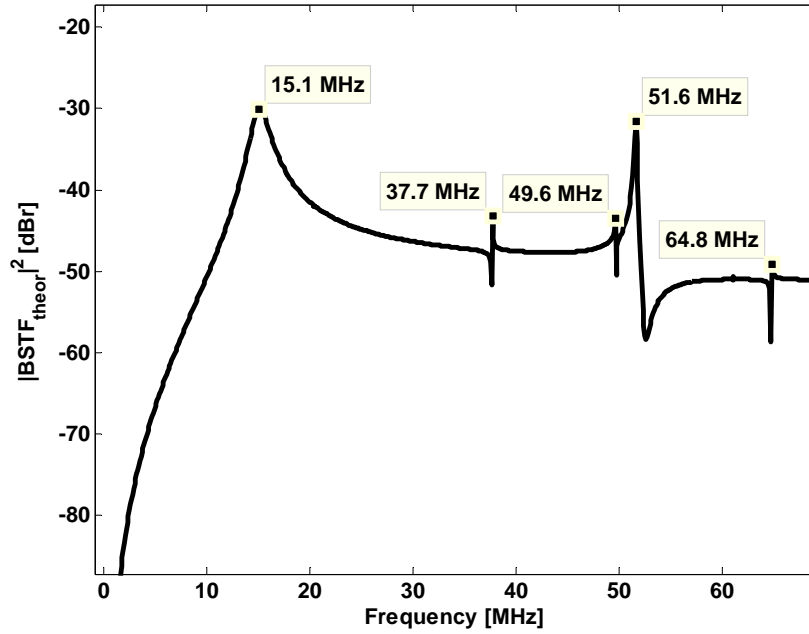


Figure 4.9: Backscatter vs. frequency for a 100 nm shelled, 4 μm diameter UCA immersed in water.

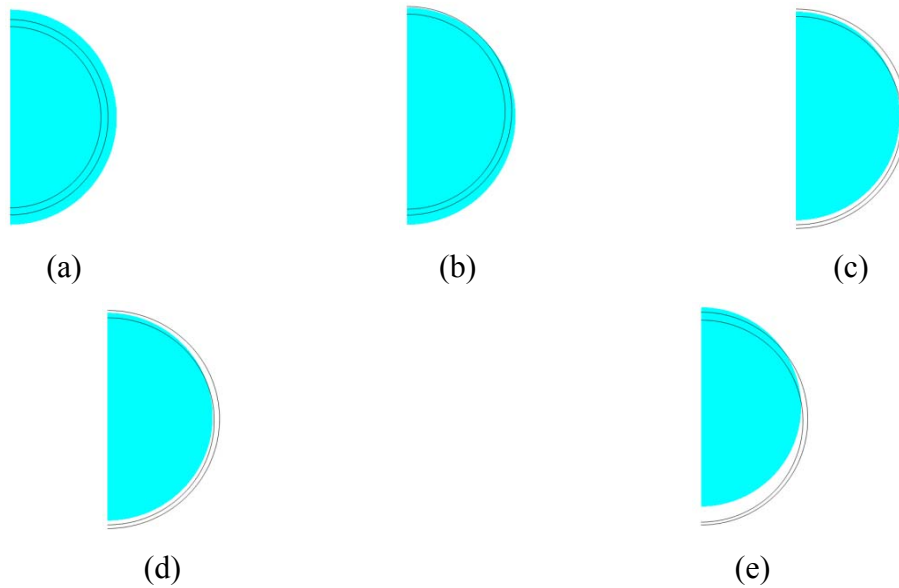
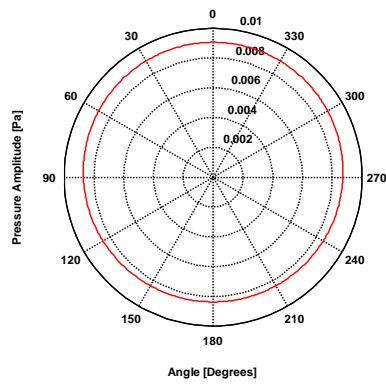
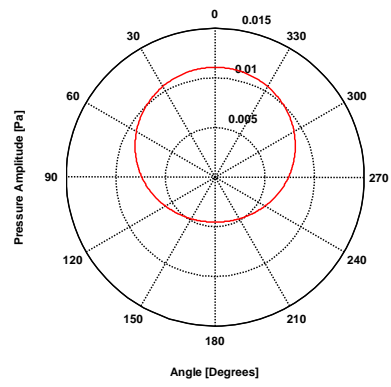


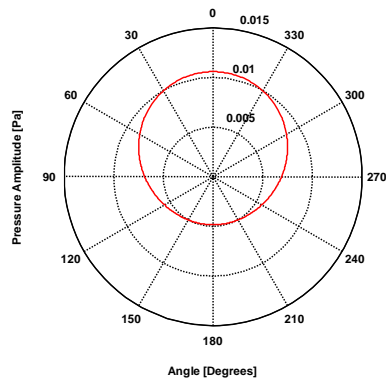
Figure 4.10: Finite-element solutions for deformations of a 100 nm shelled, 4 μm diameter UCA at a) 15.1, b) 37.7, c) 49.6, d) 51.6, and e) 64.8 MHz. The plots show a snapshot of the maximum deformation for a slice parallel to the direction of wave propagation (bottom to top). The cyan half circle and the black curve illustrate the shape of the microsphere before and after applying the pressure, respectively. The displacement was multiplied by a factor of 3.5×10^5 to 1.5×10^7 for visualization purposes.



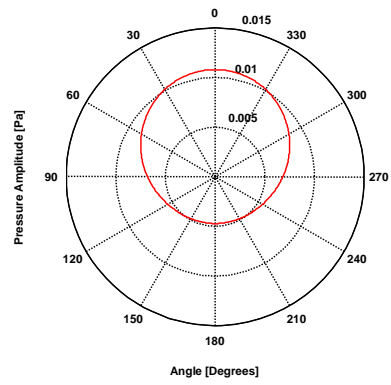
(a)



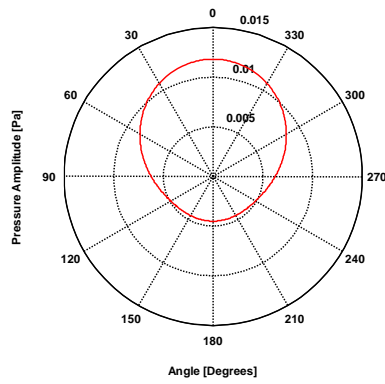
(b)



(c)



(d)



(e)

Figure 4.11: Finite element solutions for angular scattering from a 100 nm shelled, 4 μm diameter UCA at a) 15.1, b) 37.7, c) 49.6, d) 51.6, and e) 64.8 MHz. The plots show the pressure amplitude [Pa] vs. angle [degrees]. Backscattering occurs at 180° .

The far-field backscatter versus frequency for a 100 nm shelled UCA immersed in water at high frequencies is given in Figure 4.9. Figure 4.10 depicts the deformations of a 100 nm shell UCA at five resonance frequencies. The angular distribution of scattered sound as a function of angle for same UCA at five resonance frequencies is shown in Figure 4.11. The effects of varying the shell shear modulus from 10 to 60 MPa on the backscatter response for a 100 nm shelled, 4 μm diameter UCA are shown in Figure 4.12. Figure 4.13 shows the effects of varying the diameter from 1 to 6 μm on the backscatter response for a 100 nm shelled UCA. Figure 4.14 shows the relationship between shell thickness and monopole resonance frequency for a 4 μm UCA. Figure 4.15 shows the relationship between shell shear modulus and the resonance frequencies for a 100 nm, 4 μm UCA. The relationship between diameter and resonance frequencies for a 100 nm shelled UCA is shown in Figure 4.16.

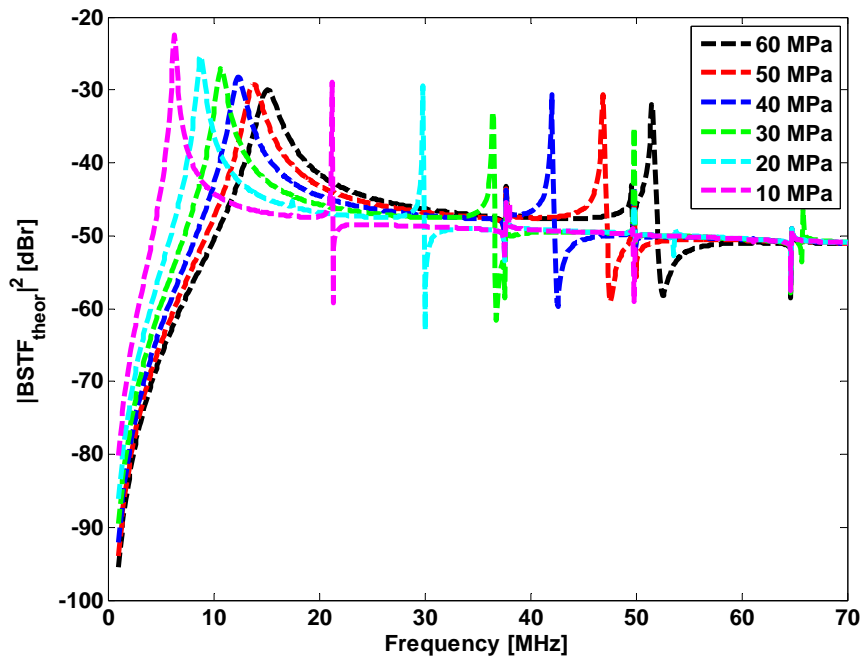


Figure 4.12: Effects of varying the shell shear modulus on the backscatter response for a 100 nm shelled, 4 μm diameter UCA.

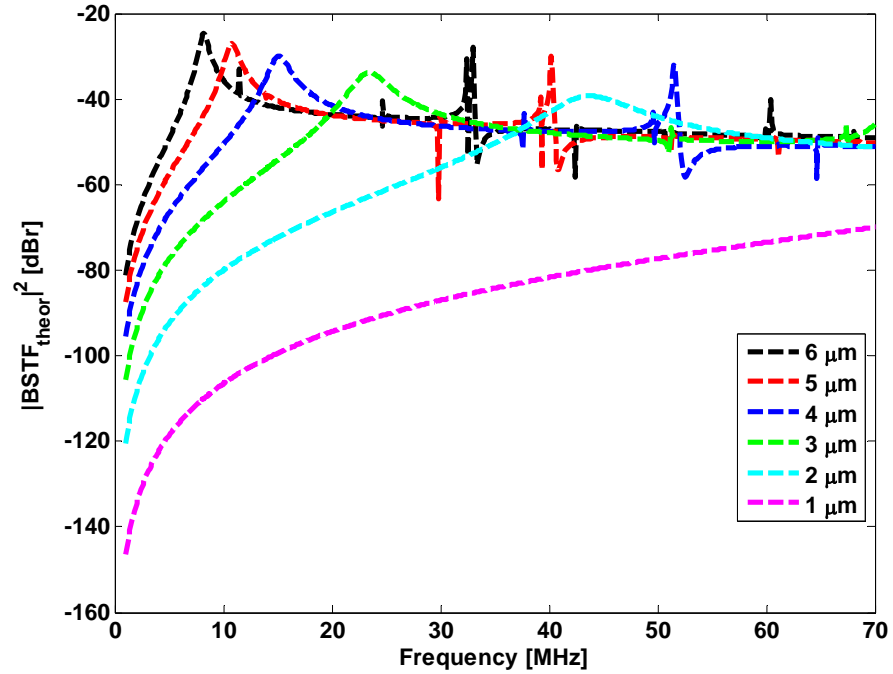


Figure 4.13: Effects of varying the contrast agent's diameter on the backscatter response for a 100 nm shelled UCA.

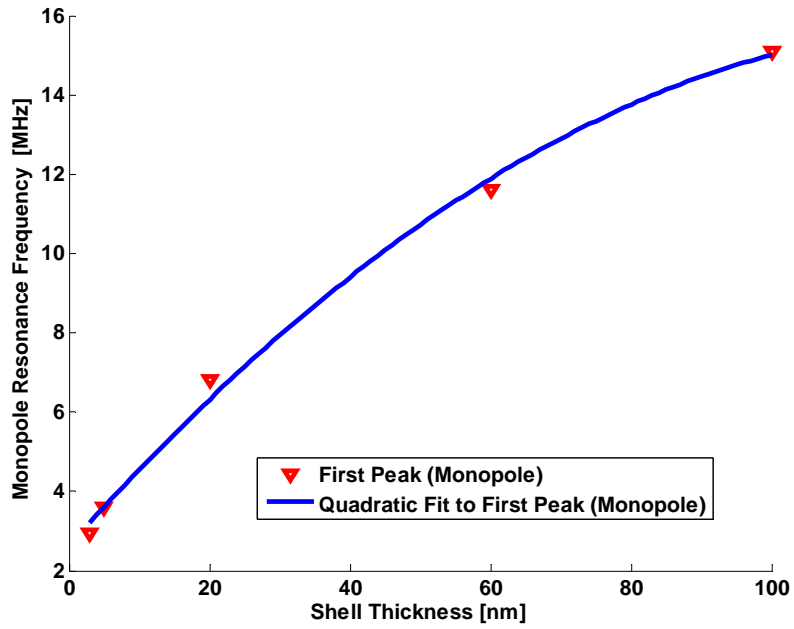


Figure 4.14: Relationship between shell thickness and monopole resonance frequency for a 4 μm UCA.

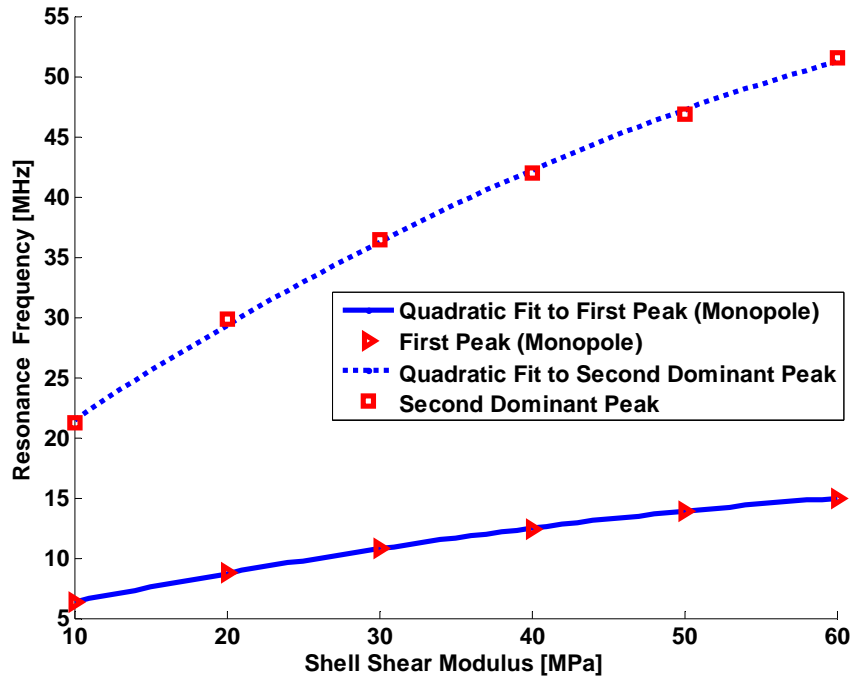


Figure 4.15: Relationship between shell shear modulus and the resonance frequencies for a 100 nm, 4 μm UCA.

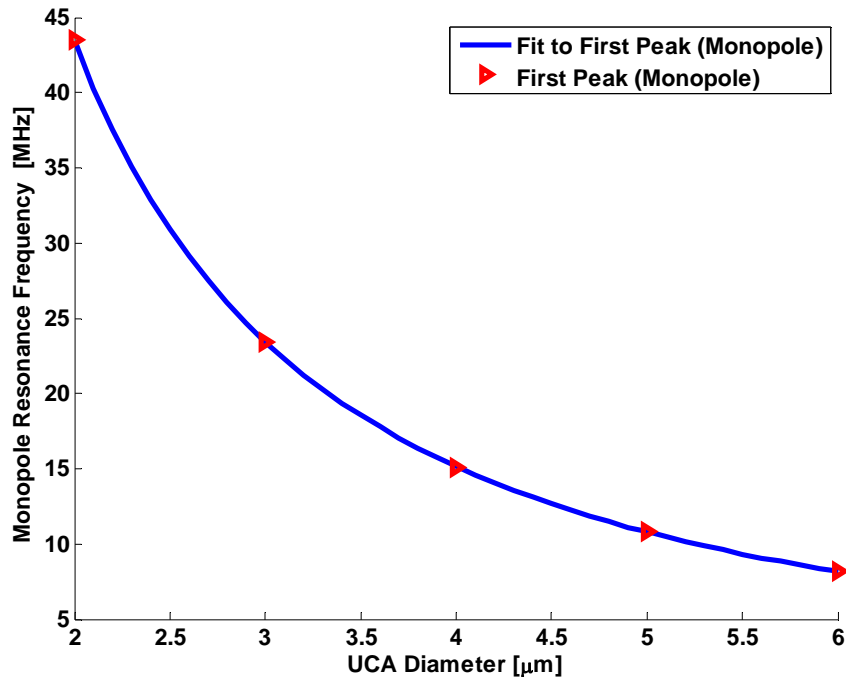


Figure 4.16: Relationship between diameter and resonance frequencies for a 100 nm shelled UCA.

4.4 Discussion and Conclusions

The dynamic behaviour and the backscatter response of ultrasound contrast agents at high frequency ultrasound are not fully understood. Various analytical models have been developed to better understand such behaviour. However, none of them can account for non-radial oscillations of the UCA, which may be significant at high frequencies. A finite element model which incorporates such oscillations was developed and validated by comparing the finite element model solution to that of Faran for a 30 μm polystyrene microsphere.

4.4.1 Polystyrene Microspheres

An excellent agreement was found between the analytical and finite element solutions, despite the large changes in pressure as a function of ultrasound frequency as shown in Figure 4.4. Various wide peaks of comparable magnitudes were found in the backscatter of the microsphere and correspond to its resonance frequencies. The first five resonances occur at 23.1, 33.7, 43.8, 53.5, and 63.2 MHz. A close look at the deformations of the polystyrene microsphere at its resonance frequencies (Figure 4.5) reveals the presence of non-spherical oscillations, or surface modes, at these frequencies which become more complex in shape as the frequency increases. At 23.1 MHz (lowest resonance frequency), the microsphere oscillates between a prolate and oblate spheroidal shape, known as quadrupole mode or mode $n = 2$ (Uberall *et al.*, 1996). The octupole mode ($n = 3$) occurs at 33.7 MHz where three wavelengths of the surface distortion are needed to span the microsphere's circumference. Four ($n = 4$), five ($n = 5$), and six ($n = 6$) wavelengths of the surface distortion are required to span the microsphere's circumference at 43.8, 53.5 and 63.2 MHz, respectively.

The angular distribution of scattering becomes more complex in shape as the frequency increases (Figure 4.6). A distinct angular directivity characterizes each resonance frequency because of multipole effects. The forward and back scattering amplitude are identical at 23.1 and 33.7 MHz ($n = 2, 3$). For frequencies above 33.7 MHz, the forward scattering becomes stronger than the backscatter. The number of scattering lobes also increases as a function of the resonance frequency which is likely related to the multipole effects. No monopole or dipole modes ($n = 0, 1$) were found at resonances in the frequency range of interest. To the best of my knowledge, this is the first investigation of the relationship between surface modes and resonance frequencies of microspheres subject to high frequency ultrasound.

4.4.2 BR14 Ultrasound Contrast Agent

A very good agreement (maximum error of $\sim 5\%$) was found between the finite element model and the Church analytical solution (Figure 4.7). The monopole resonance frequency decreases with the increase of the contrast agent diameter which agrees with previous findings (De Jong *et al.*, 1993; Church, 1995). Increasing the shell thickness of the ultrasound contrast agent produces new features in the backscatter response as shown in Figure 4.8. When the shell thickness is increased from 3 *nm* to 100 *nm*, with the other simulation parameters held constant, several changes in the backscatter occur. The monopole peak became wider, decreased in height, and increased to 15.1 MHz with the increase of shell thickness. For thick shelled contrast agents, four other peaks appear at 37.7, 49.6, 51.6, and 64.8 MHz as shown in Figure 4.9. The peak centered at 51.6 MHz is of comparable height to that of the monopole peak at 15.1 MHz. A study of the deformations of this UCA lead to

some interesting findings. First, at 15.1 MHz, the UCA contracts and expands periodically and exhibit the breathing mode or $n = 0$. At higher resonance frequencies, the UCA undergo a shape deformation characterized by a translational motion, in addition to contraction and expansion. The UCA shell thickness becomes non-uniform as the UCA oscillates: thinning of the shell occurs in the direction of the translation where as thickening occurs in the opposite direction as shown in Figure 4.10(d) and Figure 4.10(e). This change in shell thickness is particularly seen at high resonance frequencies (51.6 and 64.8 MHz).

The surface modes illustrated in Figure 4.10 seem to correlate with the angular scattering shown in Figure 4.11. For the monopole resonance at 15.1 MHz, an isotropic scattering is obtained, which is similar to that of a free air bubble (Falou *et al.*, 2006). At higher resonance frequencies (37.7, 49.6, 51.6, 64.8 MHz), the scatter amplitude is directional and is of greater magnitude in the forward direction compared to the back direction. This is likely due to the translational motion of the contrast agent observed at these frequencies. The shape oscillations of the contrast agent above the monopole resonance appear to be the result of the summation of various surface modes. The resonance peaks at 49.6, 51.6, and 64.8 MHz are identified as overtones of the resonance peak at 37.7 MHz since they all exhibit similar shape oscillations and angular distributions of scattering. It is instructive to compare the surface modes exhibited by the ultrasound contrast agent to those exhibited by the polystyrene microsphere. The former developed a breathing mode ($n = 0$) at the fundamental resonance frequency and a collection of complex oscillations at higher frequencies, in contrast to the latter which does not exhibit the breathing mode but rather higher modes starting with $n = 2$ (quadrupole mode) and ending with mode $n = 6$ for the range of frequencies studied. For the polystyrene microsphere, a systematic relationship

exists between the resonance frequency and its corresponding surface mode. The higher the resonance frequency, the more complex the oscillation pattern, and hence the higher is the mode number. No such relationship was found for the ultrasound contrast agent.

The study of surface modes of microspheres and ultrasound contrast agents in particular may have implications on imaging and therapeutic applications. Surface modes may play a role in the generation of the acoustical energy during subharmonic imaging with ultrasound contrast agents, a promising imaging technique which offers a very good contrast between tissue and blood vasculature (Goertz *et al.*, 2007). They may also provide insights into the shell properties which may lead to a better modelling of the shell behaviour at high frequencies. In terms of therapeutic applications, surface modes will help in the understanding of the mechanism of microbubble rupture and the release of drug during localized drug delivery process, as stress/strain distributions in the shell can be studied in details.

As discussed earlier, when the shell thickness is increased, the monopole peak becomes wider, decreases in height, and shifts towards higher frequencies. A quadratic relationship was found between the shell thickness and the monopole resonance frequency as shown in Figure 4.14. Increasing the shell's shear modulus from 10 MPa to 60 MPa for the 100 nm shell BR14 contrast agent, while keeping other parameters fixed, produced similar effects to those obtained as the result of the increase in the shell thickness. The monopole and the second dominant backscatter peaks in the range of frequencies studied (whose magnitude is comparable to that of the monopole), became wider and shifted to higher frequencies. For the 10 MPa shell, these peaks were initially centered at 6.3 and 21.2 MHz, and with

increasing shear modulus, they shifted to 15.1 and 51.6 MHz for the 60 MPa shell, respectively. In addition, the difference between the frequencies of the monopole and the second dominant peaks increases as the shell's shear modulus increases (6.3 and 21.2 MHz for 10 MPa vs. 15.1 and 51.6 MHz for 60 MPa). A quadratic relationship was also found between the shell's shear modulus and the monopole and second dominant resonance frequencies as shown in Figure 4.15.

When the diameter of a 100 nm shell UCA is decreased from 6 μm to 1 μm , with the other simulation parameters held constant, several features changed in the backscatter response. The monopole peak became wider, decreased in height, and shifted towards higher frequencies. High resonant peaks originally presented in the backscatter of UCAs whose diameters are larger than 3 μm , are no longer present in the backscatter of UCAs of smaller diameters. The monopole resonance peak is not visible for the 1 μm UCA and may have occurred at a frequency outside the range of this study. The UCA monopole resonance frequency varies as a function of the inverse of the square root of the UCA diameter cubed (volume) as shown in Figure 4.16.

Few studies have looked at the contrast agents' dynamics at high frequencies and the majority of these studies have focused on the monopole resonance. The developed finite element model has the advantage of being able to predict higher resonances in addition to the monopole resonance. The results reported in this work show that the shell thickness, its elasticity, and the diameter of the UCA, play a significant role in the generation of other resonance peaks at high frequencies which may contribute to the generation of harmonics. This may provide an explanation to the presence of harmonics in the backscatter of the

Definity UCA at low pressure (Goertz *et al.*, 2005), where non-linear behaviour of the contrast agent is unlikely to occur. This study also shows that more careful design approaches may be taken to maximize the backscatter response from UCAs at high frequencies. This can be achieved by using the developed finite element model, which describes the basic fundamentals of sound wave propagation and stress-strain relationship within elastic material, to optimize the UCA parameters in order to obtain the desired results. In conclusion, the finite-element model was shown to be able to predict high frequency ultrasound scattering from ultrasound contrast agents. This will eventually help in the use of contrast agents for monitoring cancer treatment.

Chapter 5

Concluding remarks and future work

5.1 Summary and Concluding Remarks

Cancer cells may respond to drugs by undergoing apoptosis. It usually takes weeks or even months of repeated dosing with drugs until the efficiency of the cancer treatment is assessed. This long evaluation time period can be troublesome since drugs have severe side effects and are expensive. Hence, providing a rapid non-invasive way to assess the tumour response to treatment would be very beneficial. High frequency ultrasound has been shown to detect structural and physical changes in cell ensembles during apoptosis and hence has the potential of monitoring cancer treatment. Ultrasound contrast agents have also been shown to enhance contrast between the blood vessels and the surrounding tissue and hence may be used to distinguish between treated and untreated tissues. Theoretical models of high frequency ultrasound scattering from individual cells and ultrasound contrast agents are needed in order to develop methods for using ultrasound backscatter measurements to classify tumours, determine their responses to treatment, and eventually provide a better cancer treatment monitoring technique.

The backscatter from some non-nucleated biological specimens was investigated in Chapter 2 through the measurement and comparison of the backscatter response from sea urchin oocytes to theoretical predictions for scattering by a fluid sphere. It was found that

such a response is best modeled as a fluid sphere. Chapter 2 also established an objective methodology to determine the appropriate theoretical model of the properties of individual cells as ultrasound scatterers. In Chapter 3, a novel technique for measuring the ultrasound backscatter from individual micron-sized objects was developed by combining a microinjection system with a co-registered optical microscope and an ultrasound imaging device. This allowed the measurement of the ultrasound backscatter response from a single object under optical microscope guidance. The backscatter frequency responses from polystyrene microspheres were measured and compared to theoretical predictions. A very good agreement was found between the measured backscatter responses of individual microspheres and theoretical predictions of an elastic sphere recording theoretically predicted gradients of 43dB/13MHz. It was also shown that the backscatter responses from single OCI-AML-5 cells, were best modelled using the fluid sphere model.

In Chapter 4, a finite element model, built upon the fundamentals of acoustics and structural mechanics, was introduced to study the dynamic behaviour and the backscatter responses of elastic microspheres and ultrasound contrast agents. An excellent agreement was found between the analytical and finite elements solutions for the backscatter from individual polystyrene microspheres and ultrasound contrast agents. For the polystyrene microspheres, a systematic relationship was found between the resonance frequencies and the microsphere surface modes which appear in the form of non-spherical deformations. To the best of my knowledge, I am the first investigator to show a relationship between surface modes and resonance frequencies of microspheres. A correlation was also found between the resonance frequency and the angular distribution of scattering which becomes more complex in shape as the frequency increases. On the other hand, for the ultrasound contrast agent, no

systematic relationship between the resonance frequencies and the surface modes was found. Instead, the UCA exhibited a collection of complex oscillations which appear to be a combination of various surface modes. This was also confirmed by examining the angular distribution of scattering at its resonance frequencies. A study of the effects of varying the shell properties on the resonance frequencies of UCAs provided some insights into their backscatter behaviours. Increasing the shell thickness of the ultrasound contrast agent changed the resonance frequencies and the width of the resonant peaks. A quadratic relationship was found between the shell thickness and the monopole resonance frequency. A similar relationship was found between the shell's shear modulus and the first and the second dominant resonance frequencies. For both resonance frequencies, increasing shell thickness broadened the width of the resonant peaks. The UCA monopole frequency was also found to vary as a function of inverse of the square root of the UCA diameter cubed. These findings are crucial for the understanding of the UCA behaviour at high frequencies and the generation of harmonics. The finite element model developed in this work was shown to provide a better framework for understanding the scattering and the dynamic behaviour of spherical objects such as microspheres and ultrasound contrast agents.

5.2 Future work

In Chapter 3, I introduced a novel technique for measuring the backscatter response from individual objects which was applied to deduce the backscatter from untreated AML cells. This technique will be used to study the variation in the backscatter response from apoptotic (treated) individual AML cells at various stages of apoptosis. Such study is essential to better

understand the change in the backscatter of AML cells exposed to cisplatin (Figure 1.2). Various stains, such as Annexin V-FITC (BioVision, Inc., Mountain View, CA) which includes Annexin and Propidium Iodide, may be used to differentiate between early and late stage apoptosis. Annexin V binds to Phosphatidylserine, a phospholipid component found on the inner leaflet of the cell membrane that is exposed during early stage of apoptosis [Figure 5.1(a)]. Propidium Iodide binds to DNA only in later stage of apoptosis when the cell membrane has become permeable as shown in Figure 5.1(b).

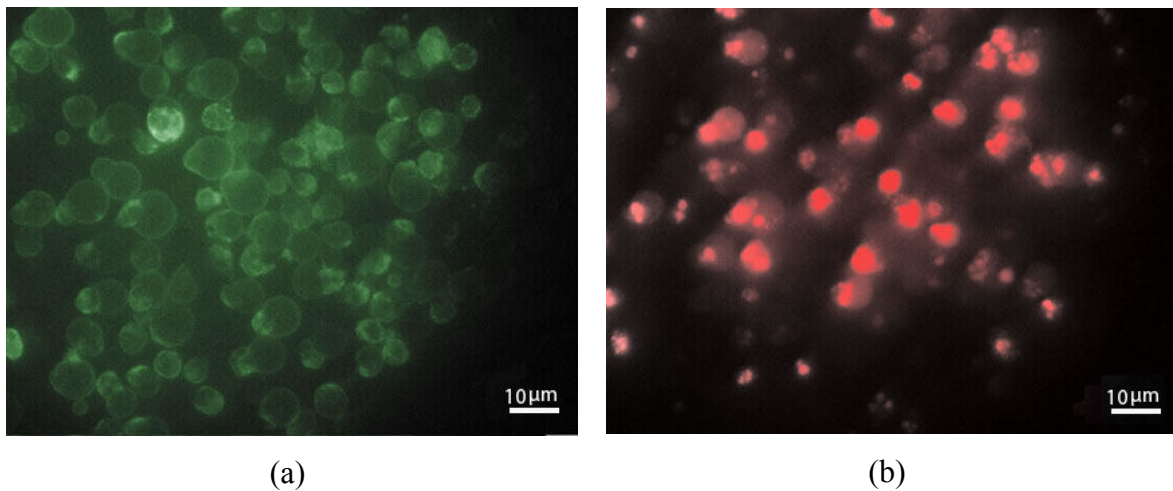


Figure 5.1: Fluorescence microscopy images of AML cells undergoing apoptosis: (a) Annexin V which stains the cell member during early stage apoptosis, (b) Propidium Iodide which stains the DNA in late stage apoptosis (courtesy of Avery Raess, Ryerson University, Toronto, ON)

Once the theoretical ultrasound backscatter responses from individual apoptotic cells in suspension are known, computer simulations may be used to calculate the ultrasound backscatter from tissues by using ultrasound scattering from collections of cells, in which each individual particles are assumed to have the same physical properties of that of the cell. This will be compared against experimental measurements of the backscatter from cells *in vitro* and *in vivo*. Such comparison will allow for the understanding of high frequency

ultrasound scattering from cells in viable and apoptotic tumour tissues (Figure 1.2). It should be noted, however, that cells in tissues may scatter in a different manner compared to when they are in suspension. In this case, I hypothesize that the cell nucleus may be the main contributor to the overall scattering and may be better modelled with either more complex formulations, or models in which the elasticity of the nucleus is taken into account. Work is currently underway in the Ultrasound Biomicroscopy Laboratory at Ryerson University to measure the high frequency ultrasound backscatter from early and late stages apoptotic cells and to use these measurements as input for computer simulations to calculate the ultrasound backscatter from tumour tissues.

In Chapter 4, I introduced a finite element model which is capable of predicting the dynamic behaviour of ultrasound contrast agents and their non-radial oscillations in particular. Computer simulations showed that thick shelled UCAs exhibit other resonance peaks which may be exploited for imaging purposes. The technique introduced in Chapter 3 can be used to measure the backscatter response from these individual UCAs at high frequencies which could be compared to theoretical predictions of the finite element model. If needed, parametric studies may be conducted to estimate some of the UCAs' physical properties (such as the shell's elasticity) which are hard to measure experimentally. This work is particularly important for the optimization of ultrasound contrast agents for high frequency ultrasound.

The finite element model may also be used to gain a better understanding of the mechanism of drug release from drug delivery vehicles (such as drug encapsulated polymer microspheres) for therapeutic applications. The number of fragments formed during the UCA fragmentation has been linked to surface modes (Versluis *et al.*, 2004) and hence a study of

these modes will help in determining the optimal conditions for the drug release. The finite element model could also be used to understand the scattering behaviour of targeted ultrasound contrast agents when they are bound to cells or inhibited from oscillating freely due to other obstacles. Such understanding is crucial for various targeted ultrasound imaging applications, such as molecular imaging.

The work presented in this dissertation has laid the foundation for new directions in high frequency ultrasound imaging applications, which will eventually help in the early detection and treatment monitoring of cancer.

Appendix A

Analytical Solution of Sound Scattering from a Sphere Immersed in a Fluid

The Anderson and Faran formulations of sound scattering from a homogeneous sphere immersed in a fluid are given below. 40 terms were used in the summation in order to guarantee convergence. All the following equations were coded in MATLAB® R2009a.

Anderson's Solution for Fluid Sphere Immersed in a Fluid

The mathematical solution of acoustic scattering from a fluid sphere submerged in a fluid was derived by Anderson (1950). The equations model plane acoustic wave travelling in the $-z$ direction and impinging upon a sphere centered at the origin as illustrated in figure A.1. c_1 and c_3 are the longitudinal sound velocities in scatterer and the surrounding medium, respectively. The complex pressure field at the observation point P is given by⁴:

$$p_s = -P_0 \sum_{m=0}^{\infty} \left[\frac{(-i)^m (2m+1)}{(1+iC_m)} \right] \times P_m(\cos(\theta)) \left[j_m(k_3 r) + in_m(k_3 r) \right], \quad (\text{A.1})$$

where m is the order of the scattered wave, P_m is the m^{th} order Legendre function, j_m is the spherical Bessel function, and n_m is the spherical Neumann function and $k_3 = 2\pi f / c_3$.

⁴ i refers to square root of -1

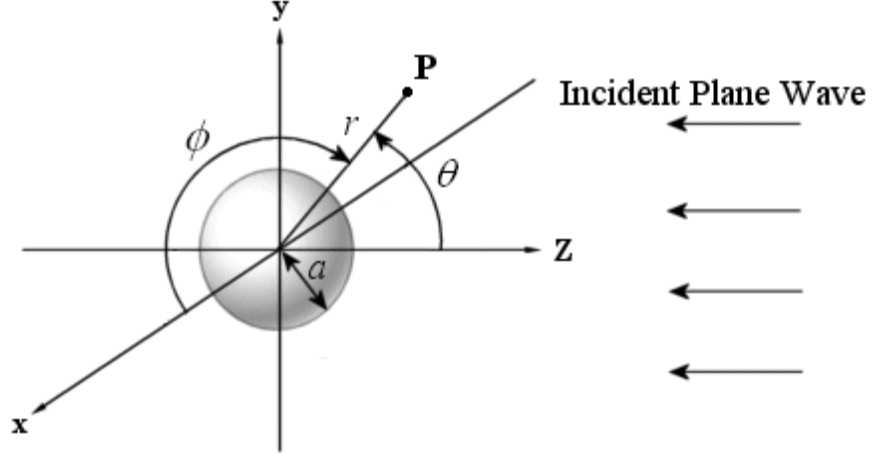


Figure A.1: Illustration of scattering by a sphere (Forward scattering occurs at the angle $\theta = 180^\circ$, and backscatter occurs when $\theta = 0^\circ$).

C_m is defined as:

$$C_m = \frac{[\alpha_m(k_1 a) / \alpha_m(k_3 a)] [n_m(k_3 a) / j_m(k_1 a)] - [\beta_m(k_3 a) / \alpha_m(k_3 a)] gh}{[\alpha_m(k_1 a) / \alpha_m(k_3 a)] [j_m(k_3 a) / j_m(k_1 a)] - gh}, \quad (\text{A.2})$$

$$\alpha_m(x) = mj_{m-1}(x) - (m+1)j_{m+1}(x), \quad (\text{A.3})$$

$$\beta_m(x) = mn_{m-1}(x) - (m+1)n_{m+1}(x), \quad (\text{A.4})$$

$$g = \rho_1 / \rho_3, \quad (\text{A.5})$$

$$h = c_1 / c_3, \quad (\text{A.6})$$

and

$$k_1 = 2\pi f / c_1. \quad (\text{A.7})$$

Faran's Solution for an Elastic Sphere Immersed in a Fluid

J. Faran (1951) was the first to derive the analytical solution of acoustic scattering from a sphere made of elastic material which supports both longitudinal (compressional) and transverse (shear) waves. Assuming that the incident plane wave is travelling in the $+z$ direction, the expression of the scattered pressure at a point P is given by:

$$p_s(r, \theta) = \sum_{m=0}^{\infty} c_m [j_m(k_3 r) - i n_m(k_3 r)] P_m(\cos \theta), \quad (\text{A.8})$$

where c_n is defined as:

$$c_m = -P_0 (2m+1) (-i)^{m+1} \sin \eta_m \exp(i\eta_m) \quad (\text{A.9})$$

and η_m is the phase-shift of the m^{th} scattered wave, defined as:

$$\tan \eta_m = \tan \delta_m(x_3) \frac{\tan \Phi_m + \tan \alpha_m(x_3)}{\tan \Phi_m + \tan \beta_m(x_3)}. \quad (\text{A.10})$$

The intermediate scattering angles, $\alpha_m(x)$, $\beta_m(x)$, and the boundary impedance phase-angle

Φ_m are given by:

$$\delta_m(x) = \tan^{-1} [-j_m(x) / n_m(x)], \quad (\text{A.11})$$

$$\alpha_m(x) = \tan^{-1} [-x j_m'(x) / j_m(x)], \quad (\text{A.12})$$

$$\beta_m(x) = \tan^{-1} [-x n_m'(x) / n_m(x)], \quad (\text{A.13})$$

and

$$\tan \Phi_m = -(\rho_3 / \rho_1) \tan \zeta_m(x_1, \sigma). \quad (\text{A.14})$$

The scattering phase angle $\zeta_m(x_1, \nu)$ is defined as:

$$\zeta_m(x_1, \nu) = \tan^{-1} \left[\frac{\frac{\tan \alpha_m(x_1)}{\tan \alpha_m(x_1) + 1} - \frac{m^2 + m}{m^2 + m - 1 - \frac{1}{2}x_2^2 + \tan \alpha_m(x_2)}}{\frac{\frac{x_2^2}{2} \frac{m^2 + m - 1 - \frac{1}{2}x_2^2 + 2 \tan \alpha_m(x_1)}{m^2 + m - 1 - \frac{1}{2}x_2^2 + \tan \alpha_m(x_2)} - \frac{(m^2 + m)[\tan \alpha_m(x_2) + 1]}{m^2 + m - 1 - \frac{1}{2}x_2^2 + \tan \alpha_m(x_2)}}{\tan \alpha_m(x_1) + 1}} \right], \quad (\text{A.15})$$

where ν is the Poisson's ratio and x_1, x_2, x_3 are given by:

$$x_1 = k_1 a, \quad k_1 = 2\pi f / c_1,$$

$$x_2 = k_2 a, \quad k_2 = 2\pi f / c_2,$$

and $x_3 = k_3 a, \quad k_3 = 2\pi f / c_3$. c_1 and c_2 are the longitudinal and shear sound velocities in scatterer, respectively, and c_3 is the longitudinal sound velocity in the surrounding medium. For a rigid scatterer, the velocities of both compressional and shear waves are infinite ($x_1 = 0$ and $x_2 = 0$). A scatterer of infinite density will be immovable. Therefore, the scattered field of a rigid immovable scatterer is found by setting $\tan \Phi_m = 0$ in equation A.14.

Church's solution of Sound Scattering from a Sphere Immersed in a Fluid

C. Church (1995) derived a Rayleigh-Plesset-like equation describing the dynamics of ultrasound contrast agents. In his formulation, the shell is assumed to be a continuous layer of solid viscoelastic material which separates the gas core from the bulk Newtonian surrounding liquid as shown in Figure A.2.

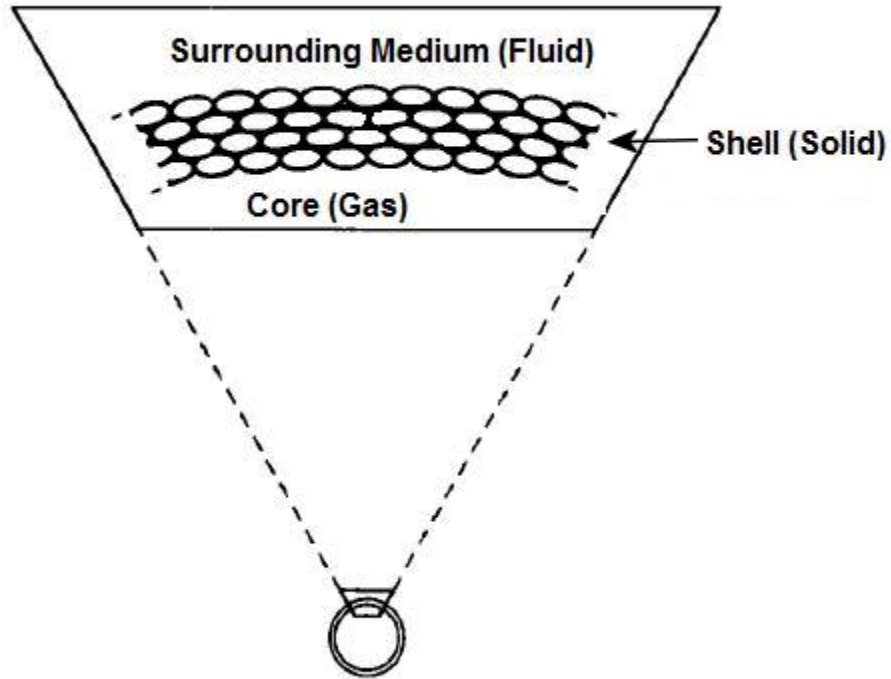


Figure A.2: Depiction of an ultrasound contrast agent. The shell is assumed to be elastic solid composed of layers of molecules (Adapted from Church, 1995)

An analytical solution to the equation was obtained for the fundamental response whose angular linear resonance frequency, ω_0 , is given by:

$$\omega_0 = \sqrt{\left(\rho_s R_{01}^2 \gamma\right)^{-1} \left\{ 3\kappa P_h - \frac{2s_1}{R_{01}} - \frac{2s_2 R_{01}^3}{R_{02}^4} + 4 \frac{V_s G_s}{R_{02}^3} \left[1 + S \left(1 + \frac{3R_{01}^3}{R_{02}^3} \right) \right] \right\}}, \quad (\text{A.16})$$

$$\gamma = \left[1 + \left(\frac{\rho_L - \rho_S}{\rho_S} \right) \frac{R_{01}}{R_{02}} \right], \quad (\text{A.17})$$

$$V_s = R_{02}^3 - R_{01}^3, \quad (\text{A.18})$$

$$S = \left\{ \left[\frac{2s_1}{R_{01}} + \frac{2s_2}{R_{02}} \right] \left[\frac{R_{02}^3}{V_s} \right] (4G_s)^{-1} \right\}, \quad (\text{A.19})$$

where $G_s, \rho_s, R_{01}, R_{02}, s_1, s_2$ are terms accounting for the shear modulus, mass density, inner radius, outer radius, inner surface tension, outer surface tension of the shell, respectively. ρ_L is the mass density of the surrounding medium, P_h is the hydrostatic pressure (10^5 Pa), and κ is the polytropic exponent (1.4 in the adiabatic case).

Appendix B

List of Publications

Papers in Refereed Journals

1. **O. Falou**, M. Rui, A. El Kaffas, J. C. Kumaradas, and M. C. Kolios, “The Measurement of Ultrasound Scattering from Individual Micron-sized Objects and its Application in Single Cell Scattering,” *Journal of the Acoustical Society of America* 128, (2): 894-902, 2010 (also selected for publication in the *Virtual Journal of Biological Physics Research*, 20(4), 2010)
2. **O. Falou**, R. E. Baddour, G. Nathanael, G. J. Czarnota, J. C. Kumaradas, and M. C. Kolios, “A Study of High Frequency Ultrasound Scattering from Non-nucleated Biological Specimens,” *Journal of the Acoustical Society of America* 124(5):EL278-83, 2008 (also selected for publication in the *Virtual Journal of Biological Physics Research*, 16(8), 2008)

Papers in Refereed Conference Proceedings

1. **O. Falou**, A. Jafari Sojahrood, J. C. Kumaradas, M. C. Kolios, “Modelling the Effect of Shell Thickness on High Frequency Ultrasound Scattering from Ultrasound Contrast Agents,” *Canadian Acoustical Association Conference*, Victoria, Canada, 2010
2. **O. Falou**, M. Rui, A. El Kaffas, J. C. Kumaradas, and M. C. Kolios, “A Novel Technique for Measuring Ultrasound Backscatter from Single Micron-Sized Objects,” *IEEE International Ultrasonics Symposium*, Rome, Italy, 2009 (won Travel Award; declined)
3. **O. Falou**, M. Rui, A. El Kaffas, J. C. Kumaradas, and M. C. Kolios, “Modelling High Frequency Acoustic Backscatter from Biological Cells,” *Canadian Acoustical Association Conference*, Niagra-on-the-Lake, Canada, 2009
4. **O. Falou**, J. C. Kumaradas, and M. C. Kolios, “Modelling High Frequency Acoustic Backscatter Response from Non-Nucleated Biological Specimens,” *Canadian Acoustics* 36(3): pp. 38-39, 2008 (won Best Student Presentation Award)
5. **O. Falou**, J. C. Kumaradas, and M. C. Kolios, “Finite-element Modelling of Elastic Surface Modes and Scattering from Elastic Objects,” *COMSOL Users Conference*, Boston, USA, 2007
6. **O. Falou**, J. C. Kumaradas, and M. C. Kolios, “Finite Element Modelling of Ultrasound Scattering by Spherical Objects and Cells,” *IEEE International Ultrasonics Symposium*, Vancouver, Canada, 2006
7. **O. Falou**, J. C. Kumaradas, and M. C. Kolios, “Modelling Acoustic Wave Scattering from Cells and Microbubbles,” *COMSOL Users Conference*, Boston, USA, 2006

Abstracts and/or other Conference Proceedings

1. **O. Falou**, M. Rui, A. El-Kaffas, J. C. Kumaradas, and M. C. Kolios, "A Novel Technique for Measuring High Frequency Ultrasound Backscatter from Individual Micron-sized Objects and its Use for Determining the Mechanical Nature of Single Cells," *Imaging Network Ontario Imaging Symposium*, Toronto, Canada, 2010
2. **O. Falou**, J. C. Kumaradas, and M. C. Kolios, "Towards the Modelling of High-Frequency Ultrasound Scattering from Ultrasound Contrast Agents," *Imaging Network Ontario Imaging Symposium*, Toronto, Canada, 2008 (Poster Award, 2nd prize)
3. **O. Falou**, J. C. Kumaradas, and M. C. Kolios, "Towards the Modelling of High-Frequency Ultrasound Scattering from Cells," *Journal of the Acoustical Society of America* 123(5): pg. 3000, 2008
4. **O. Falou**, J. C. Kumaradas, and M. C. Kolios, "Finite-element Modelling of Microsphere Surface Modes and High-Frequency Ultrasound Scattering from a Single Cell," *Journal of the Acoustical Society of America* 122(5): pg 2957, 2007

Bibliography

- Allen, J. S., Kruse, D. E., and Ferrara, K. W. (2001). "Shell waves and acoustic scattering from ultrasound contrast agents," *IEEE Transactions on Ultrasonics Ferroelectrics and Frequency Control* **48**, 409-418.
- Anderson, V. C. (1950). "Sound scattering from a fluid sphere," *J. Acoust. Soc. Am.* **22**, 426-431.
- Azuma, H., Tomita, N., Kaneda, Y., Koike, H., Ogihara, T., Katsuoka, Y., and Morishita, R. (2003). "Transfection of nf kappa b-decoy oligodeoxynucleotides using efficient ultrasound-mediated gene transfer into donor kidneys prolonged survival of rat renal allografts," *Gene Ther.* **10**, 415-425.
- Baddour, R. E., and Kolios, M. C. (2007). "The fluid and elastic nature of nucleated cells: Implications from the cellular backscatter response," *J. Acoust. Soc. Am.* **121**, EL16-EL22.
- Baddour, R. E., Sherar, M. D., Hunt, J. W., Czarnota, G. J., and Kolios, M. C. (2005). "High-frequency ultrasound scattering from microspheres and single cells," *J. Acoust. Soc. Am.* **117**, 934-943.
- Bayliss, A., Gunzburger, M., and Turkel, E. (1982). "Boundary-conditions for the numerical-solution of elliptic-equations in exterior regions," *SIAM Journal on Applied Mathematics* **42**, 430-451.
- Becher, O. J., and Holland, E. C. (2006). "Genetically engineered models have advantages over xenografts for preclinical studies," *Cancer Res.* **66**, 3351-3354.
- Chen, J. S., Hunter, K. S., and Shandas, R. (2009). "Wave scattering from encapsulated microbubbles subject to high-frequency ultrasound: Contribution of higher-order scattering modes," *J. Acoust. Soc. Am.* **126**, 1766-1775.
- Chen, W. S., Matula, T. J., Brayman, A. A., and Crum, L. A. (2003). "A comparison of the fragmentation thresholds and inertial cavitation doses of different ultrasound contrast agents," *J. Acoust. Soc. Am.* **113**, 643-651.
- Church, C. C. (1995). "The effects of an elastic solid-surface layer on the radial pulsations of gas-bubbles," *J. Acoust. Soc. Am.* **97**, 1510-1521.

- Cobbold, R. S. C. (2007). "Foundations of biomedical ultrasound," (Toronto).
- COMSOL (2008). *Acoustics module: User's guide* (COMSOL, Inc., Burlington, MA).
- Czarnota, G. J., Kolios, M. C., Abraham, J., Portnoy, M., Ottensmeyer, F. P., Hunt, J. W., and Sherar, M. D. (1999). "Ultrasound imaging of apoptosis: High-resolution non-invasive monitoring of programmed cell death in vitro, in situ and in vivo," *Br. J. Cancer* **81**, 520-527.
- Czarnota, G. J., Kolios, M. C., Vaziri, H., Benchimol, S., Ottensmeyer, F. P., Sherar, M. D., and Hunt, J. W. (1997). "Ultrasonic biomicroscopy of viable, dead and apoptotic cells," *Ultrasound Med. Biol.* **23**, 961-965.
- Davis, T. A. (2004). "Algorithm 832: Umfpack v4.3 - an unsymmetric-pattern multifrontal method," *Acm Transactions on Mathematical Software* **30**, 196-199.
- De Jong, N., and Hoff, L. (1993). "Ultrasound scattering properties of albnex microspheres," *Ultrasonics* **31**, 175-181.
- Demkowicz, L., and Shen, J. (2006). "A few new (?) facts about infinite elements," *Computer Methods In Applied Mechanics And Engineering* **195**, 3572-3590.
- Deng, C. X., Lizzi, F. L., Silverman, R. H., Ursea, R., and Coleman, D. J. (1998). "Imaging and spectrum analysis of contrast agents in the in vivo rabbit eye using very-high-frequency ultrasound," *Ultrasound Med. Biol.* **24**, 383-394.
- Doinikov, A. A., and Dayton, P. A. (2007). "Maxwell rheological model for lipid-shelled ultrasound microbubble contrast agents," *J. Acoust. Soc. Am.* **121**, 3331-3340.
- Dollet, B., van der Meer, S. M., Garbin, V., de Jong, N., Lohse, D., and Versluis, M. (2008). "Nonspherical oscillations of ultrasound contrast agent microbubbles," *Ultrasound Med. Biol.* **34**, 1465-1473.
- Doyle, T. E., Tew, A. T., Warnick, K. H., and Carruth, B. L. (2009). "Simulation of elastic wave scattering in cells and tissues at the microscopic level," *J. Acoust. Soc. Am.* **125**, 1751-1767.
- Eaton, J. A., and Regan, B. A. (1996). "Application of the finite element method to acoustic scattering problems," *Aiaa Journal* **34**, 29-34.
- Emmer, M., van Wamel, A., Goertz, D. E., and de Jong, N. (2007). "The onset of microbubble vibration," *Ultrasound Med. Biol.* **33**, 941-949.

- Everstine, G. C., and Henderson, F. M. (1990). "Coupled finite-element boundary element approach for fluid structure interaction," *J. Acoust. Soc. Am.* **87**, 1938-1947.
- Falou, O., Baddour, R. E., Nathanael, G., Czarnota, G. J., Kumaradas, J. C., and Kolios, M. C. (2008). "A study of high frequency ultrasound scattering from non-nucleated biological specimens," *J. Acoust. Soc. Am.* **124**, EL278-283.
- Falou, O., Kumaradas, J. C., and Kolios, M. C. (2006). "Finite element modeling of ultrasound scattering by spherical objects and cells," in *2006 IEEE Ultrasonics Symposium, Vols 1-5, Proceedings* (Vancouver, Canada), pp. 2072-2075.
- Falou, O., Rui, M., El Kaffas, A., Kumaradas, J. C., and Kolios, M. C. (2010). "The measurement of ultrasound scattering from individual micron-sized objects and its application in single cell scattering," *J. Acoust. Soc. Am.* **128**, 894-902.
- Faran, J. J. (1951). "Sound scattering by solid cylinders and spheres," *J. Acoust. Soc. Am.* **23**, 405-418.
- Feleppa, E. J., Liu, T., Lizzi, F. L., Kalisz, A., Silverman, R. H., Sigel, B., and Fair, W. R. (2000). "Three-dimensional ultrasonic parametric and tissue-property imaging for tissue evaluation, treatment planning, therapy guidance, and efficacy assessment," in *Proceedings of SPIE - The International Society for Optical Engineering* (San Diego, CA, USA), pp. 68-76.
- Fellinger, K., and Schmidt, J. (1954). "Klinik and therapie des chronischen," in *Gelenkrehmatismus* (Maudrich, Vienna, Austria), pp. 549-552.
- Firestone, F. A. (1945). "The supersonic reflectoscope for interior inspection," *Metal Progress* **48**, 505-512.
- Flax, L., Dragonette, L. R., and Uberall, H. (1978). "Theory of elastic resonance excitation by sound scattering," *J. Acoust. Soc. Am.* **63**, 723-731.
- Garbin, V., Cojoc, D., Ferrari, E., Di Fabrizio, E., Overvelde, M. L. J., Van Der Meer, S. M., De Jong, N., Lohse, D., and Versluis, M. (2007). "Changes in microbubble dynamics near a boundary revealed by combined optical micromanipulation and high-speed imaging," *Applied Physics Letters* **90**.
- Gerald, C. F., and Wheatley, P. O. (1999). *Applied numerical analysis* (Addison Wesley, Reading).
- Goertz, D. E., Cherin, E., Needles, A., Karshafian, R., Brown, A. S., Burns, P. N., and Foster, F. S. (2005). "High frequency nonlinear b-scan imaging of microbubble contrast agents," *IEEE Transactions on Ultrasonics Ferroelectrics and Frequency Control* **52**, 65-79.

- Goertz, D. E., Frijlink, M., Bouakaz, A., Chin, C. T., De Jong, N., and Van Der Steen, A. W. F. (2003). "The effect of bubble size on nonlinear scattering from microbubbles at high frequencies," in *Proceedings of the IEEE Ultrasonics Symposium*, pp. 1503-1506.
- Goertz, D. E., Frijlink, M. E., Tempel, D., Bhagwandas, V., Gisolf, A., Krams, R., de Jong, N., and van der Steen, A. F. W. (2007). "Subharmonic contrast intravascular ultrasound for vasa vasorum imaging," *Ultrasound Med. Biol.* **33**, 1859-1872.
- Group, R. C. D. R. (2007). "Apoptosis," (Reproductive & Cardiovascular Disease Research Group, St George's University of London, London).
- Hacker, G. (2000). "The morphology of apoptosis," *Cell Tissue Res.* **301**, 5-17.
- Hampton, L. D., and McKinney, C. M. (1961). "Experimental study of scattering of acoustic energy from solid metal spheres in water," *J. Acoust. Soc. Am.* **33**, 664-&.
- Harrison, G. H., Balcerkubiczek, E. K., and Eddy, H. A. (1991). "Potentiation of chemotherapy by low-level ultrasound," *Int. J. Radiat. Biol.* **59**, 1453-1466.
- Hickling, R. (1962). "Analysis of echoes from a solid elastic sphere in water," *J. Acoust. Soc. Am.* **34**, 1582-1592.
- Hoff, L. (2001). *Acoustic characterization of contrast agents for medical ultrasound imaging* (Kluwer Academic Publishers, Dordrecht).
- Hunt, J. T., Knittel, M. R., Nichols, C. S., and Barach, D. (1975). "Finite-element approach to acoustic scattering from elastic structures," *J. Acoust. Soc. Am.* **57**, 287-299.
- Hunt, J. W., Worthington, A. E., Xuan, A., Kolios, M. C., Czarnota, G. J., and Sherar, M. D. (2002). "A model based upon pseudo regular spacing of cells combined with the randomisation of the nuclei can explain the significant changes in high-frequency ultrasound signals during apoptosis," *Ultrasound Med. Biol.* **28**, 217-226.
- Insana, M. F., and Hall, T. J. (1990). "Characterizing the microstructure of random-media using ultrasound," *Phys. Med. Biol.* **35**, 1373-1386.
- Kenner, T. (1989). "The measurement of blood density and its meaning " *Basic Res. Cardiol.* **84**, 111-124.
- Kerr, J. F. R., Wyllie, A. H., and Currie, A. R. (1972). "Apoptosis - basic biological phenomenon with wide-ranging implications in tissue kinetics," *Br. J. Cancer* **26**, 239-257.

- Ketterling, J. A., Mamou, J., Allen, J. S., Aristizabal, O., Williamson, R. G., and Turnbull, D. H. (2007). "Excitation of polymer-shelled contrast agents with high-frequency ultrasound," *J. Acoust. Soc. Am.* **121**, EL48-EL53.
- Klibanov, A. L. (2006). "Microbubble contrast agents - targeted ultrasound imaging and ultrasound-assisted drug-delivery applications," *Invest. Radiol.* **41**, 354-362.
- Knight, M. M., Bravenboer, J., Lee, D. A., van Osch, G., Weinans, H., and Bader, D. L. (2002). "Cell and nucleus deformation in compressed chondrocyte-alginate constructs: Temporal changes and calculation of cell modulus," *Biochimica Et Biophysica Acta-General Subjects* **1570**, 1-8.
- Kolios, M. C., Czarnota, G. J., Lee, M., Hunt, J. W., and Sherar, M. D. (2002). "Ultrasonic spectral parameter characterization of apoptosis," *Ultrasound Med. Biol.* **28**, 589-597.
- Kolios, M. C., Czarnota, G. J., Worthington, A., Giles, A., Tunis, A. S., and Sherar, M. D. (2004). "Towards understanding the nature of high frequency backscatter from cells and tissues: An investigation of backscatter power spectra from different concentrations of cells of different sizes," in *2004 IEEE International Ultrasonics, Ferroelectrics, and Frequency Control Joint 50th Anniversary Conference* (Montreal, Quebec, Canada), pp. 606-609.
- Krishnan, S., Rigby, K. W., and O'Donnell, M. (1997). "Improved estimation of phase aberration profiles," *Transactions on Ultrasonics, Ferroelectrics and Frequency Control* **44**, 701-713.
- Leighton, T. G. (2004). *The acoustic bubble* (Academic Press, London).
- Lizzi, F. L., Astor, M., Feleppa, E. J., Shao, M., and Kalisz, A. (1997). "Statistical framework for ultrasonic spectral parameter imaging," *Ultrasound Med. Biol.* **23**, 1371-1382.
- Lizzi, F. L., Greenebaum, M., Feleppa, E. J., Elbaum, M., and Coleman, D. J. (1983). "Theoretical framework for spectrum analysis in ultrasonic tissue characterization," *J. Acoust. Soc. Am.* **73**, 1366-1373.
- Lizzi, F. L., King, D. L., Rorke, M. C., Hui, J., Ostromogilsky, M., Yaremko, M. M., Feleppa, E. J., and Wai, P. (1988). "Comparison of theoretical scattering results and ultrasonic data from clinical liver examinations," *Ultrasound Med. Biol.* **14**, 377-385.
- Logan, D. L. (2002). *A first course in finite element method* (Thomson Learning Inc., Pacific Grove).
- MacKenzie, K. V. (1981). "Nine-term equation for sound speed in the oceans " *The Journal of the Acoustical Society of America* **70**, 807-812.

- Macovski, A. (1983). *Medical imaging systems* (Prentice-Hall, Inc., Upper Saddle River, NJ).
- Mamou, J., Oelze, M. L., O'Brien, W. D., and Zachary, J. F. (2006). "Perspective on biomedical quantitative ultrasound imaging," *IEEE Signal Processing Magazine* **23**, 112-116.
- Mie, G. (1908). "Beiträge zur optik trüber medien, speziell kolloidaler metallösungen," *Annalen der Physik* **25**, 377-445.
- Moran, C. M., Watson, R. J., Fox, K. A. A., and McDicken, W. N. (2002). "In vitro acoustic characterisation of four intravenous ultrasonic contrast agents at 30 mhz," *Ultrasound Med. Biol.* **28**, 785-791.
- Mordfin, L. (2002). *Handbook of reference data for nondestructive testing* (American Society for Testing & Materials, Inc., West Conshohocken, PA).
- Morse, P. M. (1936). *Vibration and sound* (American Institute of Physics, New York).
- Naf, D., Krupke, D. M., Sundberg, J. P., Eppig, J. T., and Bult, C. J. (2002). "The mouse tumor biology database: A public resource for cancer genetics and pathology of the mouse," *Cancer Res.* **62**, 1235-1240.
- Nassiri, D. K., and Hill, C. R. (1986). "The use of angular acoustic scattering measurements to estimate structural parameters of human and animal tissue," *J. Acoust. Soc. Am.* **79**, 2048-2054.
- NCRP (1983). "Biological effects of ultrasound: Mechanisms and clinical implications," (Washington, DC).
- Numrich, S. K., Varadan, V. V., and Varadan, V. K. (1981). "Scattering of acoustic-waves by a finite elastic cylinder immersed in water," *J. Acoust. Soc. Am.* **70**, 1407-1411.
- Oelze, M. L., O'Brien Jr, W. D., Blue, J. P., and Zachary, J. F. (2004). "Differentiation and characterization of rat mammary fibroadenomas and 4t1 mouse carcinomas using quantitative ultrasound imaging," *IEEE Trans. Med. Imaging* **23**, 764-771.
- Oelze, M. L., Zachary, J. F., and O'Brien Jr., W. D. (2002). "Characterization of tissue microstructure using ultrasonic backscatter: Theory and technique for optimization using a gaussian form factor," *J. Acoust. Soc. Am.* **112**, 1202-1211.
- Overgaard, J., Gonzalez, D. G., Hulshof, M., Arcangeli, G., Dahl, O., Mella, O., and Bentzen, S. M. (1995). "Randomized trial of hyperthermia as adjuvant to radiotherapy for recurrent or metastatic malignant-melanoma," *Lancet* **345**, 540-543.

- Patil, A. V., Reynolds, P., and Hossack, J. A. (2010). "A non-linear three-dimensional model for quantifying microbubble dynamics," *J. Acoust. Soc. Am.* **127**, EL80-EL86.
- Paubin, M. C., Mensah, S., and Lefebvre, J. P. (2007). "Development of a finite element model of ultrasound contrast agent," in *Proceedings - IEEE Ultrasonics Symposium*, pp. 1989-1992.
- Reid, J. M., and Wild, J. J. (1952). "Further pilot echographic studies on the histological structure of tumors of the living intact human breast", *Am. J. Pathol.* **28**, 839-861.
- Saad, A. H., and Hahn, G. M. (1989). "Ultrasound enhanced drug toxicity on chinese-hamster ovary cells-invitro," *Cancer Res.* **49**, 5931-5934.
- Saad, A. H., and Hahn, G. M. (1992). "Ultrasound-enhanced effects of adriamycin against murine tumors," *Ultrasound Med. Biol.* **18**, 715-723.
- Salgame, P., Varadhachary, A. S., Primiano, L. L., Fincke, J. E., Muller, S., and Monestier, M. (1997). "An elisa for detection of apoptosis," *Nucleic Acids Research* **25**, 680-681.
- Saraste, A., and Pulkki, K. (2000). "Morphologic and biochemical hallmarks of apoptosis," *Cardiovasc. Res.* **45**, 528-537.
- Serway, R. A., and Beichner, R. J. (2000). *Physics for scientists and engineers* (Saunders College Publishing, Orlando, FL).
- Sherar, M. D., Noss, M. B., and Foster, F. S. (1987). "Ultrasound backscatter microscopy images the internal structure of living tumor spheroids," *Nature* **330**, 493-495.
- Society, C. C. (2002). "Canadian cancer statistics 2002."
- StatsCan (2004). "Mortality, summary: List of causes," (Ottawa).
- Stride, E., and Saffari, N. (2003). "Microbubble ultrasound contrast agents: A review," *Proceedings Of The Institution Of Mechanical Engineers Part H-Journal Of Engineering In Medicine* **217**, 429-447.
- Strutt, J. W. (1872). "Investigation of the disturbance produced by a spherical obstacle on the waves of sound," in *London Mathematical Society*, pp. 233-283.
- Szabo, T. L. (2004). *Diagnostic ultrasound imaging* (Elsevier Academic Press, Burlington, MA).

- Taggart, L. R., Baddour, R. E., Giles, A., Czarnota, G. J., and Kolios, M. C. (2007). "Ultrasonic characterization of whole cells and isolated nuclei," *Ultrasound Med. Biol.* **33**, 389-401.
- Tunis, A. S., Czarnota, G. J., Giles, A., Sherar, M. D., Hunt, J. W., and Kolios, M. C. (2005). "Monitoring structural changes in cells with high-frequency ultrasound signal statistics," *Ultrasound Med. Biol.* **31**, 1041-1049.
- Tyle, P., and Agrawala, P. (1989). "Drug delivery by phonophoresis," *Pharm. Res.* **6**, 355-361.
- Uberall, H., Ripoche, J., Maze, G., and Izbicki, J.-L. (1996). "The resonances: From nuclear physics to underwater acoustics," in *Acoustic interactions with submerged elastic structures*, edited by A. Guran, J. Ripoche, and F. Ziegler (World Scientific Publishing Company, River Edge, NJ), pp. 1-14.
- Ursea, R., Coleman, D. J., Silverman, R. H., Lizzi, F. L., Daly, S. M., and Harrison, W. (1998). "Correlation of high frequency ultrasound backscatter with tumor microstructure in iris melanoma," *Ophthalmology* **105**, 906-912.
- Vernon, C. C., Hand, J. W., Field, S. B., Machin, D., Whaley, J. B., vanderZee, J., vanPutten, W. L. J., vanRhoon, G. C., vanDijk, J. D. P., Gonzalez, D. G., Liu, F. F., Goodman, P., and Sherar, M. (1996). "Radiotherapy with or without hyperthermia in the treatment of superficial localized breast cancer: Results from five randomized controlled trials," *International Journal of Radiation Oncology Biology Physics* **35**, 731-744.
- Versluis, M., Van Der Meer, S. M., Lohse, D., Palanchon, P., Goertz, D., Chin, C. T., and De Jong, N. (2004). "Microbubble surface modes," in *Proceedings - IEEE Ultrasonics Symposium*, pp. 207-209.
- Vlad, R. M., Alajez, N. M., Giles, A., Kolios, M. C., and Czarnota, G. J. (2008). "Quantitative ultrasound characterization of cancer radiotherapy effects in vitro," *International Journal of Radiation Oncology Biology Physics* **72**, 1236-1243.
- Vlad, R. M., Brand, S., Giles, A., Kolios, M. C., and Czarnota, G. J. (2009). "Quantitative ultrasound characterization of responses to radiotherapy in cancer mouse models," *Clin. Cancer Res.* **15**, 2067-2075.
- Vos, H. J., Versluis, M., and De Jong, N. (2007). "Orthogonal observations of vibrating microbubbles," in *Proceedings - IEEE Ultrasonics Symposium*, pp. 765-768.
- Wilton, D. T. (1978). "Acoustic radiation and scattering from elastic structures," *International Journal For Numerical Methods In Engineering* **13**, 123-138.

Zhao, S., Ferrara, K. W., and Dayton, P. A. (2005). "Asymmetric oscillation of adherent targeted ultrasound contrast agents," *Applied Physics Letters* **87**, 1-3.

Zhao, S., Kruse, D. E., Ferrara, K. W., and Dayton, P. A. (2006). "Acoustic response from adherent targeted contrast agents," *J. Acoust. Soc. Am.* **120**.

Zienkiewicz, O. C., Taylor, R. L., and Zhu, J. Z. (2005). *The finite element method: Its basis and fundamentals* (Elsevier Butterworth-Heinemann, Oxford).